POLITECNICO
MILANO 1863

SCUOLA DI INGEGNERIA INDUSTRIALE
E DELL'INFORMAZIONE

Injectable gelatin-based photocurable composite hydrogel for the treatment of osteochondral defects

Tesi di Laurea Magistrale in
Biomedical Engineering - Ingegneria Biomedica

Author: **Ignazio Niosi**

Student ID: 952678
Main advisor: Prof. Silvia Farè
External advisor: Prof. Leonardo Ricotti
Co-advisors: Lorenzo Vannozzi, Diego Trucco
Academic Year: 2021-22

Abstract

Osteochondral (OC) injuries affect millions of people of all ages worldwide every year with a significant socio-economic impact. Many approaches are used to date but there is still no definitive therapy and an overall gold standard. Among the approaches that attempt to regenerate the osteochondral tissue in the appropriate way, minimally invasive injectable systems based on hydrogels have come to light in research. Among these, natural hydrogels seem to be optimal candidates, but one of their main limitations is their lack of mechanical properties for load-bearing applications, as OC tissue. In the presented thesis it was demonstrated how to increase the compressive mechanical properties of a gelatin methacrylate (GelMA) network by using a filler based on dispersed fibers (DFs) made of a poly-(ϵ)-caprolactone (PCL) /GelMA blend so to obtain a GelMA+DFs composite. In order to produce DFs, electruspun random mesh (isotropic) and aligned mesh (anisotropic) were ultrasonicated. However, the procedure proved to be unreliable, probably due to the high plasticity of the PCL. Thus, a cryomicro-cutting approach was implemented in order to disperse fibers, resulting in microstructured DFs through a repeatable and controllable process where the cutting thickness was set to be 20 μm, allowing a control over the characteristic dimension of DFs.

The GelMA+DFs composite specimens showed an adhesive interaction between DFs and GelMA network in addition to a tendency of DFs to to assume an entangled state, physically intertwined like a web structure, which acts as a bridge between different spaced points within GelMA network. Porosity and pore dimensions were additionally not influenced by the presence of DFs. For the GelMA+DFs composite, elastic modulus values of 70.8 $\pm$ 5.8 kPa, max strength of 139.3 $\pm$ 10 kPa, max deformation at break 60.8 $\pm$ 2.6 % and toughness of 4 $\pm$ 0.2 J/m^3 were achieved. The elastic modulus almost doubled GelMA value, giving to the composite a more stiff character.

An injectability study, preceded by a rheological characterization, showed that it is possible to inject homogeneously the GelMA solution at 30 and 37 °C by using different needle sizes (18, 20, 22G), showing maximal glide force value for the worst configuration up to 25N. At the same time it was not possible to inject uniformly for temperatures of 20 and 25 °C for all needle tested. A treshold value of injection force was suggested by

EN ISO 7886 1:2018, in order to consider a substance injectable. The model adopted to predict the injectability of non-Newtonian fluids was found to be completely adequate to the experimental results from the injectability tests, showing an increasing discrepancy decreasing needle size and temperature. Composite GelMA + DFs filling may represent a new mini-invasive UV-photocurable way with high compressive mechanical performance to approach the key issues of clinical osteochondral repair with a soft injectable hydrogel material. Some experimental tests are still ongoing, e.g., the injectability force, the swelling behavior and the sol fraction featuring the GelMA + DFs material.

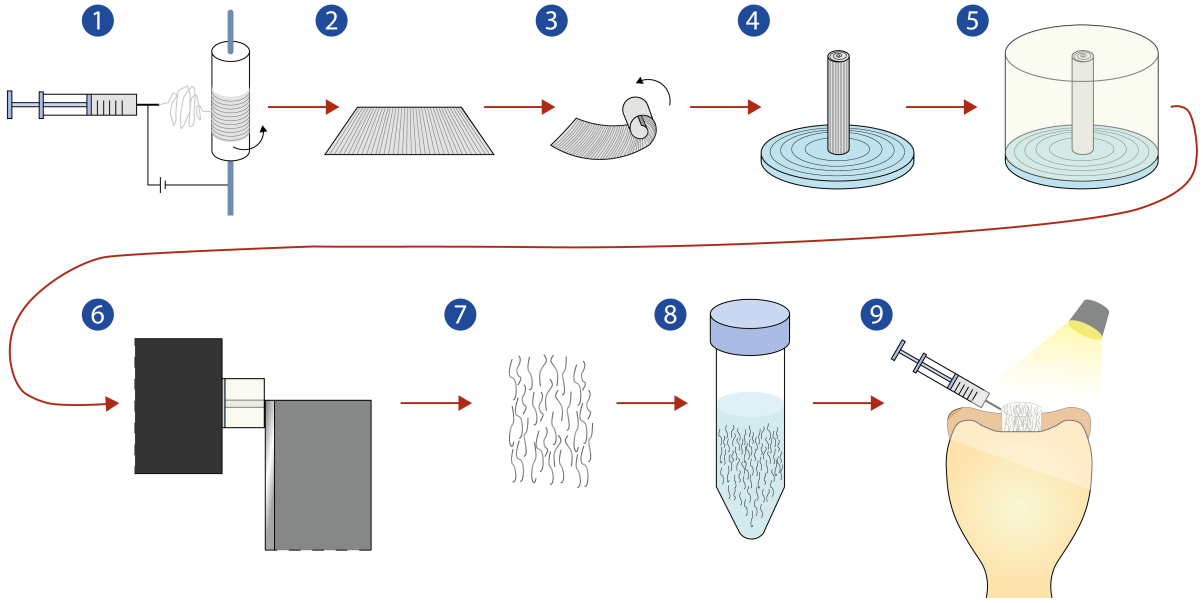

Figure 1: Graphical abstract. (1) Rotating electrospinning set-up. (2) Electrospun aligned fibers mesh (3) Cylindric mesh (4) Cryostat sample holder + cylindric mesh (5) Properly sample embedding in cryomedium (6) Cryostat cutting (7) DFs (8) DFs + hydrogel (9) injection and in-situ photo-curing

Keywords: Osteochondral defects treatment, injectable systems, biocomposite, electrospun nanofibers, cryomicro-cutting technique, dispersed fibers (DFs).

Sommario

I difetti osteocondrali (OD) affliggono milioni di persone ogni anno in tutto il mondo con un impatto socioeconomico notevole. Diversi approcci terapeutici sono stati impiegati ma ancora oggi non esiste un trattamento definitivo e soprattutto un gold standard terapeutico. Tra tutti gli approcci che tentano di rigenerare il tessuto nel modo appropriato, i sistemi iniettabili minimamente invasivi basati sugli idrogeli sono emersi in campo di ricerca. Tra questi, in particolare, gli idrogeli naturali si sono rivelati essere i potenziali candidati; tuttavia, uno dei loro limiti riguarda la perdita delle loro proprietà meccaniche in tessuti portanti, proprio come quello osteocondrale. Dunque, in questo studio sono stata affrontata la possibilità di aumentare le meccaniche di compressione di una rete di gelatina metacrilata (GelMA) attraverso un riempitivo basato su fibre disperse (DFs) costituite da una miscela di PCL/GelMA, al fine di ottenere un composito GelMA + DFs, di cui si è valutata la sua applicabilità come sistema iniettabile. Al fine di produrre le DFs, le maglie elettrospinnate in configurazione random (isotropiche) e allineate (anisotropiche) sono state prima ultrasonicate, portando a risultati non auspicati, rendendo la procedura fallimentare per lo scopo, probabilmente a causa dell'alta plasticità del PCL. In virtù di questo, è stata impiegata una tecnica di criomicrotaglio, che ha permesso di ottenere fibre disperse microstrutturate attraverso un processo ripetibile e controllabile, dove lo spessore di taglio è stato impostato a 20 μm, e questo ha consentito di avere un controllo sulla dimensione delle strutture a fibra. I campioni compositi GelMA+DFs hanno mostrato un'interazione adesiva tra le fibre disperse e la rete polimerica di GelMA, oltre che una tendenza delle fibre disperse ad assumere uno stato fisicamente intrecciato fungendo da ponte rinfornzante all'interno del network di GelMA senza alterarne significamente porosità e dimensione dei pori. Per il composito GelMA+DFs sono stati raggiunti valori di modulo elastico a compressione di 70,8 $\pm$ 5,8 kPa, resistenza massima di 139,3 $\pm$ 10 kPa, deformazione massima di 60,8 $\pm$ 2,6 % e tenacità di 4 $\pm$ 0,2 J/m^2. Il modulo elastico ha quasi raddoppiato il suo valore, con differenze statisticamente significative rispetto alla sola rete di GelMA, conferendo in questo modo al composito un carattere più rigido senza renderlo però più fragile. Inoltre, uno studio di iniettabilità, preceduto da una caratterizzazione reologica, ha dimostrato che è possibile iniettare in modo omogeneo la soluzione di GelMA

a 30 e 37 ° C per le diverse dimensioni degli aghi utilizzati (18, 20, 22G), mostrando un valore massimo di forza di scorrimento per la configurazione peggiore fino a 25N. Allo stesso tempo, non è stato possibile iniettare uniformemente per temperature di 20 e 25 ° C per tutti gli aghi testati. La norma EN ISO 7886 1:2018 suggerisce un valore soglia di forza di iniezione per considerare una sostanza iniettabile è di 10N. Test di iniettabilità sulla configurazione GelMA+DFs sono al momento in corso. Il modello adottato per prevedere l'iniettabilità dei fluidi non newtoniani è risultato non adeguatamente coerente rispetto ai risultati sperimentali dei test di iniettabilità, mostrando, in particolar modo, una discrepanza crescente al diminuire delle dimensioni dell'ago e della temperatura. Il riempimento composito GelMA + DFs può rappresentare un nuovo metodo mininvasivo, fotoreticolabile con UV e con elevate prestazioni meccaniche a compressione, pur essendo un idrogelo iniettabile. Alcuni test sperimentali sono ancora in corso, quali di iniettabilità, di swelling e di sol-fraction per il composito GelMA + DFs.

Parole chiave: Trattamento dei difetti osteocondrali, sistemi iniettabili, biocomposito, nanofibre elettrospinnate, tecniche di crio micro-taglio, fibre disperse (DFs).

Contents

1 | Osteochondral defects and related treatments

1.1. Articular cartilage and osteochondral unit

Nowadays, articular cartilage (AC) is object of worldwide research due to the lack in proper own-regeneration capacity among the population of any age [1]. AC is formed of two types of cartilage, fibrous and hyaline one, the former is characteristic of structures that provide mechanical support such as menisci, while the latter is smoother and more flexible and characteristic of joint surfaces. AC is a highly specialized connective tissue with a proteoglycan gel matrix reinforced with collagen fibers and holds a crucial role in load bearing and load distribution of different joints like the knee. Among joints the knee is a joint subject to high mechanical stress, both in static and dynamic conditions, and represents one of the diarthrosis most involved in osteochondral damage, whether induced by traumatic or degenerative events.

The compression cartilage Young's modulus ranges from 280 ± 160 to 730 ± 260 kPa for the superficial and deep regions, respectively [2]. Others studies reported compression tests performed on the human knee AC, exhibited a full-thickness compression Young's modulus of 581 ± 168 kPa [3] [4]. A further study reported for AC a compressive modulus within a range of 0.51–1.82 MPa in addition to high toughness [5] (fracture energy of 1000 J $\dot{m}^{-2}$). In addition, compressive strength values found in the 14–59 MPa range [6].

The principal functions of AC are to mainly act as a bridge for the transmission of loads to the more robust deeper structure of the bone, especially for joints subject to high loads and provide the proper tribological lucricant interface properties, characteristic of articular joints (ankle, knee, hip, etc.). In order to understand more and more deeply the mechanisms of healing, response to stimuli and the cross-talk between cartilage and underlying bone, the definition of osteochondral (OC) unit is nowadays used to refer to a single entity [7]. It consists of the multilayer cartilage and underlying subchondral bone plate, where the thickness (Fig.1.2a) and the mineralized (Fig.1.2b) component amount

of the subchondral plate change in the same joint and among different joints in function of the bearing state. In the tibial plateau, the thickness of the cartilage unit stays in 2-4 mm range, while the subchondral bone plate unit is in 100-900 μm range, giving to the transversal profile a wavy trend (Fig.1.2a) [8].

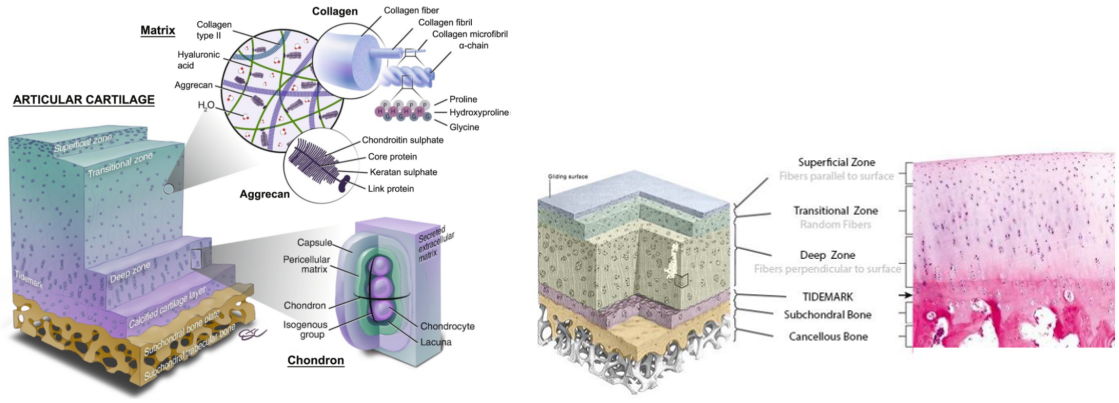

(a) (b)

Figure 1.1: (a) Main components of the articular cartilage tissue: hyaluronic acid, collagen II, cartilage-specific proteoglycan core protein (aggrecan) and water. (b) Histological image (right) of natural tissue, tidemark trend profile is observable (changing in intensity of pink colour) [9]

.

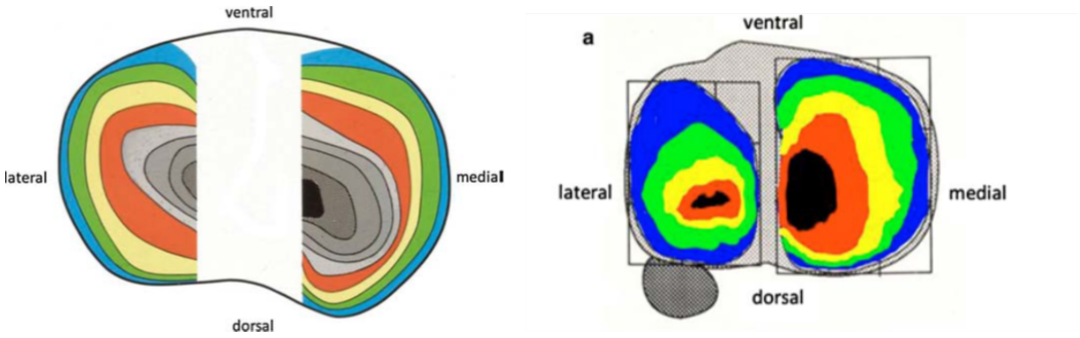

(a) Thickness distribution. (b) Mineral map distribution.

Figure 1.2: (a) Thickness subchondral layer gradient in tibial plateau: from thicker (black, 900μm) to thinnest (light blue, 100 μm). (b) A mineral content gradient is established: from the denser zone (black) to the less dense (blue) [8].

The osteochondral unit could be conceived as a multilayer structure, where each layer is characterized by a specific topography and component amount. It is possible to identify the superficial, the transitional, the deep and the calcified zones for the proper cartilage layer and the subchondral bone plate and subchondral trabecular bone zones for the bone

layer. For proper cartilage layer a phenotype expression is related to the corresponding extracellular matrix (ECM) density and composition, especially regarding the collagen fibers assembling type. Starting from the upper layer and going deeper toward the subchondral bone, the percentage content of collagen type X and glycosaminoglycans (GAGs) increases, increasing the mechanical strength properties, meanwhile the content of collagen II decreases (Fig.1.1a). In the transition zone collagen II forms microfibrils, fibrils and then collagen fibers intertwined with proteoglycan aggregates and these organized structures characterize the AC tissue [10]. Components such as blood vessels, lymphatics, and nerves decrease their presence from the trabecular bone to the compact bone of the subchondral plate, until they disappear completely in the cartilage calcified area (Fig.1.3).

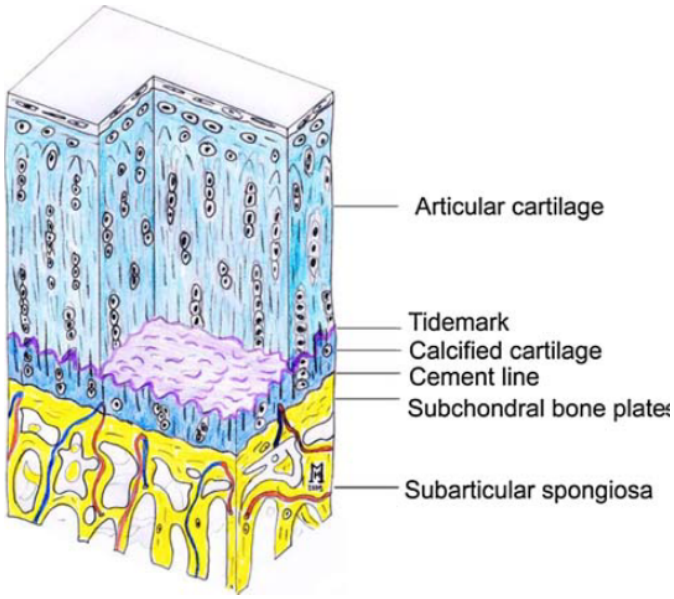

Figure 1.3: Vascular endoff across OC unit between subchondral bone and calcified calrtilage represented by cement line [11].

Therefore, due to the 3D architecture of the OC unit, a nutrient intake gradient is established causing a different cellular expression. Indeed along the thickness of the cartilaginous layer of the OC unit, phenotypically different chondrocytes produce, depending on the regulation of gene expression, different matrix components that ensure a different composition for each layer (Fig.1.4). Regarding the more superficial layer, being without vessels, its nutrient intake depends mainly on the synovial capsule (and synovium), from where the exchange of substances takes place.

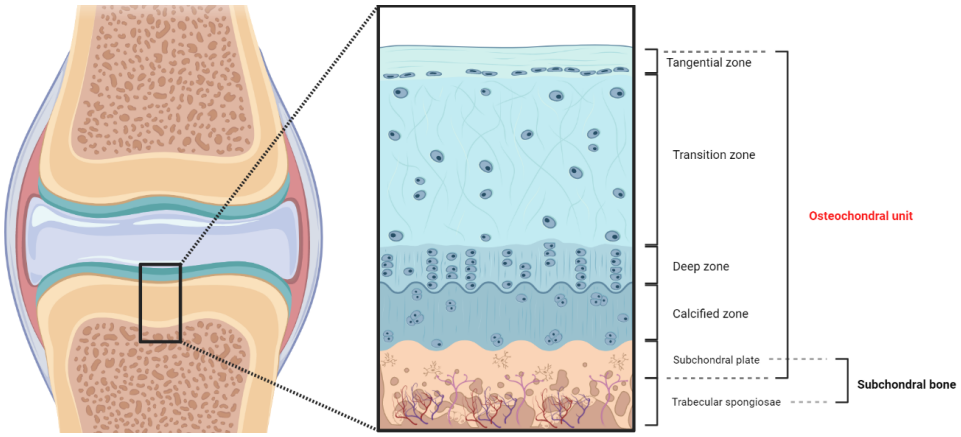

Figure 1.4: Chondrocytes organization within cartilage thickness.

Cells have an elongated and tangential orientation to the articular surface shape in the superficial zone, a rounded shape in the middle zone, a cluster behaviour in the deep zone and a calcified aspect in the calcified zone (Fig.1.4). Based on the different composition of each specific layer, each layer exhibits different mechanical properties with specific ranges of load-bearing conditions. If the load state or distribution within a joint (e.g., weight gain) undergoes abnormal changes, this will have repercussions from a functional point of view in the OC tissue. In support of this, studies have shown that a cyclic state of compression resulting from moderate motor activity favours the nutrients exchange and also affects the proper phenotypic expression of chondrocytes [12] [13] [14].

1.2. OC pathologies and defects classification

Underlying conditions such as osteochondral defects and diseases such as osteoarthritis, osteochondritis dissecans and rheumatoid arthritis, it is possible to identify factors of different natures that contribute to their onset: biological, genetic, infectious but also traumatic. These may lead to a degeneration of the AC, involving also the deep subchondral bone plate layer. In particular, diseases like osteoarthritis (OA) nowadays represent one of the more disabling and degenerative conditions that affect millions of people every year all over the world [1]. A recent systematic review also reported that full-thickness chondral defects occur in 36% of young and active athletes [15]. Given the ageing of the population, a past estimation made for 2020 revealed that there would be 60 million arthritis sufferers in the United States and Europe by that year. The social and economic cost of the disease has been quantified at USD 65 billion, of which USD 15 billion is due to medical costs and the remainder to the quantification of losses in work capacity.

The multifactorial pathology of the disease does not allow an aetiological therapy to be set

up. A further limitation in the treatment of the condition is the lack of a gold standard of treatment, being it surgical or pharmacological, since there has been a lack of uniformity in the response to the various therapeutic approaches [9].

In the context of OA pathology, osteochondral defects can be both the cause and the consequence. In the case of focal osteochondral defects derived from traumatic events, these are important co-factors for the genesis of OA; where the disease is already overt, the outcome can be cartilage degeneration and the development of OC defects [16] [17] [18] [19]. As extreme event, due to the development of the lesions, a degenerative process can start irreversibly, bringing the condition for a total knee replacement as the worst outcome.

According to the International Cartilage Repair Society (ICRS), the osteochondral defect could be classified in four grades (Tab.1.1 and Fig.1.5), starting from the less to the more severe condition, and depending on the depth and size of the lesion.

Table 1.1: Defects classification according to ICRS [20]

Defects grade	**Features**
Grade 0	-Normal conditions
Grade I	-Moderately damaged, nearly normal condition (superficial defect with indentation, fissures or cracks)
Grade II	-Abnormal condition (defect extending to $< 50\%$ of cartilage depth)
Grade III	-Severely abnormal (defect extending $>50\%$ of cartilage depth but not up to the subchondral bone plate)
Grade IV	-Severely abnormal (defect penetrating through subchondral bone)

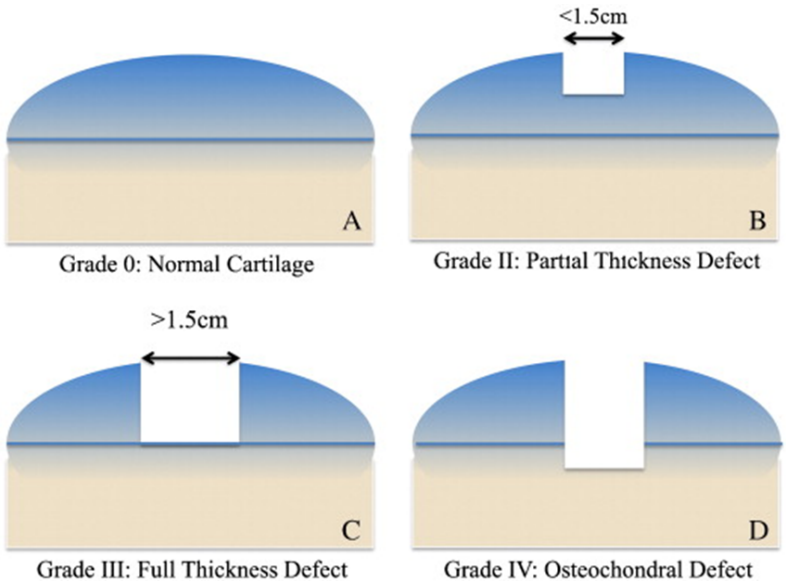

Figure 1.5: ICRS Defects classification [21]

1.3. Current surgical OC treatments

The OC surgical therapies available are classified as palliative, reparative and regenerative treatments. Palliative ones have the objective to temporarily relieve the pain and improve the functional status, avoiding a rapid worsening of the patient condition in the short term. Reparative ones, like arthroplasty, pridie drilling and microfracture, promote the bleeding from the subchondral and underlying trabecular bone, blood clot formation, and consequent recruitment of bone marrow cells and consequent fibrocartilage filling [9].

In the field of regenerative approaches, Autograft (OAT), Allograft (OCA), Autologous Chondrocytes Implantation (ACI), Matrix-Assisted Chondrocytes Implantation (MACI) and Autologous Matrix-Induced Chondrogenesis (AMIC) represent the main approaches for the regeneration of the new tissue. Different advantages and limitations are connected with each type of intervention, the most relevant of which are the high costs related to both cells use and long multistep procedure due to cell isolation and manipulation. In addition, as shared by all presented regenerative techniques, an overall limitation is the need of an open surgery scenario to treat the patient. Problems related to patient fear, general anesthesia, hospitalization and connected sanitary costs remain the main bottlenecks of all of the surgical approaches (Tab.1.2). Among all the regenerative available approaches there is not an overall gold standard. It is important to underlying the wide number of parameters that lead to the choice of the most suitable intervention type: the disease that causes the defect, the stage of the defect, the involvement of other joint elements (e.g., synovium, ligaments, joint muscles), the number of joints involved, patient co-morbidity, patient age, clinical story, economic balance between the type of intervention and expectations of life/overall patient condition.

1.3.1. AMIC devices

AMIC systems (Fig.1.6) are a class of devices that can be implanted through open surgery, inducing autologous ECM production by promoting chondrogenesis in the treated patient.

AMIC products may be considered within the regenerative procedures and are conceived to induce chondrogenesis through the sole interaction between the constituent device materials and the cells of the patient. In particular, in the surgical procedure it is planned to proceed first with a scratching technique in order to make in contact the blood of the patient coming from the underlying bone marrow and related bone mesenchymal stem cells (BMSC), with the device. This procedure has been designed to ensure a BMSCs-device interaction that has been shown to be more effective and efficient in tissue regeneration

Table 1.2: Regenerative procedures [20]

Tecniques	Advantages	Limitations	Defects grade
Osteochondral autograft transplantation (OAT)	-Own tissue -Ability to control depth of the donor graft, facilitating a more congruent coverage and filling of the defect	-Significant donor-site morbidity -Not suitable for big defects	Up to moderate grade III
Osteochondral allograft (OCA)	-Similar ECM composition -High costs -Batch-to-batch variability	-Immunogenicity problems -Short shelf-live -High costs -Batch-to-batch variability	Severe grade IV
Autologous chondrocytes implantation (1^th and ^2nd ACI generations)	-Patient cells -Cells are assisted by a sutured/sealed template (periostium flap or porcine collagene derived membrane)	-Donor-site morbidity -Two-steps procedure -High costs -Problem related to the flaps type	Severe grade III
Matrix-assisted autologous chondrocytes implantation (MACI, 3^rd ACI generation)	-Patient cells -No need for sutures	-Donor-site morbidity -Two-steps procedure -High costs	Severe grade III
Autologous matrix-induced chondrogenesis (AMIC)	-Lower costs -Different types of materials (natural, synthetic or hybrid) -Single step procedure	-Own-cell free structure -Success of the application dependent on material choice -Possible foreign body reaction -Open surgery	Grades III and IV

if compared with the common reparative techniques, like the microfracture one. The features of the most studied AMIC products are reported in Tab.1.3.

Considering the hard limitation of the ex-situ fabrication and related matching site implantation and open surgery procedure (i.e., small defects might be treated alternatively to open surgery with arthroscopic procedure that is challenging and often reserved for experienced specialist surgeons [30]) an overview of the main advantages and limitations is evidenced in Tab.1.3. It is possible to notice a wide variability, among the presented

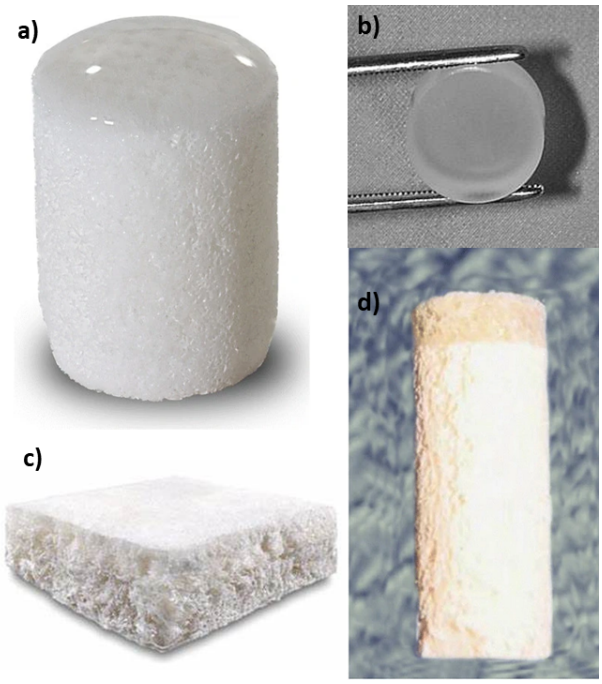

Figure 1.6: a)Agili-C^{TM} (CartiHeal) b)SaluCartilage^{TM} (SaluMedica) c)MaioRegen® (FinCeramica) d)TruFit^{TM} (Smith and Nephew)

AMIC devices, in terms of the type of material constituent, being natural or synthetic, organic or inorganic and in terms of monophasic or multiphasic structures, evidencing that there is not a unique path-tracked option for this type of OC lesions because of questionable clinical outcomes. Since there is not an optimal solution, as unanimously shared by the scientific community today, a common goal should be to try to limit the invasiveness of surgeries as much as possible. This is the reason why several research groups are moving to injectable and minimally invasive approaches. These new systems should not only satisfy the pre-clinical and clinical outcomes at least as much as presented AMIC devices but also have a lower social and economic impact.

Table 1.3: AMIC devices with satisfying information from the literature [22]

Commercial name, company and composition	**Advantages**	**Limitations**	**Ref.**
MaioRegen® (Med & Care) *Type I collagen and magnesium enriched-HA*	-Multilayers structure mimicking natural tissue -Good clinical outcomes on clinical investigation over 5 years	-Fibrous tissue, collagen type I, and fibroblasts presence -Fibrillations, fissures and hypertrophy	[23] [24]
ChondroMimetic™ (TiGenix NV) *Collagen, GAGs and CaPs*	-It showed to support the simultaneous natural repair mechanism of full osteochondral unit	-Fibrocartilage new formed tissue	[25]
TruFit™ (Smith & Nephew) *CaPs and PLGA*	-Good filling of OC defects and good integration in the native cartilage -High percentage of hyaline cartilage formation and good bone renovation in goats	-Granulomatous reactions -Generates acidic degradation by-products -Sub-chondral bone cysts -No improvement in applying this product in comparison to the other procedure	[26]
SaluCartilage™ (SaluMedica) *PVA hydrogel*	-Mimics human cartilage in terms of water proportions -There is no evidence of inflammatory reaction or osteolysis associated with this implant -Clinical results showed improvement of the chondral defects	-Inadequate connection to the bone with risk of dislocation	[27]
Agili-C™ (CartiHeal) *aragonite and hyaluronic acid based*	-Formation of articular hyaline cartilage with a marked grade of collagen type II -Homogeneous proteoglycan expression -Restoration of the subchondral bone plate -Formation of a well-defined tidemark	-Increased transient chronic knee pain and knee swelling -Synovial hypertrophy and exuberant intra-articular scar tissue events	[28] [29]

Note: HA= hydroxyapatite; GAGs= glycosaminoglycans; CAPs= calcium phosphates; PLGA= poly(lactic-co-glycolic) acid; PVA= polyvinil alcohol

2 | Mini-invasive hydrogel systems: ongoing research efforts

Nowadays in different medical fields (neural, cardiovascular, ophthalmic surgeries, etc.) the efforts are directed to switch to minimally invasive surgery in order to expand the pool of patients that can be operated in the same period of time, if compared to the corresponding standard surgical technique, as happen for a large class of cardiac interventions for transcatheter aortic valve implantation [31]. Different injectable materials were developed to overcome the open surgery limitations, starting from bone fillers [32], musculoskeletal and intra-articular therapies [33] , arriving up to nucleus spine replacement [34]. Phosphate-based materials are largely used as injectable pastes for bone regeneration seem to represent a suitable choice as well as a class of materials for osteochondral regeneration. Nevertheless, they did not fully guarantee the chondrogenic potential needed for a proper OC tissue regeneration, so far, even if from a mechanical point of view they show a mechanical performance in line with those desired [35] (see Paragraph 1.1). Recently, in combination with amino acids residues it has been proven a better phenotypic expression of the newly formed osteochondral tissue [36]. This phenomenon is related to the positive effects of the amino acids residues both influence the osteogenic and chondrogenic potential. Since the success of improved regeneration is linked to the biochemical interaction that tissues have with the chemical groups of the material, it is desiderable the use of materials capable of interacting and inducing cells response, like promoting adhesion, migration and colonisation while managing to maintain the correct phenotype or even induce appropriate differentiation.

Hydrogels are three-dimensional (3D) cross-linked macromolecular networks of natural or synthetic polymers with a viscoelastic nature that can swell by absorbing water up to thousands of times of their initial dry weight, confering to these materials quite friendly to water-enriched biological environments such as the human body. Hydrogels can be categorized as reported in Fig.2.1.

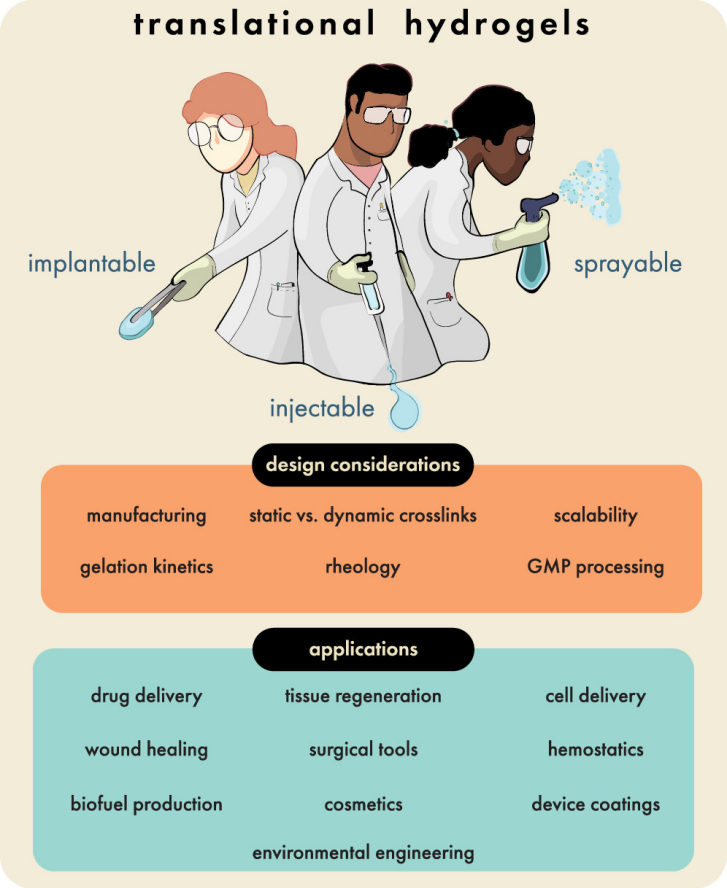

Figure 2.1: Implatable, injectable and sprayable nature of the hydrogels, depending on design considerations whereas the type of target application [37]

Hydrogels can be characterized by different types of crosslinking mechanism between polymer chains, mainly subdivided into chemical and physical mechanisms. The chemical one is characterized by covalent bonds, meanwhile the physical one by weak interactions such as ionic bonds, hydrogen bonds and van der Waals interactions. Depending on the nature and on the number of bonds, the crosslinked hydrogel will show different properties.

Some hydrogels possess self-healing properties, which are related to the non-covalent and reversible bonds, and possess a behaviour capable of countering natural forces and stresses of a body in motion. Self-healing is an advantageous property for exploiting hydrogels as injectable systems. Depending on the nature of the chains constituting the hydrogel and the initial configuration of set parameters (pH, temperature, ions concentration, etc.), specific bonds will be formed. However, if a force field (e.g., increasing in shear stress field) is applied, the bonds may break, and reform once the force field is removed. Therefore, self-healing is defined as the property that enables a material to intrinsically and automatically heal damages, restoring itself to normality and regaining its associated mechanical and

rheological properties [38].

The in situ-gelling platforms exploit specific cues from the body to trigger gelation: physiological temperature, pH, or ionic strength. In addition, others externally induced biocompatible stimuli (e.g., electric/magnetic field application, UV/visible ligtht stimulation) may trigger polymer chain interaction leading to changes in material properties as well. Harsh mechanisms for macromolecular cross-linking (e.g., toxic agents, etc.) meant that gelation needed to occur prior to introducing gels to biological systems. Unsurprisingly, this might limit the bioengineering applications of hydrogels, narrowing its field of use, to superficial environments such as the surface of the eye, an open wound, or an exposed surgical bed (absorbent materials for absorbing haemorrhagic blood). Safer cross-linking mechanisms, as ion mediated by ion-enriched solutions rather than mediated by visible or UV light, were developed to trigger the gelation in situ, allowing a minimally invasive way of administering hydrogels in deeper body organs and tissues, making them injectablesystems.

2.1. Injectable hydrogels

The definition of injectability encloses parameters like pressure or force required for injection, evenness of flow, and freedom from clogging (i.e., no blockage of the syringe needle) [39]. Injectability is a feature that confer the possibility to use hydrogel formulations as gently fillers in different part of the body, injecting them in a liquid or even a gel state in order to adapt to the volume to be filled, exploiting, once gelled, the possibility to switch their behaviour towards a solid state and remaining stable (e.g., in terms of shape rather than volume) in the implantation site. On the whole, injectable hydrogels in a gel state need a predictable control of gelation kinetics during the procedure, which requires transporting the sol or the pre-gel to a targeting site through an injection device [40].

Since hydrogels are viscoelastic materials, they can be generally classified as non-newtonian fluids, i.e., fluids that do not have a linear relationship between viscosity (η) value and applied shear rate ($\dot{\gamma}$). In particular, fluids that see a decrease in their η value as the $\dot{\gamma}$ increases are termed shear-thinning behaviour materials. This nature is a relevant characteristic to be able to evaluate the injectability ranges of the material. A class of shear-thinning hydrogels may be represented by naturally derived materials, that were used as injectable systems to combine the cell-friendly nature and injectability feature. Different types include peptide-based hydrogels, protein-based hydrogels, hydrogels from blends, colloidal systems, and cyclodextrin-based hydrogels [41]. Some synthetic polymer-based hydrogels also have a shear-thinning character and these include poly(N-

isopropylacrylamide) (PNIPAM), poly (ethilene glycole) (PEG) and poly propylene fumarate (PPF) based materials [42].

The viscosity of non-newtonian fluids with a shear-thinning behaviour can be described with a power law equation through the Ostwald–de Waele model (Eq.2.1) [43], where K ($Pa \cdot s^n$) is the consistency index and n (adimensional) is the flow behavior index, as follows:

$$\eta = K \cdot \dot{\gamma}^n \tag{2.1}$$

where a value of n<1 is associated to a shear-thinning behaviour of the hydrogel.

One of the most prominent aspect of injectable hydrogels is to know a priori the application scenario to accomplish an effective treatment, summarized in the parameters listed as follows:

- Injection parameters
  - Temperatures of injection
  - Needle length and diameter
  - Syringe type
  - Glide injection required
- Shape retention in-situ once injected
- Shape recovery for self-healing materials
- Types of stimuli that trigger crosslinking
- Types of interactions with the biological environment
- Morphological and properties changes over time

For applications as OC defect treatments, where the natural tissue to be substituted have strong properties, like the elastic modulus or compressive strength at break values, it is a difficult task to replicate the natural environment, especially with soft materials such as hydrogels.

Indeed, the natural polymer-based hydrogels prepared by the traditional method (e.g., mixing water and natural compound without functionalising the material and/or maximising any crosslinking mechanisms) generally possess poor mechanical strength, which

greatly limits its application prospects for OC defect treatments. On the other hand, synthetic polymer-based hydrogels may be employed for their remarkable mechanical properties tunability as bearing tissue substitutes, but they lose in terms of bioactivity. For these reasons, the concept of hybrid injectable hydrogels [44], both conceived as copolymer or blend systems, made of natural and synthetic hydrogels, was introduced to exploit the advantages of each constituent in order to simultaneously compensate for each component limitations. In addition, a strategy that can be adopted in combination with hybrid systems or as an alternative to the synthetic component is to use structured fillers at different scales (mainly micro and nano scale) to still boost the mechanical performance. The most promising and used natural and synthetic hydrogel materials for OC defects are reported respectively in Tab.2.1 and Tab.2.2 with relative limitations and advantages.

Table 2.1: Injectable natural materials for chondral and osteochondral applications

Natural derived materials	**Advantages**	**Limitations**	**Ref.**
Collagen	-ECM component -Osteocompatibility -High structural integrity -High bioresorbability	-Potential of immunogenicity -Lack of inherent rigidity	[45] [46]
Hyaluronic acid	-ECM component -Good hydration capacity -Good cellular encapsulation -Promotes angiogenesis	-Poor mechanical strength -Faster degradation	[47] [48] [49] [50]
Chondroitin sulfate	-ECM component -Anti-inflammatory nature -Role in cell recognition and signaling	-Rapid degradation in contact with body fluids -Poor thermal resistance -Poor mechanical properties	[51] [52]
Chitosan	-Chondroprotective nature -Structurally similar to GAGs -Antibacterial properties Temperature-controlled phase transition	-Limited solubility at physiological pH -Polycationic and hemostatic properties -Poor mechanical properties	[53] [54]
Alginate	-High functionality -Chelating ability -pH-sensitivity	-Limited in vivo degradation -Poor cell adhesion -Mechanically weak nature	[55] [56]
GellanGum	-Biocompatibility -Biodegradability -Similarity with the extracellular matrix -Easy to functionalize	-Low mechanical properties -Thermosensitivity -Low bioactivity	[57] [58]
Gelatin	-Low cost -Low immunogenicity (respect to collagen) -RGD presence -Possibility of easy functionalization	-Low mechanical strength -Thermosensitivity	[59] [60] [15] [61]

Table 2.2: Injectable synthetic materials for chondral and osteochondral applications

Synthetic materials	**Advantages**	**Limitations**	**Ref.**
Poly(N-isopropylacrylamide) (PNIPAAm)	-Thermosensitivity -Ease of grafting bioactive additives	-Poor cell affinity	[62] [63]
Polyvinil alcohol (PVA)	-Ease of aqueous processing -Good mechanical properties	-Poor cell adhesion -Not biodegradable but bioresorbable	[64]
Poly(lactic-co-glycolic) acid (PLGA)	-Hydrophilicity and biodegradability -Low immunogenicity -FDA approval for various biomedical applications	-Limited bioactivity -Generates acidic degradation by-products	[65]
Polypropilen fumarate (PPF)	-High strength -Injectability	-Limited bioactivity	[66] [67]

In order to widen the use of hydrogels for applications where mechanically performing monolithic systems are currently used, different approaches to increase the mechanical performance of hydrogels were investigated and reported in Tab.2.4.

Table 2.3: Different approaches to increase the mechanical properties of hydrogels [44]

Approach	Advantages	Limitations
Copolymeric hydrogels and blend -Natural/Natural -Natural/Synthetic -Synthetic/Synthetic	-Improved mechanical properties -Tunable chemical and biological properties	-Cytotoxic molecules often involved -Peculiar reaction triggers
Interpenetrated Network (IPN) and s-IPN	-High mechanical properties -Tunable properties -Activated by different external stimuli	-Higher mechanical properties with synthetic material that though do not guarantee acceptable cell friendly properties
Composite -Carbon-based particles -Polymeric particles -Inorganic/mineral-based particles -metal/metal-oxide particles	-Simplicity in assembly -Notable mechanical properties -Smart properties	-Higher costs -Not complete controllable in micro/ scale processes

Copolymeric hydrogels

Conceiving hydrogels as copolymers is an alternative approach to modulate their properties like mechanical, biochemical and also the hydrophobic/hydrophilic character. Copolymers consist of two types or more monomers where each one confers peculiar properties; nevertheless, the main requirement for this type of hydrogel remains the swelling properties that should be guaranteed with at least a hydrophilic part. Copolymer hydrogels are generally prepared by optical or chemical polymerization (synthesis phase) of monomers using a multifunctional agent and an initiator in the presence of a suitable solvent that leads to the formation of chain-polymerized polymer. There are different examples of copolymer hydrogels with tunable properties for OC application (Tab.2.4), if compared with the single component hydrogel.

Table 2.4: Injectable copolymer hydrogels for cartilage and OC applications

Copolymer	Description	Ref.
Methoxy polyethylene glycol–poly(ϵ-caprolactone) copolymer	-Cartilage formation increased with hydrogel implantation time -Maximal expression of glycosaminoglycans, and type II collagen reached at 6 weeks post-implantation	[68]
Poly(ethylene glycol)dimethacrylate copolymer	-Integration of neocartilage with surrounding native cartilage improved with time -Resulting in the development of tight integration interface -Photoencapsulated chondrocytes were capable of survival and proliferation over time	[69]
N-acryloyl glycinamide–N-[tris(hydroxymethyl)methyl] acrylamide copolymer	-Significantly acceleration of cartilage and subchondral bone regeneration in a rat model	[70]
Chitosan-poly(N-isopropylacrylamide) copolymer	-Provide mechanical support for cell growth -Induce stem cells to differentiate into osteochondral lineages	[62]

However, looking at what has been done in the literature, one of the main limitations of hydrogels designed as copolymers are their missed injectability, due to the need of a crosslinking mechanism that requires chemicals that are generally toxic to cells, thus greatly narrows the field of materials from which to draw.

Semi-interpenetrating (s-IPNs) and interpenetrating networks (IPNs) hydrogels

An additional approach consists on the multiple crosslinking of different hydrogels designed as a semi-interpenetrated polymer networks (s-IPNs) and as interpenetrated polymer networks (IPNs), namely double entangled polymeric networks, in a way to have a similar scenario as copolymer hydrogels, obtaining high mechanically performant systems. In s-IPNs, a single chain crosslinking occurs, resulting in a polymer mesh where the sec-

ond polymer chain type remains trapped. In IPN, a topologically interlocked crosslinking of polymer chains occurs and each of these polymer networks will be characterised by bonds formed between chains of the same type. Interactions between chains residues of the same polymer may take place in order to have an assembly property of every network separately as shown in Fig.2.2.

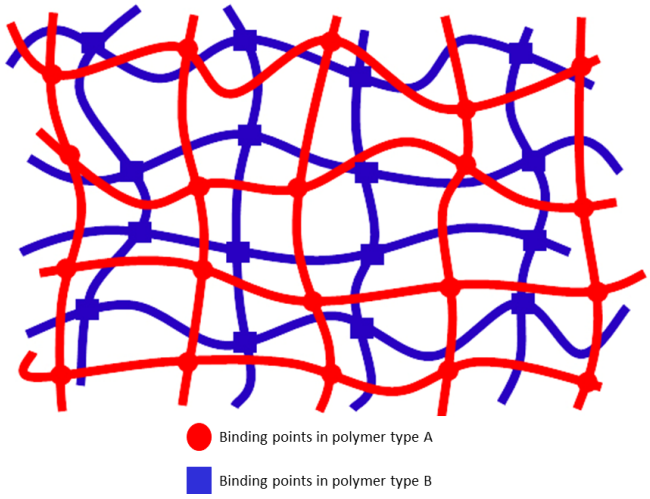

Figure 2.2: Polymer chains type A and polymer chains type B with intranetwork entanglements points

The development of IPN systems arose from the need to exploit the dual crosslinking mechanism to tune the mechanical and rheological funcionality. This approach increases the different functional aspects when compared with single network (SN) hydrogel design, as exploiting a more hydrophilic nature of a chain type rather than promoting cell adhesion through the presence of chemical residues capable of binding to specific cell receptors; or even inserting a type of chain capable of cross-linking by creating strong covalent bonds that greatly increase the mechanical properties of hydrogels. Indeed, it may be possible to modulate the hydrogel properties, in terms of cellular interactions (promoting adhesion, migration, colonisation, differentiation/maintenance of the phenotype, etc.), mechanical, degradation rate, based on the nature of the chains that constitute the IPN. A wide range of physical or covalent crosslinking methods have been investigated for the formation of IPNs, with synthesis occurring primarily through either sequential or simultaneous crosslinking [71].

Table 2.5: Injectable s-IPNs and IPNs hydrogels cartilage and OC applications

Network type	Components	Description	Ref.
IPNs	*1)* Chondroitin sulfate-methacrylate (CSMA) and hyaluronic acid-methacrylate	*1)*Hydrogel could upregulate cartilage-specific gene expression and promote the chondrocytes secreting glycosaminoglycan and collagen II	[72] [73] [74]
	2) Alginate and gelatin methacryloyl (GelMA)	*2)* Supported chondrogenesis in vivo, with the controlled release of TGF-β3 promoting significantly higher levels of cartilage-specific extracellular matrix deposition	
	3) Gelatin methacryloyl (GelMA) and chitosan	*3)* IPN structure can greatly enhance the mechanical properties of GelMA-CS hydrogels compared to the single network CS or GelMA and excellent biocompatibility for bone mesenchymal stem cells	
s-IPNs	*1)* Hyaluronic acid and hydroxyethyl-methacrylate-derivatized dextran	*1)* Excellent viability observed for encapsulated chondrocytes and stable constructs with in cartilage range mechanical strengths	[75] [76]
	*2)*Fibrin and alginate	*2)* Fibrin guarantee cell proliferation and alginate improved biostability, better supported glycosaminoglycan and collagen II production and chondrogenic gene expression	

As reported in Tab.2.5, different s-IPNs and IPN systems were investigated for OC appli-

cations and are mainly based on natural networks. The most promising work reported, which showed better regenerative outcomes, suggests that the components consist of natural, rather than synthetic, polymers. This aspect may be related to the fact that have a synthetic bulk component that has a gentle in-situ crosslinking mechanism with the contemporary ability to harden the structure, keeping unchanged the cellular outcomes, is challenging. However, among synthetic materials, a promising study [64] has highlighted the possibility to obtain an injectable hydrogel based on polyvinyl alcohol (PVA) with highly modifiable mechanical properties depending on the percentage of cross-linking agent. Although the use of such crosslinking agents is controversial with regard to a possible danger to humans, even if the study presents the injectable hydrogel with in-situ crosslinking mechanism as cytocompatible for 3D cell culture and able to promote cartilage repair. In another study [77] ultrahigh toughness PVA-based hydrogel with fracture stress over 7 MPa, shows excellent mechanical performance for cartilage tissue application, even if it was not conceived as an injectable system.

Thanks to its biocompatibility and bioresorbability, PVA is a synthetic material that can be used as an injectable hydrogel system with the possibility of gelling through ionic crosslinking using boron-derived substances such as borax or acid derivatives, as previously reported [64]. A more in-depth study of the possible use to be part of an injectable system for OC applications cannot be ruled out.

Moreover, analysing the natural components, an important aspect is the possibility of undergoing functionalisation to modify the properties of the material. In particular, methacrylation is a process that can be applied to a wide range of natural materials, making them photocrosslinkable, increasing their mechanical properties. Gelatine-based materials occupy a not inconsiderable place in the relevant literature, especially for IPN structure, as reported in Tab.2.5. Gelatin-based materials, being derived from collagen, have intrinsic cellular interaction properties due to the presence of the RGD domain in their structure and have been tested in a variety of applications, such as OC substitutes [78] [79]. They can also be exploited as injectable systems and can undergo, if properly functionalised, a hardening triggered by particular stimuli once injected. In addition, the introduction of methacrylate groups to the amine-containing side groups of gelatin can be used to make it lightcrosslinkable into a hydrogel, namely gelatin methacrylate (GelMA) [80]. However, the application of simple GelMA-hydrogel on cartilage tissue engineering, despite its injectable and photo-crosslinkable properties, was limited due to its poor strength and fast biodegradation rate [81], although it has promising properties in terms of cell interaction.

Composites hydrogels

Micro and nano materials have emerged as promising biomaterial additives to effectively enhance the mechanical and biological properties of biomaterials. Composite hydrogels consist of a matrix material and a filler that can vary depending on which property is to be modulated to have tailored functionality. The common fillers are carbon-based materials (carbon nanotubes (CNTs), graphene, nano diamonds), polymeric elements (polymer particles, dendrimers, fibers structures and dispersed short fibers (DSFs)), inorganic like ceramic particles (hydroxyapatite, silica, calcium phosphate), and metal/metal-oxide particles (gold, silver, iron-oxide). The combination of these structured elements with a polymeric hydrogel network allows to obtain composite hydrogels. Each of these structured elements may interfere with the material properties, once embedded, according to its nature. The chemical interactions between fillers and matrix hydrogel may lead to a interesting integration of properties depending also on hydrophobicity/hydrophilicity ratio between both components. If the objective of the filling is to act on the mechanical properties of the bulk material, it will be necessary for the structured filling component to compensate for the deficiencies of the bulk material or to act in synergy with it. Therefore, 3D shape of the filler and also the characteristic dimensions as well as the quantity are relevant filler parameters for a proper composite design.

Structured elements have been embedded in hydrogels maintaining injectability for OC applications, in order to impart certain specific characteristics as increased bio-adhesion, confer lubricity as happens for GO nanoflakes, increasing mechanical properties like tensile modulus as shown for CNTs, confer the ability to entrap hydrophobic or hydrophilic drugs with polymeric micelles, particles gels, and core-shell polymeric particles for drug delivery purpose [82]. As reported in Tab.4.1, different types of fillers were employed to confer different features to the system, even in combination with cells or with specific molecules.

Nevertheless, being able to have such precise control over the fabrication of elements with micro and nano length scale is very complex. To date, several fabrication techniques were developed to produce, with a high precision, different micro and nano structured elements, reducing a low as possible the stochastic impact on all the fabrication steps. Additive manufacturing techniques have developed over time precisely to try to make these fabrication limitations less impactful.

Table 2.6: Composite injectable hydrogels for cartilage and OC applications

Bulk material	**Filler type**	**Description**	**Ref.**
Sodium alginate and agarose	Bioglass	Stimulate the hyaline cartilage and subchondral bone regeneration in an entire osteochondral unit and promote the integration between the newly formed tissues and the host tissue	[83]
Gellan gum and poly (ethylene glycol) diacrylate	Graphene oxide	Antiwear properties and absence of cytotoxicity effects	[2]
Collagen-alginate	nHA	Better mechanical properties, cell viability, faster cell proliferation and upregulated hyaline cartilage markers if compared to a nHA-free structure	[84]
Fibrous protein (keratin), triblock copolymer (Pluronic), and chitosan	Laponite	Good cell adhesion depending on their formulation and microstructure	[85]
Type II collagen, hyaluronic acid and polyethylene glycol	Magnetic particles	Responsivity to an external magnet while maintaining structural integrity with normal and consistent morphology of BMSCs	[86]
Sodium alginate/carboxymethyl bacterial cellulose	nHA e calcium carbonate	Gelation time and mechanical properties could be regulated increasing to 150%–300% compared with common alginate hydrogels	[87]

Additive manufacturing and electrospinning technique Additive manufacturing (AM) is a key enabling technology to realize a vision of precision biomaterials in the clinic. AM provides freedom of design, device customization, contemporary multimaterial fabrication, ability to produce parts with complex geometry and also enables customization at a reasonable cost. AM techniques were widely used in order to manufacture different shaped materials. In order to have precisely structured elements different AM fabrication

techniques were developed and could be classified as stimulate-triggered or deposition-based (Fig.2.3): different electrospinning set-ups, electrowriting and direct inject-printing but also 3D-bioprinting approach and stereolithography [88] [89].

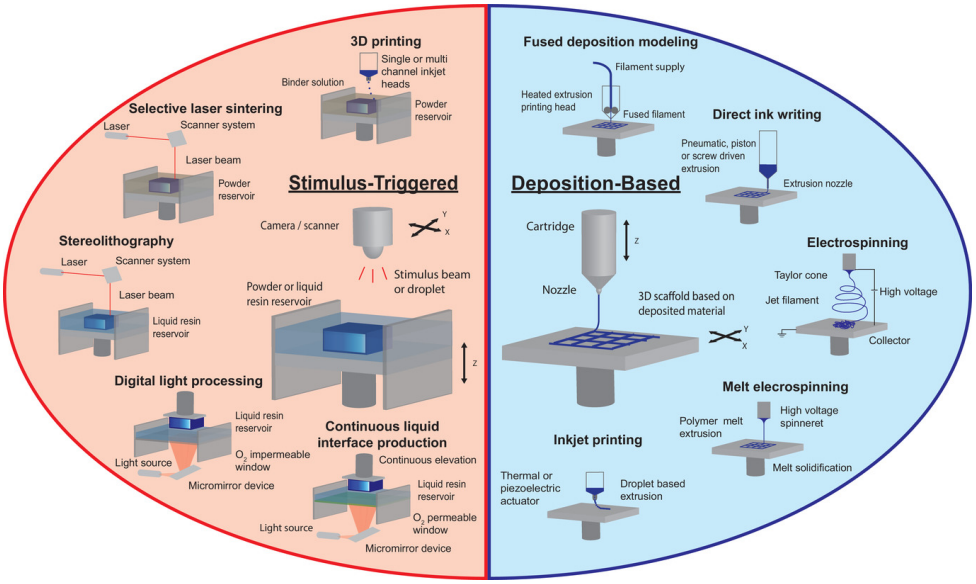

Figure 2.3: AM techniques divided into stimulus-triggered (left) and deposition-based areas (right) [90]

Among those presented, electrospinning represents one of the most studied and used for various applications in the biomedical field because of its simplicity, low cost, and suitability for natural and synthetic polymers [91]. Electrospinning is a common technique to produce interwoven and nonwoven meshes of thin polymeric fibers, in a dimensional range that lies between the micro and nano scale. A high voltage electric field is applied, having as pole the polymeric solution, to create an electrically charged jet of polymer from the end of the needle, which is ejected from the tip of a Taylor cone and gathered on a grounded collector of different various geometry (Fig.2.4).

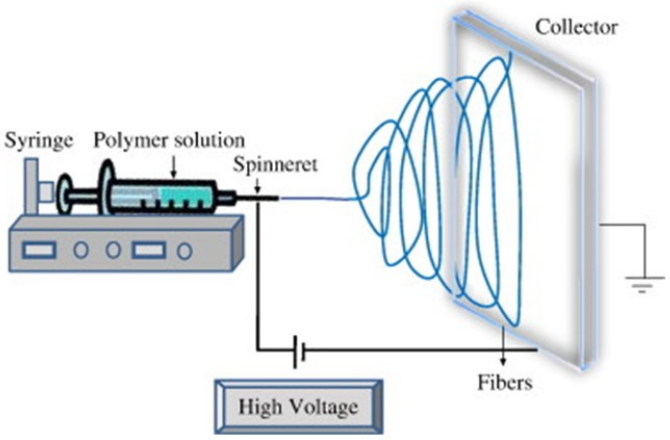

Figure 2.4: Electrospinning principle of operation [92]

While electrospinning was initially applied in the formation of bulk scaffolds for tissue engineering and drug delivery, the introduction of melt electrospinning writing (MEW) improved the control over the alignment of deposited fibers, thus, resulting in biomaterial fabrication with enhanced tensile properties [90]. However, with some specifics set-ups is possible to obtain oriented fibers with a preferential orientation direction that posseses enhanced tensile properties as well. In different studies [89] [93] [94] [23], authors have exploited some structured fibers, being them conceived as a 3D template where cast a hydrogel matrix or utilized them as broken and quasi mono dispersed short fibers reinforcement. Particular attention has been and still is being paid to the possibility of using electrospun meshes, if properly processed, to obtain dispersed short-fibers (DFs) that can be embedded within inks or soft materials in order to simultaneously impart different properties to the bulk material. Prominent examples are exploiting these nearly dispersed short fibers to increase mechanical properties rather than conferring an anchor site or a preferred direction for both growth and load transmission for cells [95]. Therefore, DFs if placed in a bulk material, may expand their use in different applications [94].

Different biomaterials could be processed to obtain electrospun fibers such as Polycaprolactone (PCL), Poly L-lactic acid (PLLA), Polyethilen glycol (PEG) and others [96]. Among these materials, PLLA and PCL were used to obtain DFs, and was investigated

the scenario of use them loading in bulk materials [97] [98]. Both PCL and PLLA are slowly degrading polymers, but their biocompatibility resulting from degradation is quite different [99]: the degradation subproducts of PLLA have been demonstrated to acidify the related ambient. In addition in a study it was hypothesized that for PLLA screws it was observed a foreign body reaction associated to the combination of a biochemical and biomechanical reaction of the crystal-like PLLA fragments. Therefore, in order to use fibers elements based on a performing biopolymer, PCL could be a good candidate to be used due to its features such as good mechanical properties and relative biocompatibility and biodegradation, in addition to a good processibility and relatively low cost [98].

Beyond different reported shortening fibers techniques, such as ultrasonication [100] [97], homogenizing [101], chemical treatment [102] and patterned UV-crosslinking [103]and electrospinning/microcutting methods, enable the production of dispersed short fibers [104] [105]. Biomaterials like poly-ϵ-caprolactone (PCL), poly L-lactic acid (PLLA), poly L-glycolic acid (PLGA) might be the main biopolymers in the biomedical field to be treated with the presented method to be embedded in different system types as short fibers reinforcement. However, each technique presented has its own limits of applicability to certain materials and has technological limitations. For example, to carry out fragmentation techniques with chemical reactions, there must be the right chemical matching that allows the formation of fibres that maintain morphology, because chemical treatment may often induce a partial degradation of the material. Techniques such as ultracentrifugation or ultrasonication, on the other hand, do not allow for accurate process control and repeatability. Instead, electrospinning/micro cutting techniques, even though they are multistep techniques involving the use of different types of instrumentation and skilled samples manipulation, allow for greater control and repeatability in the process than those just presented.

Objective of the thesis

Articular cartilage is a finely organized tissue consisting of four overlapping layers (superficial layer, transitional, deep and calcified) in a contiguous relationship with the underlying compact bone. To date, OD represent one of the most significant problems worldwide in epidemiological, economic and social terms. Among treatments of osteochondral defects, regenerative ones aim to induce the regeneration of tissue having a composition as similar as possible to that of the native tissue. Some treatments rely on the use of autologous cells that require multi-step manipulation procedures as well as high costs. Others, however, take advantage of heterologous implants whose limitations are mainly issues of immunogenic response. To date, all regenerative approaches rely on open surgery techniques causing patient fear, hospitalization, increased risk of infection and slow recovery of function. Research is now shifting toward the development of injectable systems that, while ensuring clinical outcomes comparable to those of other treatments in use, also allow a minimally invasive approach, capable of inducing osteo- and chondrogenesis (intrinsically or through the use of drugs or biological molecules) to such an extent that cell embedding could be ruled out. With regard to osteochondral applications, where the bearing state exceeds that sustainable by natural-based hydrogels, the effort of researchers has been to increase their mechanical properties through different approaches, for example by considering interpenetrated systems (semi and double network), creating copolymerics or composite hydrogels. Particularly regarding the first two approaches, the introduction of a synthetic component, either as a crosslinked network for IPNs, as blended chains for s-IPNs, or as a constituent monomer in copolymers, acts as a reinforcement over a single natural phase.

With regard to composite systems, interest has been focused on the popular biopolymeric fiber-based fillers, such as poly-ϵ-caprolactone. Fiber-based fillers may be used both as bulk frames where the hydrogels may be cast inside, and again, if properly processed, as dispersed fibers. These may be obtained from the forerunner meshes fiber through post-processing techniques as electrospinning/microcutting techniques. In this regard, to focus on the injectability of systems, the optimal approach has proven to be the use of dispersed fibers that allow for increased mechanical properties.

Therefore, the overall objective of this project would be the analysis of the combination (both as s-IPN and IPN systems) of gelatin-based (GelMA) and poly vinil alcohol (PVA), as an injectable system with a fiber-based filler based on a PCL:GelMA blend, in order to investigate a hybrid IPN composite system with enhanced mechanical properties and satisfactory cytocompatibility and tissue regeneration capacity.

In light of this, the primary objectives include the production of electrospun fibers in such a configuration that they be post-processed obtaining dispersed fibers according to a repeatable and controllable procedure. These fibres are inserted as reinforcement in a GelMA-based hydrogel system and their ability to increase the mechanical properties of the resulting composite is tested, upon UV-based crosslinking. In addition, a study of the influence of temperature ranges below a critical threshold of required injection force of the GelMA solution employed is investigated, in order to evaluate the possibility to the need of a thermostatic injection system and to be able to inject, according to EN ISO 7886-1:2018, below a selected force value, with setted injection configuration.

3 | Materials and Methods

3.1. Materials

Gelatin from porcine skin (Gel, type A, strength: 300), methacrylic anhydride (MAA, 94%), poly-ϵ-caprolactone (PCL, Mn 80.000), 2-Hydroxy-4'-(2-hydroxyethoxy)-2- methyl-propiophenon (Irgacure 2959), glacial acetic acid (AA, 99%+), PolyFreeze, glycerol (99%+), sodium citrate monobasic (99%+), ninhydrin, deuterated water (D2O) and phosphate buffered saline tablet (PBS, w/o Ca^{2+} and Mg^{2+}) were purchased from Merck.

3.2. Hydrogel preparation

3.2.1. GelMA synthesis

GelMA was synthetized as reported by *Loessner et Al* [106]. Briefly, Gel was soaked in pre-heated 50 °C PBS or deionized water (DIW) to reach a final concentration of 10 %w/v and the solution was magnetically stirred for 1 h at 50 °C. The effect of functionalization bath (PBS or DIW) on the outcome degree of functionalization will be investigated. MAA was slowly added with a 0.6 g for each gram of Gel, with a 1 mL/min rate. Once MAA was fully added, the solution was left to react for 2h under gently stirring, keeping the temperature at 50° C. Then, the obtained white and opaque solution was poured into 50 mL tubes and centrifugated (refrigerated benchtop centrifuge, Sigma 3-16 KL) at 4000 rpm/min for 5 min at 37 °C to separate the clear GelMA solution (supernatant) from the bottom pellet (unreacted MAA). The supernatant was then collected and diluted with pre-heated DIW at 40°C with a 1:2 volume ratio. Then the diluted solutions was poured in a 12-14 kDa MWCO dyalisis membrane (Spectra/Por, Spectrum laboratories, Inc), and dialyzed against 40°C distilled water for 7 days in order to remove the unreacted MAA. The DIW was renewed three times a day for the first three days and two times a day for last four days. The GelMA solution was poured in 50 mL tubes with 20-25 mL aliquots, frozen in a -80°C for 1h and dehydrated through a freeze dryer (FreeZone 2.5 Plus, Labconco) for 7 days, obtaining approximately 03-04 g for each 50mL-tube. The

tubes were then stocked in -80°C freezer, ready for following use. For all the steps, the material was covered from direct light sources with aluminum foil.

3.2.2. Electrospun nanofibers fabrication and post-processing

Blend solutions preparation

Electrospun fibers prepared by using polymeric solutions at a concentration of 10 and 20 % w/v of PCL and PCL75:GelMA25 in AA, were fabricated as described in the following Paragraph. Briefly, PCL (7,5 and 15 % w/v) was dissolved in AA and stirred overnight at room temperature (RT) in a sealed glass flask. GelMA (2,5 and 5 % w/v) was dissolved in AA and stirred for 1 h at RT in a sealed glass flask. Then, the GelMA solution was added into the PCL solution at 1:3 (GelMA:PCL) ratio and stirred for 1 h to achieve a homogeneous blend. The solution was collected avoiding bubbles formation in syringe (5 mL/syringe) to be used during the electrospinning process. All steps have been performed under a chemical hood.

Electrospinning procedure

Two different homemade electrospinning set-up were used to fabricate two mesh types. The concentration of the electrospinnable solutions was optimized starting from a 10 % w/v of polymer concentration for both PCL and PCL75:GelMA25 solutions, in order to have beads-free electrospun meshes. An isotropic random fibers mesh and an anisotropic (aligned) fibers mesh were fabricated by using the solution of PCL75:GelMA25 in AA at 20 % w/v. A syringe pump (Single syringe infusion pump SP100iZ, Word Precision Instruments) was connected alternatively to both configurations.

For the fabrication of the random fibers, a flat collector covered with an aluminium foil was used as the anode, while the needle of the syringe was used as the cathode (Fig.3.1a).

Instead, for the fabrication of the aligned fibers, a metallic rotating mandrel (Fig.3.1b) and the needle of the syringe were used as the collector/anode and the cathode, respectively. Two types of fibers with different orientations (aligned and random) were fabricated with the intent of investigating the optimal configuration to easily fragment the fibers with ultrasonication and via cryo-microcutting (Cryostat YD-1900, JINHUAYIDI), and obtain different outcomes in terms of geometry of the processed fibers. The electrospinning parameters for both flat and rotating configurations are reported in Tab.3.1.

The resulting meshes were left under a chemical fume hood overnight to allow the AA solvent to evaporate and to obtain well-dried samples. Subsequently, the aluminium foil

Table 3.1: Electrospinning parameters for the two different configurations

Parameter	Flat configuration	Rotating configuration
Electric applied field	- 16 kV	- 16 kV
Syringe type	- Terumo 10mL	- Terumo 10mL
Needle type	- 20 Gauge(0.812 mm)	- 20 Gauge(0.812 mm)
Syringe rate	- 0,5 mL/h	- 0,5 mL/h
Distance between the tip of the needle and collector	-13 cm	-13 cm
Time	- 10 min	- 1 h
Drum collector diameter	- /	- 12,5 cm
Speed	- /	- 2000 rpm/min
Room temperature	- 26-28 °C	- 26-28 °C
Relative Humidity	- 35-37 %	- 35-37 %

was cut into 1x1 cm^2 square pieces. In order to facilitate the detachment of the mesh, the samples were sonicated in an ethanol bath for 30 sec. At this point, by manipulating the sample in an ethanol-filled petri dish, the meshes were gently peeled away from the aluminium foil and allowed to remain in a floating lying configuration. The volume of ethanol at this point was removed with a pipette while still preventing the sample from curling up. The sample was left overnight under an chemical hood to ensure ethanol evaporation. The samples were stored in -20 °C ready for further manipulation.

Ultrasonication and cryomicro-cutting technique for DFs fabrication

In order to obtain DNFs, two approaches based on the ultrasounds and the mechanical cryo micro-cutting were investigated for the disaggregation of electrospun mesh fibers. Two different ultrasonication processes (Tab.3.2) were tested with a sonicator (SONOPLUS HD 4050, Bandelin) with the aim to obtain disperse fibers through ultrasonication by exploiting anisotropic aligned fibers and isotropic fibers (random fibers), following as previously reported parameters by *B. Niemczyk-Soczynska et Al* [97].

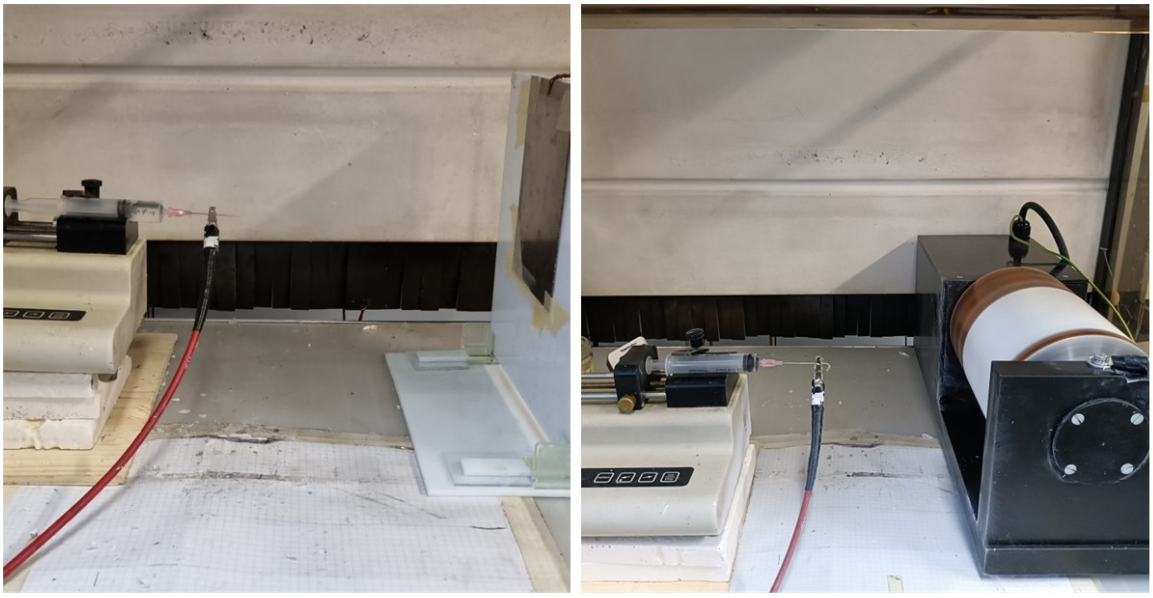

(a) (b)

Figure 3.1: Homemade set-ups. a) Flat elctrospinning configuration. b) Rotating mandrel configuration

(a) (b)

Figure 3.2: (a) Cryostat microcutting configuration. The circular white frozen sample advance with a pass of 20 µm toward the blade. The slices drop down on a metallic binder (b) Schematic illustration about how cryostat works.

On the other hand, the cryomicro-cutting technique was applied to the anisotropic aligned electrospun mesh in order to obtain the side fibers dispersion. Briefly, the obtained mesh chunk (see section 3.2.2-"Electrospinning procedure") was weighted, rolled in the

Table 3.2: Ultrasonication implemented configurations

Parameter	Configuration1	Configuration2
Tip type	- TS102	- TS103
Ultrasonication time	- 45 min' & -90 min'	- 90 min'
Amplitude [%]	- 80%	-80% & -95%
ON/OFF operation mode	- 1sec/1sec	- 1sec/1sec & 2sec/1sec
Sonicated volume type	- DIW	-DIW & Ethanol50:DIW50
Sonication volume	- 5 mL	-10 mL
Sonication tube temperature status	-Exposing to RT air & -Dipping in an ice bath	-Dipping in an ice bath

direction of the fibers (obtaining a cylinder-like structure) and frozen in the Polyfreeze cryomedium perpendicularly to the cryomold surface. The frozen block was cut with the cryostat (Fig.3.2a) using a 20 μm slicing thickness, perpendicularly to the aligned fibers orientation (Fig.3.2b). The frozen slices were collected in a tube and, once the cryomedium liquefies, the viscous solution containing the DFs was diluted with DIW (1:3 ratio), then washed and centrifugated sequentially at 4000rpm/min for 5 min'. The DFs, accumulated at the bottom of the tube, were collected and then freeze-dried and ready for further characterization and use.

3.2.3. Photocrosslinking step

GelMA was dissolved in DIW at a concentration of 10 % w/v. To obtain the DFs-loaded GelMA (GelMA+DFs), the DFs at 0.5% w/v were added separately to the GelMa solution and gently mixed avoiding bubble generation. Separately a solution of Irgacure 2959 with a 0.5% w/v concentration was prepared in DIW at 80° C, magnetically stirring for 1 h and coll to RT. Then, the GelMA and Irgacure solution were mixed in order to have a photo-crosslinking upon exposure to UV light. Both solutions were respectively poured in a cylindrical mold (diameter: 7 mm, height: 5 mm) temperature $>$ 25° C to avoid gelation. By a UV light source working at 365 nm (Lightniningcure LC5 lamp, Hamamatsu) a UV light intensity of 3,5 W/cm^2, detected with a UV light meter (PCE- UV34), was applied for 2 min [107]. The distance photo-crosslinking of 1 cm was used in order to irradiate the entire surface of the specimens [50]. The samples were gently pulled out and ready to further characterizations.

3.3. Chemical characterization

Qualitative Fourier-transform infrared spectroscopy (FTIR) analysis, quantitative proton nuclear magnetic resonance $^1H - NMR$ and the ninhydrin assay were performed to evaluate the presence of methacryloyl groups and the degree of methacrylation.

3.3.1. FTIR analysis

FT-IR spectra were collected in attenuated total reflection (ATR) mode, on purchased raw dry Gel powder and on GelMA flakes, using an IRAffinity-1 FT-IR spectrophotometer equipped with an ATR MIRacle-10 accessory (Shimadzu Scientific Instrument, Japan). The analysis was carried out to qualitatively evaluate the methacrylation of GelMA alone and to verify the presence of GelMA on electrospun mesh.

3.3.2. Ninhydrin Assay

A ninhydrin assay was performed as follows. Gel and GelMA were dissolved in DIW at 3.5 mg/mL for 1h at 40 °C. Then, sodium citrate monobasic (0.5 M in DIW) was added to glycerol at the ratio of 1:2. Ninhydrin powder was dissolved in the sodium citrate monobasic/glycerol solution to reach a final ninhydrin concentration of 2.5 mg/mL. To calibrate the assay, four Gel-based solutions were prepared at different dilution (25, 50, 75 and 100% (w/v) starting from the previous Gel solution). Then, 50 μL of DIW (for blank samples), 50 μL of each Gel dilutions and 50 μL of GelMA were added in 2 mL tubes containing 0.950 mL of ninhydrin solution. Each sample was left to react at 50 °C for 12 min and then cooled down at RT.

For absorbance measurements, 250 μL of each solution were poured into a 96-well plate (n=3) and the optical absorbance at 570 nm was measured with a plate reader (VICTOR Nivo Multimode Plate Reader, Perkin Elmer).

The average absorbance results of the calibration samples were plotted versus the concentration of Gel dilutions (0 for blank, 25, 50, 75 and 100%, 100% is equal to non-diluted Gel solution at 3.5 g/mL) and a linear regression was used to obtain the calibration curve. The absorbance at 570 nm corresponds to the concentration of free amine groups and any reduction in free amine concentration is due to the methacryloyl functionalization.

The measured absorbance of both GelMA dissolved in PBS and DIW solutions was then used to obtain from the standard curve the corresponding Gel dilution value. The DoF was calculated as reported in Eq.3.1 where the X is the GelMA concentration. A comparison

of two baths (DIW and PBS solution) used during GelMA preparation was evaluated to assess the impact the bath has on the degree of GelMA functionalization.

$$DoF(\%) = (100 - X)\% \tag{3.1}$$

3.3.3. ^{1}H-NMR analysis

A contemporary confirmation of the methacrylation degree (%) was obtained with a ^{1}H-NMR analysis. The ^{1}H-NMR spectra were recorded by using a Bruker Ascend 400 instrument, at 37 ° C on both Gel and GelMA solutions dissolved in D_2O with 5 mg/mL concentration (n=1). The spectra of both Gel and GelMA were normalized to the phenylalanine peaks in 7.1-7.4 ppm signal. The 7.1-7.4 ppm range is considered as the standard (no modifications by reaction with MAA). Moreover, the 2.8-2.95 ppm signal of the lysine methylene peak was used to calculate the substitution degree due to the fact that the lysine is the bonding site for the methacryloyl conjugations. [108]. The DoF was calculated by using the Eq. 3.2:

$$DoF(\%) = \frac{\int Gelatin_{(2.8-2.95ppm)} - \int GelMA_{(2.8-2.95ppm)}}{\int Gelatin_{(2.8-2.95ppm)}} \cdot 100 \tag{3.2}$$

3.4. Rheological analysis

An Anton Paar modular compact rheometer (MCR 302e) equipped with a 50 mm diameter cone-plate configuration was used for the rheological analysis on 10% GelMA solution in DIW. Flow rate tests were performed in order to investigate the viscosity variation at different temperatures (20, 25, 30, 37 °C), where 20 and 25 °C represent two operating temperatures close to estimated sol-gel range transition, 37 °C represents the body temperature, meanwhile 30 °C is in-between the previous operating values. The viscosity vs the shear rate data were considered to have a power law trend described by the Eq.3.3.

$$\eta = K \cdot \dot{\gamma}^n \tag{3.3}$$

Afterwards, the flow consistency index K (Pa $\cdot s^n$) and flow behavior index n (adimensional) have been calculated for each temperature to assess which particular non-Newtonian character is associated with GelMA solution.

Amplitude sweep tests were performed to find the linear viscoelastic region (LVR) at

different temperatures (20, 25, 30 and 37 °C). Before the test, each sample was cooled to the operating temperature for 10 min. A logarithmic ramp of shear strain was applied from 0.01% to 100% and keeping the frequency constant at 1 Hz.

Ramp decreasing temperature sweep tests were also carried out to evaluate the G' and G" behavior varying the temperature from 50 to 10 °C and keeping constant the shear strain at 10% and the fixed frequency at 1Hz. The cooling rate was at 1°C/min.

Finally, the viscosity has been evaluated varying the temperature in order to achieve the gelation temperature. The test was performed keeping costant the shear rate of 10 s^{-1} and decreasing the temperature from 45 °C to 15 °C with a cooling rate of 1 °C/min. Before the test, each sample was allowed to settle to the operating starting temperature for 10 min.

3.5. Injectability

Injectability tests on GelMA solution (10% w/v, described in section 3.2.3) were performed by using in-house developed set-up adapted to a MTS electro-mechanical machine (MTS, cat no. 1/MH with CTD-200, thermal chamber) with a thermostatically controlled chamber using a 5 kN load cell (Fig. 3.3).

Figure 3.3: MTS electro-mechanical machine with a thermostatically controlled chamber for the injectability.

The injection speed was set at 1.63 mm/s for a 5mL syringe, in order to have an output flow (0.2 mL/sec) (Q_{Out_Needle}) close to the clinical scenario [109] (assuming conservation of flow rate and applying a flow balance conservation) according to Eq. 3.4:

$$Q_{InSyr} = Q_{OutNeedle} = v_{PlungerSyr} \cdot A_{TrasversalSyr} = v_{OutNeedle} \cdot A_{TrasversalNeedle} \tag{3.4}$$

The test was carried out at four operating temperatures (20, 25, 30 and 37 °C). The sealed syringes were maintained for 30 min in a pre-heated water bath at the corresponding temperature. Different needle diameters were tested (18G, 20G, 22G), starting with the one with the largest diameter (18G, 0.838 mm), passing through the middle one (20G, 0.603 mm) and going towards the one with the smallest value (22G, 0.413 mm).

The crossbeam total displacement was set at 8.5 mm for each test, corresponding ejected volume of 1 mL. Nevertheless, whenever the force displacement real-time curve reached a critical value, the test was manually interrupted to avoid the collapse of the home made set-up. An upper limit of 10N was set as critical value to consider the solution comfortably injectable, according to [109] and BS EN ISO 7886–1:2018.

A theoretical calculation of the glide force was performed to try to predict the injection force, for temperatures where GelMA10% will show a fluid/liquid behaviour, using a model from *Andrea Allmendinger et Al.* [43] for non-Newtonian fluids. Glide force values were calculated at the different temperatures varying the needle size. The Hagen-Poiseuille law was adapted for the case of injection geometry under investigation, and non-newtonian fluid with the proper assumptions: a constant flow in addition to a negligible effects of entry losses and the conical symmetry of the syringe.

The force was calculated as reported in Eq.3.5. K and n parameters were obtained as explained in Paragraph 4.2. Further explanations of how to obtain Eq. 3.5 are reported in Appendix A.

$$F = 2^{n+2} \cdot \pi^{1-n} \cdot l \cdot R_{Syringe}^{2} \cdot K \cdot Q^{n} \cdot R_{needle}^{-(3n+1)} \cdot \left(\frac{3n+1}{2n+1}\right)^{n-1} + F_f \tag{3.5}$$

Where n (adimensional) is the flow behaviour index, l (m) is the length of the needle, $R_{syringe}$ (m) is the radius of the syringe, K ($Pa \cdot s^n$) is the consistency index, Q (m^3/s) is the volumetric flow, R_{needle} (m) is the radius of the needle and F_f (N) is frictional force between stopper and syringe barrel. The fixed values are reported in Tab.3.3 .

Table 3.3: Force glide parameters values needed for calculation

Parameter	Value	unit
K	- See Paragraph 4.2	Pa $\cdot s^n$
n	- See Paragraph 4.2	adimensional
l	- 38.4	mm
$R_{syringe}$	- 6.1250	mm
R_{needle}	- 18G, 20G, 22G	mm
Q	- 0.2	mL/sec
F_f	- See Paragraph 4.3	N

Empty syringes were used in order to calculate the frictional force at different temperatures varying the needle size (18,20,22G) [110]. The theoretical force value found with this model was used to evaluate whether the injectability behaviour of the GelMA solution can be previously predicted.

3.6. SEM investigation

A SEM investigation was performed on the two electrospun mesh types (aligned and random) to analyze the diameter size distribution and orientation of the fibers. For the qualitative analysis of DFs dispersion and length measurement (ImageJ Sorftware), 150 μL of the ultrasonication medium and of the washed cryomedium solution was dripped on a glass slide and observed at SEM. The diameter size of 30 fibers was manually measured and plotted in a histogram distribution. The fiber orientation was analyzed with an ImageJ DirectionalityJ plug-in (ImageJ Software).

The lyophilized hydrogels after the photo-crosslinking step obtained according to Paragraph.3.2.3 (GelMA10 and GelMA+DFs solutions) were cut to expose longitudinal cross-section and adhered to carbon tape, then sputtered with gold to study morphological properties. The samples were scanned and observed via SEM (Phenom XL, Thermo Fisher Scientific) and the final images were analyzed with ImageJ software to evaluate porosity, pore dimension and the integration of the fibers (n=3).

3.7. Mechanical compression tests

An Instron 5965 machine equipped with 1kN load-cell was used to carry out the mechanical tests. A compression deformation rate of 1 mm/min was applied. The photocrosslinked GelMA and GelMA+DFs samples (n=3) (obtained as described in Paragraph. 3.2.3) were immediately subjected to compression at RT (n=3). The height and the diameter of

each sample were accurately measured before to carry out each test and have been used to extrapolate the compressive modulus from the linear region of the curves, calculated as the slope of the curve in the range 0-10%, according to *Hairui Suo et Al.* [111]. Compressive toughness, maximal deformation and strength at break were also derived. Compressive toughness was calculated integrating the stress-strain graph area underlying the curve. Maximal compressive deformation and strength were taken as the corresponding maximal value obtained from the curve.

3.8. Physical characterization

3.8.1. Swelling behaviour

Crosslinked GelMA and GelMA+DFs samples (see Paragraph. 3.2.3) were put in a 24-multiwell with 2mL of DIW and placed in a 37 ° C water bath (n=5). At each time point a medium change was performed. The swelling behaviour was plotted over time up to 96 h (t=0.5, 1, 2, 4, 8, 12, 24, 48, 72, 96 h). At each time point the swelling ratio value was calculated as reported in Eq.3.6:

$$SR(t_i) = \frac{W_{wet}(t_i) - W_{post-crosslinking}(t_0)}{W_{post-crosslinking}(t_0)} \cdot 100 \tag{3.6}$$

$W_{wet}(t_i)$ is the weight of the hydrogel at each time point, while $W_{post-crosslinking}(t_0)$ is the wet weight immediately after the UV-crosslinking.

3.8.2. Sol-fraction analysis

A sol-fraction quantification was performed at a *equilibrium* time point in the *plateau* region of the swelling curve. The *equilibrium* time point was selected when the swelling trend becomes asymptotic, and the time point at which the corresponding value have a comparable value with the following one (small % variation).

At the corresponding time point the samples (n=3) were freeze-dried (FreeZone 2.5 Plus, Labconco) for 24h and the cross-linking efficiency was analyzed through the Eq.3.7:

$$GelFraction(t_i) = \frac{W_{dry1}(t_0) - W_{dry2}(t_i)}{W_{dry1}(t_0)} \cdot 100 \tag{3.7}$$

4 | Results and Discussion

4.1. Chemical characterization

4.1.1. FTIR

A FTIR spectra for gelatin, GelMA and electrospun PCL, PCL75:GelMA25 meshes are reported respectively in Fig.4.1a and Fig4.1b.

GelMA specific vibrations can be detected in the spectrum at 1252 cm $^{-1}$, 1558 cm $^{-1}$, 1656 cm $^{-1}$, 3058 cm $^{-1}$ and 3420 cm $^{-1}$ (from 1 to 5) (Fig.4.1a). Peaks at 1252 cm $^{-1}$ and at 1558 $^{-1}$ are related to vibration of N-H bond and Amide II signal respectively. Peak signal of 1656 cm $^{-1}$ is linked to the amide III (C=O) and is related to gelatin second structure. In particular it has been reported that both intensity and position were function of the second structure type [112]. From the spectrum is not possible to identify a precise distinct new peak characteristic of methacrylation respect to Gel one. This happens because the presence of methacrylate vinyl group can be traceable by C=C stretching absorption peak at 1630–1680 cm^{-1}, that is however concealed by the strong amide (C=O) signal characteristic of gelatin-based material at 1656 cm^{-1}. The peaks at 3058 and 3420 cm $^{-1}$ were related to B and A amides, respectively and respresent the C-H bonds variations and the mobility of the N-H bonds. These results confirmed that the GelMA has been synthesized successfully according to *Sahar Abdollahi Baghban et Al* [113].

For the spectrum of electrospun PCL75:GelMA25 mesh, it is possible to identify a variation of the spectrum, in terms of intensity and position of the peaks (from 1 to 6) at 1200 cm^{-1}, 1550 cm^{-1}, 1625 cm^{-1} and in the 2850-2950 cm^{-1} and 3250-3350 cm^{-1} ranges (Fig.4.1b). New peaks at 1550 and 1625 cm^{-1} respect to to the PCL spectrum. Both methacrylate vinyl group and Amide II groups may be attributed to that signal [114]. The peaks of the PCL75:GelMA25 blend have lower intensity when compared to the characteristich peaks of GelMA alone at 1252 and 1656 cm^{-1}. The presence of PCL also affects the signal in the 3250-3350 cm^{-1} range causing a narrow signal compared to

GelMA spectrum. At the same time, the GelMA affects the characteristic signals of the PCL at 1700-1750 cm^{-1} range related to the strong bands such as the carbonyl stretching, at around 2850-2950 cm^{-1} range relative to symmetric and asymmetric CH_2 stretching, at 1200 cm^{-1} relative to the OC=O stretching, making them marked. From the analized spectra, according to *P.Coimbra et Al.* [114], the presence of both PCL and GelMA in the electrospun blend mesh is confirmed.

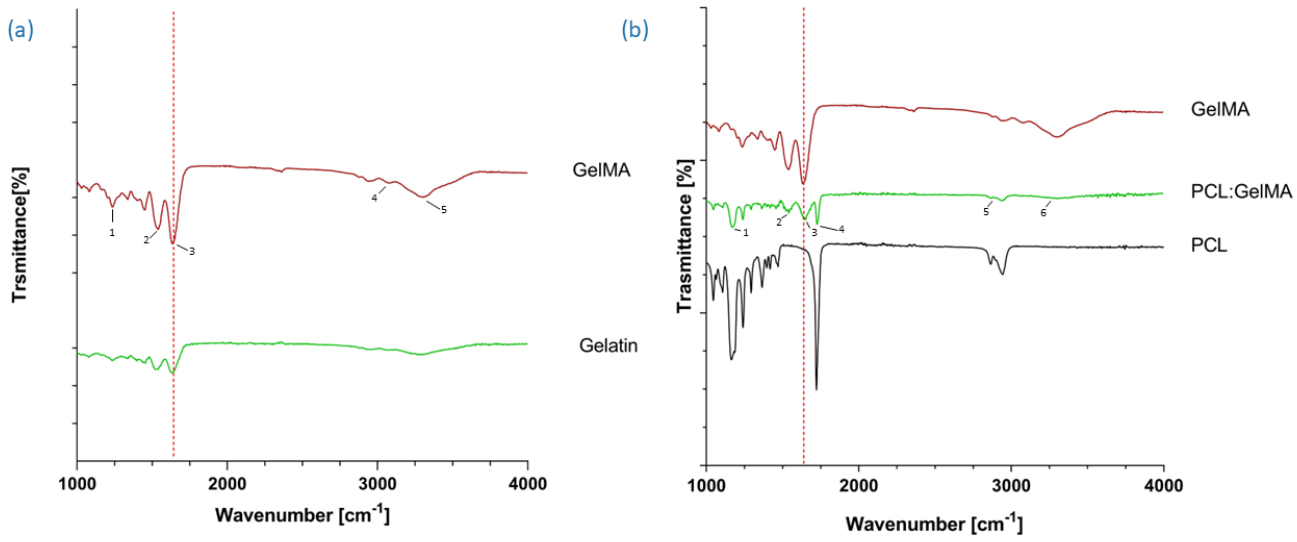

Figure 4.1: (a) FTIR spectrum of gelatin (green) and GelMA (red). The dashed red line shows the overlapping of the methacrylate vinyl and the Amide I signals. (b) FTIR spectrum of electrospun mesh of the PCL (green) and the PCL75:GelMA25 blend. The dashed red line shows the characteristic peak for the blend configuration at 1630-1680 cm $^{-1}$.

4.1.2. Ninhydrin assay

To understand the effect of pH during the functionalization of the gelatin, the DoF of GelMA was measured by using Ninhydrin assay and the results are shown in Fig.4.1a). The comparison between the two different baths (PBS and DIW) showed that a higher substitution degree occurred in the reaction at higher pH (using PBS respect to DIW), as confirmed by *Shirahama at Al.* [115]. In particular, with DIW bath DoF was 66% meanwhile the DoF with PBS functionalization bath was 75%. Since the target DoF was 80%, a PBS-based functionalization GelMA protocol was used for the material preparation for the subsequent tests.

The mentioned method for the extrapolation of the functionalization degree could be interpreted trough Fig.4.2a. To understand the effect of pH during the functionalization reaction with MAA a comparison between two different reaction baths was performed and shows that increasing the pH using PBS respect DIW cause a high substitution degree, according with as reported by *Shirahama at Al.* [115]. The calculated DoF with DIW functionalization bath produce a DoF equal to 66% meanwhile the basic PBS functionalization bath produce an higher value of 75%. Since the desired DoF target outcome was 80%, a PBS-functionalised GelMA was used for the subsequent tests.

4.1.3. ^{1}H-NMR

The ^{1}H-NMR spectra shows the differences in terms of peaks between gelatin and the GelMA. As reported in the Fig.4.2b, proton peaks belonging to functional signal groups of GelMA differed respect to the gelatin ones marked as orange “a” “c” and "d" . According to *Zhu et Al.* [116], new peak appear in the range of 1.85-2 ppm (a) increased widely and is related to methylene protons of non-modified lysine. The peak related to the free lysine signal of the unmodified gelatin at 2.8-2.95 ppm (b) decreased distinctly and due to methyl protons of methacryloyl groups respectively. Additionally in the range of 5.4–5.7 ppm (c-d) new peaks appear and are owed to acrylic protons of methacrylamide groups in lysine residues and acrylic protons of methacrylamide groups in hydroxylysine residues respectively. The corresponded DoF was equal to 80%, according to Eq.3.2.

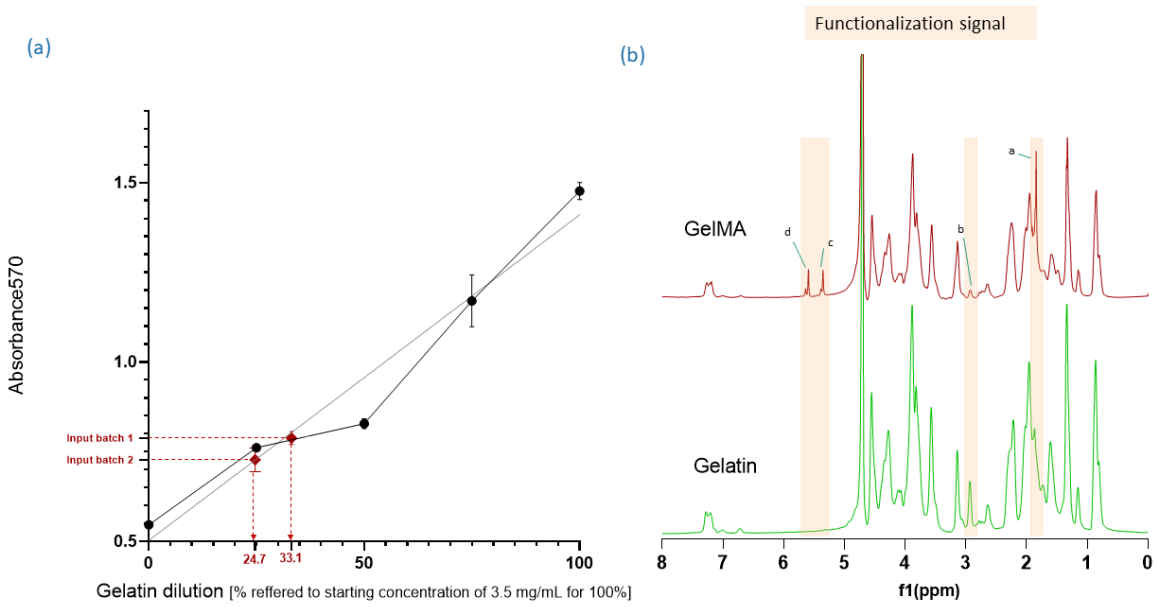

Figure 4.2: (a) A standard curve in obtained trough a linear regression of the absorbance measured values. From a known absorbance value, it is possible to derive the corresponding X% value. Dependence on the pH of the functionalization bath during methacrylationreaction on the degree of functionalization. Higher DoF in basic bath (PBS) than DIW.(b) ^{1}H-NMR signal of gelatin and GelMA. The orange bands underline the functionalization group signal.

4.2. Rheological analysis

From the analysis of viscosity as a function of shear rate at different temperatures (Fig.4.3a) is possible to classify the curves into two macro-groups with similar trends. For the curves at 37 and 30 ° C, viscosity values are in the same order of magnitude over the shear strain, with a slightly change in the slope of the curve around the value of 10 s^{-1} shear rate. For the curves at 25 and 20 ° C, on the other hand, the values at the same shear rate differ by orders of magnitude (factor 1000 for shear rates of $0.1s^{-1}$ and factor $\approx$ 100 for values of $\approx$ 1000 s^{-1}). However, the curves turn out to have a similar characteristic trend and do not show a shear rate value at which the corresponding viscosity value collapses as in the case of 20 and 25 ° C. This suggests that the curves at higher temperatures (30 and 37 ° C) have a a sudden decreasing behaviour and the viscosity value settles in the 0.01-0.001 Pa·s range, for shear rates greater than 10 s^{-1}. This value represents a threshold beyond which the viscosity is no longer changing, for 30 and 37 ° C, suggesting an independent behaviour (remains costant) of viscosity over the shear rate applied. In the following Paragraph (Paragraph 4.3), it will be seen how a plateau region will be reached for 30 and 37 ° C, suggesting that low viscosities allow lower forces during injec-

tion. From the flow curves, the K and n parameters were derived, highlighting the shear thinning character of the GelMA solution.

Table 4.1: K and n indexes obtained from linear regression parameters of flow curves as slope and intercept (n=3)

Temperature	**Consistency index K [Pa · s $^{-1}$]**	**Flow index n [adimensional]**
20 °C	242.1 ± 17.20	0.12 ± 0.152
25 °C	1.35 ± 0.014	0.50 ± 0.006
30 °C	0.03 ± 0.041	0.59 ± 0.028
37 °C	0.035 ± 0.0066	0.47 ± 0.049

N and K are extrapolated from the linear regression as slope and intercept, n index represents the type of behaviour in the flow regime and, for n<1, the smaller n is, the more the character of the material will be shear thinning. Meanwhile, the K index gives the magnitude of the fluid consistency and can be considered as a viscosity value in the case of Newtonian fluids [117]. Consequently, with a fixed n value, the greater the value of K, the more viscous behaviour will be attributed to the material at a given shear rate. The K and n values shown in Tab.4.1 describe the rheological behaviour of GelMA solution at different temperatures. The consistency index assumes much larger values at 20 °C, with a value of 242.1 ± 17.20 Pa · s $^{-1}$, than at other temperatures, reaching a value of 1.35 ± 0.014 Pa · s $^{-1}$ at 25 °C, 0.03 ± 0.041 Pa · s $^{-1}$ and 0.035 ± 0.007 Pa · s $^{-1}$ for 30 °C and 37 °C, respectively. The flow behaviour index for increasing temperatures show values of 0.12 ± 0.152, 0.5 ± 0.006, 0.59 ± 0.028 and 0.47 ± 0.049 for 20, 25, 30 and 37 °C respectively. The flow index n similarly increases as a function of temperature with a value clearly smaller than the others for 20 °C. In contrast, the values of n for 30 and 37 °C are comparable. The n values show the maximal value for 30 °C. It can be observed therefore that K and n values are more sensitive to variations in temperatures in the range 20-25 °C than for the range 30-37 °C, accordingly to the gel-point temperature value. K and n parameters were used in the injection model to calculate the theoretical glide force in function of temperature (indirect function).

From the amplitude sweep analyses (Fig.4.3b) performed at different temperatures, it is possible to observe a decrease of G' and G" as the temperature increases. At 20 °C, the values of G' and G" (in blue) have a constant trend as the shear strain increases, with G' that clearly prevails over G", indicative of a solid-like behaviour. At 25 °C, it is possible to observe a decrease of G' and G" (in green) compared to the corresponding values at 20 °C, with G' still prevailing over G" confirming a solid-like behaviour. G' increases slightly with increasing shear strain from 1 Pa for 0.1 % to 10 Pa for values around 100

% shear strain. On the other hand, G" remains constant over a shear strain variation. When 30 and 37 °C are tested, the G' and G" lie within a very narrow range and are found to have almost equal values. At higher temperatures, as the shear strain increases, G" prevails over G' confirming a liquid-like behaviour at 30 and 37 °C. However, at these temperatures, the trends of G' and G" for low shear strain (less than about 1) values fluctuate, much more than for the same shear strain values at temperatures of 20 and 25 °C, causing a variable trend of the curves. This phenomenon can be attributed to the liquid-like state of the material at that temperature suggesting that, at 30 and 37 °C and low shear strain value, a different geometry should be used for rheological measurements (e.g., concentric cylinder measuring systems). On the other hand, this would no longer work well for temperatures near the sol-gel transition, nor for high shear strain % values being a suitable geometry for very watery material. The field of application also requires the material to be subjected to very high strain % during injection, so it is reasonable to lose accuracy for low shear strain % values rather than use other geometries and lose accuracy for higher values. The GelMA solution has therefore a liquid-like behaviour which influence the force transmission and the relative force reading. Therefore, for low shear strain % the material, starting from a static configuration, is in a transient state in which the measurement produce variables values. As the shear strain increase, such outliers cease to occur. The measurement could lead to results with fewer outliers if a pre-shear strain of 0.1 % was applied for a predetermined time to ensure that the material begins to flow without undergoing an abrupt transient from the static condition.

From the graph it is possible to identify a linear viscoelastic region (LVR) which is common to all curves regardless of temperature. It is possible to use a shear strain % value of 10% for the following rheological analysis.

An oscillating logarithmic temperature ramp (Fig.4.3c), carried out at 10% shear strain, shows that the gel-point occurs at 20 °C. This suggests that the gelation temperature of GelMA resides in this vicinity, according to *Zhou et Al.* [118]. To investigate deeper this aspect, an evaluation of the viscosity as a function of temperature at a fixed shear rate of $10s^{-1}$ was performed. The shear rate of 10 s^{-1} was fixed at this value as the viscosity of the GelMA solution is almost constant in the range 0-10 s^{-1} at 25°C [119]. However, outliers in the curves were obtained for lower shear rates (0.1-1 s^{-1}). For temperatures close to 20 °C indeed the material, by gelling, increases its adhesiveness to the superior rotating plate, creating sticking points. This is not evident at shear rates of 10 s^{-1}.

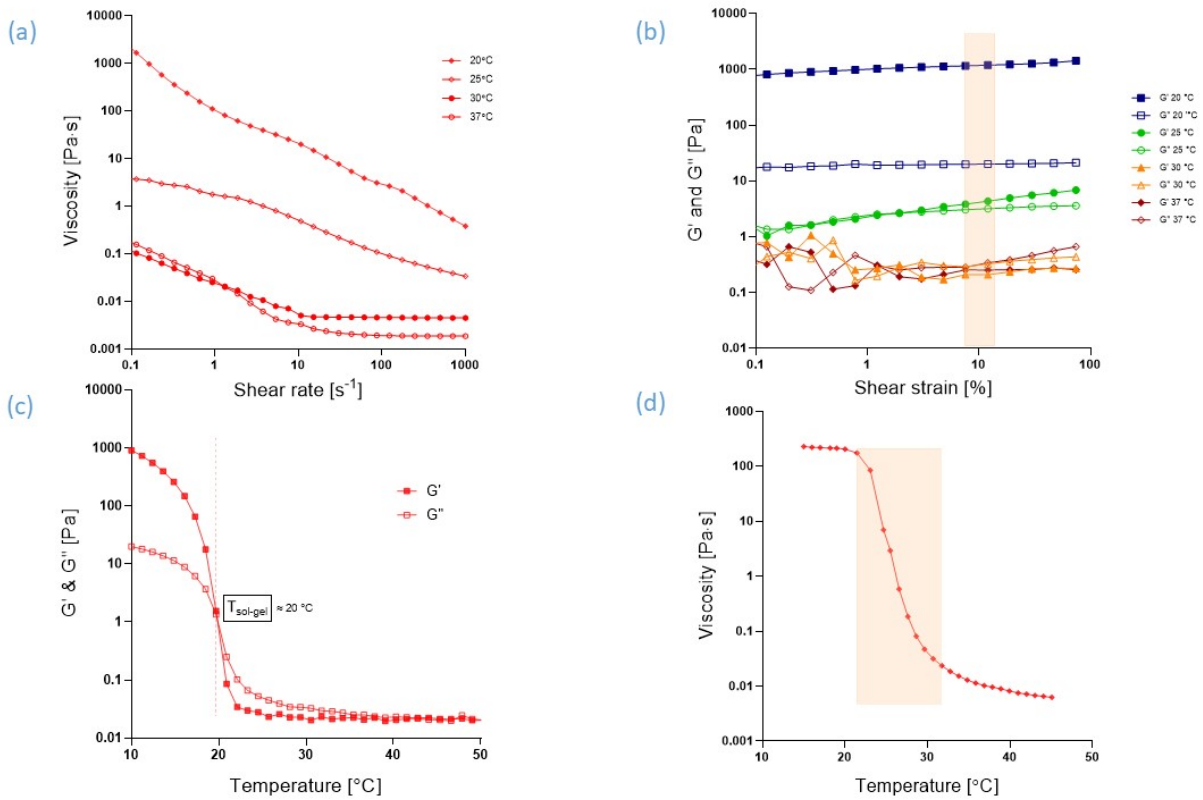

Figure 4.3: Analysis performed on GelMA10% (a) Flow regime test: viscosity over shear rate at different operating temperatures to extrapolate the parameters n and K. (b) Amplitude sweep at different operating temperature to evaluate the LVR. (c) Temperature oscillation ramp allow to observe a collapse of G' and a cross with G" in correspondence of the range 20-25 °C. (d) Viscosity over temperature collapse 20-25 °C, additional confirmation about the gelation temperature.

Results show a collapse of viscosity from 20 °C up to an asymptotic settlement from 30 °C onwards (Fig.4.3d). This evaluation supports the amplitude sweep results, in which the relative G' and G" do not differ substantially between tests carried out at 30 and 37 °C.

All the reported values are in line with those presented by *Yin et Al.* [107] where a rheological characterization on GelMA-base bioink was performed, showing gelation temperature range comparable with the ones obtained in the present thesis work, in addition to values of the same orders of magnitude and comparable curve profiles.

The tests performed are the ones suitable for a preliminar evaluation of possible injectability of a material. In this particular case, GelMA represent a material with an upper critical solution temperature (UCST), means go towards a sol-gel transition lowering the temperature. For this reason all the tests were carried out with the prerogative of being performed at different temperatures to understand the rheological behaviour of

the GelMA10% solution, in order to determine a priori a possible temperature range for material injection.

4.3. Injectability

Injectability tests showed the expected temperature-dependent behaviour. In particular, the injection force decreases with increasing temperature. At 20 °C using an 18G needle, the test was manually interrupted as the force profile increased rapidly, risking breaking the injection set-up. A characteristic force profile at 20 °C with 18G is shown in Fig.4.4a. As the 18G could not allow the extrusion reaching a plateau-like region, the subsequent needles (20G and 22G) were not tested at 20 °C. A maximal force value of ≈ 80N (Fig.4.4a) was measured for a granular GelMA with a gellous feature that is highly adhesive to the needle. At 25 °C, a pseudo-plateau region can be observed for 18G and 20G with a slight increasing character of the curves (Fig.4.4b). By carrying out a linear regression of the pseudo-plateau section, it was possible to calculate the slope m for both 18G and 20G curves (m_{18G}= 1.77 and m_{20G}= 2.2) showing a steeper slope for the 20G configuration (FIg. 4.4b'). The fact that the force at 25 °C does not reach a plateau can be partially explained by the rheological amplitude sweep at the same temperature. Indeed, as soon as the material tries to be extruded it is subjected to a strain % such that the values of G' and G" (see Paragraph 4.2, amplitude sweep test) are similar and approximately equal to 1 Pa. As the material continues to be extruded, a higher strain % is applied to the material, which, as evidenced by the trend of G', shows a greater solid-like character. In particular, G' at 25 °C increases as the applied strain % increases. From this correlation injection force-amplitude sweep test can be explained the slightly increasing trend in the pseudo-plateau region of the injection force curve. For the configuration with 22G, on the other hand, a hiccup pattern can be observed with an initial momentary entry into a constant-force region before entering in a new plateau region with a constant force value of ≈ 80N Fig.4.4b. The tests carried out at 30 and 37 °C (Figs. 4.4c and 4.4d) and show similar curves. At 30 °C, maximum force values of less than 10N are observed for both 18G and 20G. For the 22G, on the other hand, values of around 25N are reached, but the trend of the curves for 18G and 20G is similar. At 37 °C for both 18G and 20G, the maximum plateau force values are equal to ≈ 2.5 and ≈ 3.5N respectively and are similar to the ones reported by *Kulkarni et Al.* at the same temperature [120]. Furthermore, when compared to the corresponding values at 30 °C, they show lower values. For 22G, a maximum value that slightly exceeds 10N is observable. Figs 4.4b', 4.4c', and 4.4d' were rescaled (on the right) in order to better appreciate the trends of the curves.

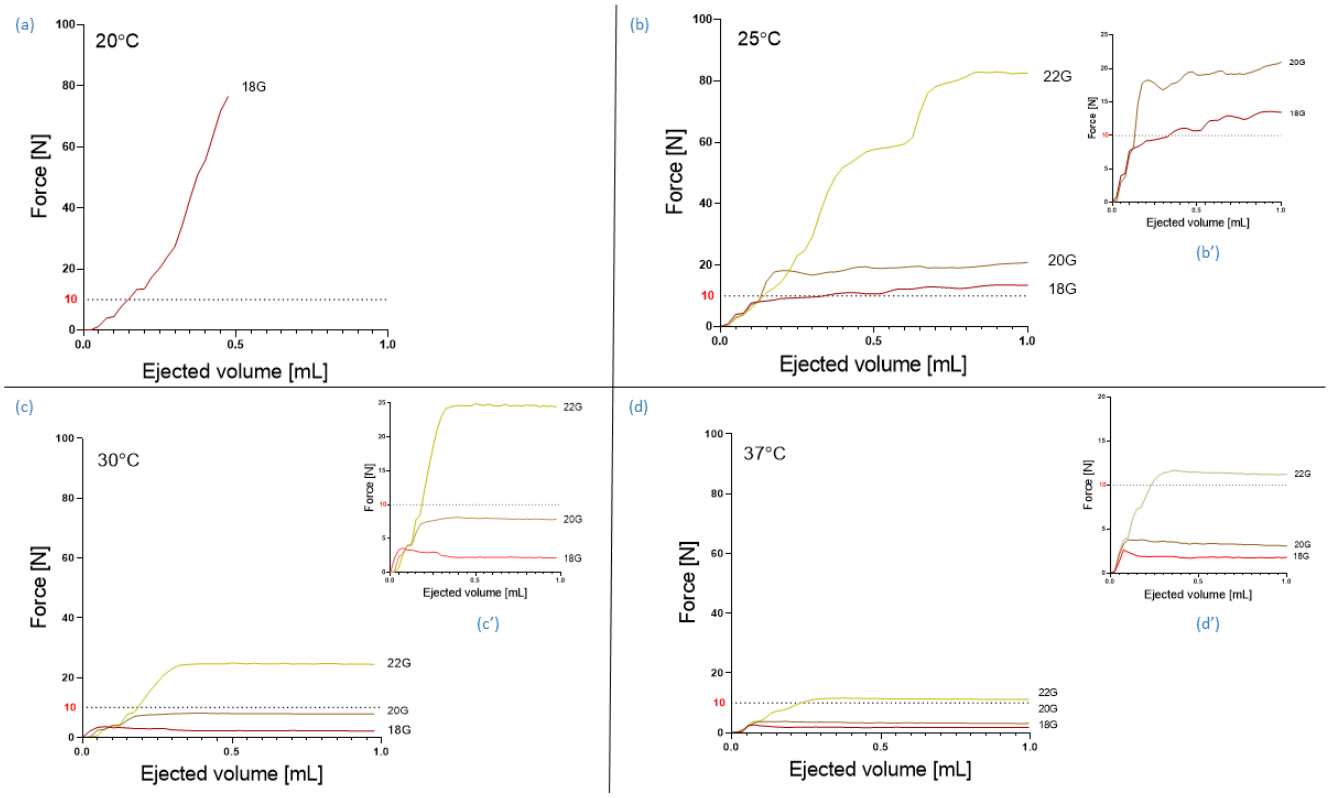

Figure 4.4: (a) Force over extruded volume at 20° C. (b) Glide force over extruded volume at 25° C. (b') Glide force over extruded volume at 25° C for 18G and 20G rescaled curves. (c) Glide force over extruded volume at 30° C. (c') Glide force over extruded volume at 30° C for 18G and 20G rescaled curves. (d) Glide force over extruded volume at 37° C. (d') Glide force over extruded volume at 37° C for 18G and 20G rescaled curves.

.

Since the sol-gel temperature of the 10% GelMA solution is in the range of 20-25 °C, it is complicated to inject at 20 and 25 °C as evidenced by the maximum values in the graphs (Figs4.4a) and b)). This is associated with the phase change of the solution, which tends to become a gel with solid-like behaviour. Around the sol-gel point, therefore some portions of the material begin to gel, leading to the formation of clots that hinder extrusion, and which need a greater value of force to be injected. This can also be observed from the more inhomogeneous trend of the curves at those temperatures, having an increasing smooth trend for 25 °C for 18 and 20G, more noticeable swings in force for 22G and an increasing course with a greater slope for 20 °C and 18G.

For this reason, as the model for glide force prediction is applicable to non-Newtonian fluids/liquids, the 20 and 25 ° C configurations were not considered, as the material is in a gel-like state. For the temperatures of 30 and 37 ° C, on the other hand, a comparison

between the experimentally measured force and the calculated one, showed that the model is more accurate in prediction the real behaviour for the 18G condition than for the 20G and 22G conditions and for 30 ° C rather than 37 ° C (Fig.4.5), but not yet precise enough to be considered reliable.

In Fig.4.5 it can be observed that as the needle size decreases (from 18G to 22G), the model decrease the accuracy. A greater difference between calculated and measured force occurs at temperature of 30 rather than at 37 °C. The two phenomena can be justified in this order: the assumption that the change in cross-sectional area between syringe and needle can be considered negligible probably falls away, and this is more noticeable for a material which passes through shrinkage, that posses a solid-like (at 30 °C) rather than a liquid-like (at 37°C). However, rheological analyses show no marked difference in G' and G" values at 30 and 37 °C. Additionally, the estimation of frictional force trough empty syringes could be valid considering GelMA not impacting into the friction it makes with the plunger surface. GelMA probably creates a relevant friction component with the walls, that cannot be approximated by the friction force between the plunger and walls with the empty conditions assumed. Nevertheless, the mean frictional force calculated for empty syringe for 18G, 20G, 22G at 30 and 37 °C are reported in Tab. 4.2.
It can be seen that as the cross-sectional area of the needle decreases, the maximum ejection force also increases for the empty configuration. From this it follows that as the needle cross-section decreases, atmospheric pressure will exert an ever-increasing force on the needle cross-section which will oppose extrusion. A further piece of information can also be derived for the configuration with air, namely that considering the cross-sectional variation to be irrelevant is limiting. Anyhow, these discrepancies will deserve to be evaluated in greater detail in future efforts, to check the opportunity to develop a new model, better fitting with the GelMA and GelMA+DFs behaviors. I.e., a valid option could be to carry out CFD simulations in which both rheological parameters obtained at different temperatures and the gyometries involved, in addition to constrain such as inlet or outlet velocities, are provided as inputs to fit better the injectable behaviour.

Table 4.2: The frictional force measured for empty syringe configuration (n=3).

Temperature	**18G**	**20G**	**22G**
30 °C	2.2 ± 0.8 N	3.68 ± 0.32 N	6.5 ± 1.2N
37 °C	2.15 ± 0.45 N	3.74 ± 0.16 N	7.1 ± 0.89 N

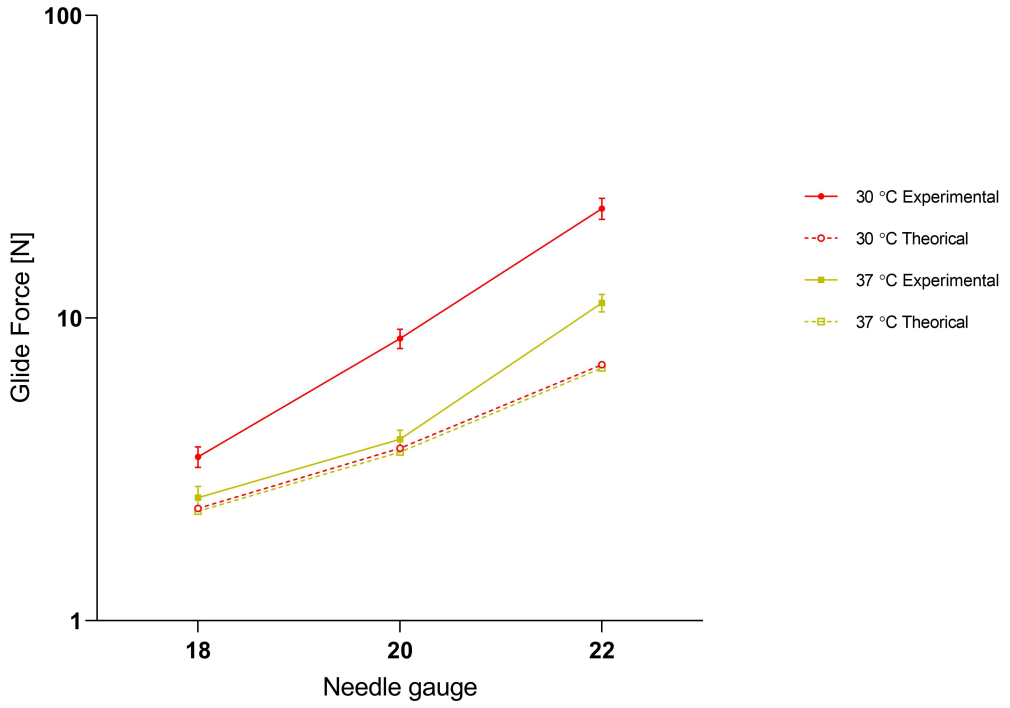

Figure 4.5: Comparison between measured maximal glide force (red continuous) and calculated glide force (red dashed) at 30 °C and maximal glide force (yellow continuous) and calculated glide force (yellow dashed) at 37 °C, as function of needle size.

The results obtained for the configurations at different temperatures therefore suggest that 30 °C can be set as the upper limit of injection temperatures in order to have homogeneous injection (reaching a well-defined plateau zone) and within a force range applicable by users comfortably (F<10N).

4.4. Mesh, DFs and bulk hydrogels SEM evaluation

In Fig.4.6a and 4.6b beads were obsarvable for both PCL and PCL75:GelMA25 solutions using a 10 % w/v polymer concentration. Increasing the polymer concentration to 20 % w/v beads disappear (Figs. 4.7a and 4.8a), according to a previous study [121].

The PCL75:GelMA25 random electrospun mesh (Fig.4.7a and 4.7b) shows randomly orientation, bead-free and homogeneously distributed fibers, as also shown by the directionality histogram (Fig.4.7c). The histogram is very broad and flat, characteristic of a high variability of the analysed values, as expected for a random distribution of the electrospun fibers. This type of mesh, obtained with the parameters reported in Paragraph 5.3, consists of fibers with a diameter value of 835.2 ± 150.2 nm with a maximum relative frequency of 24% for fibers in 750-950 nm range (Figs.4.9a and 4.9b).

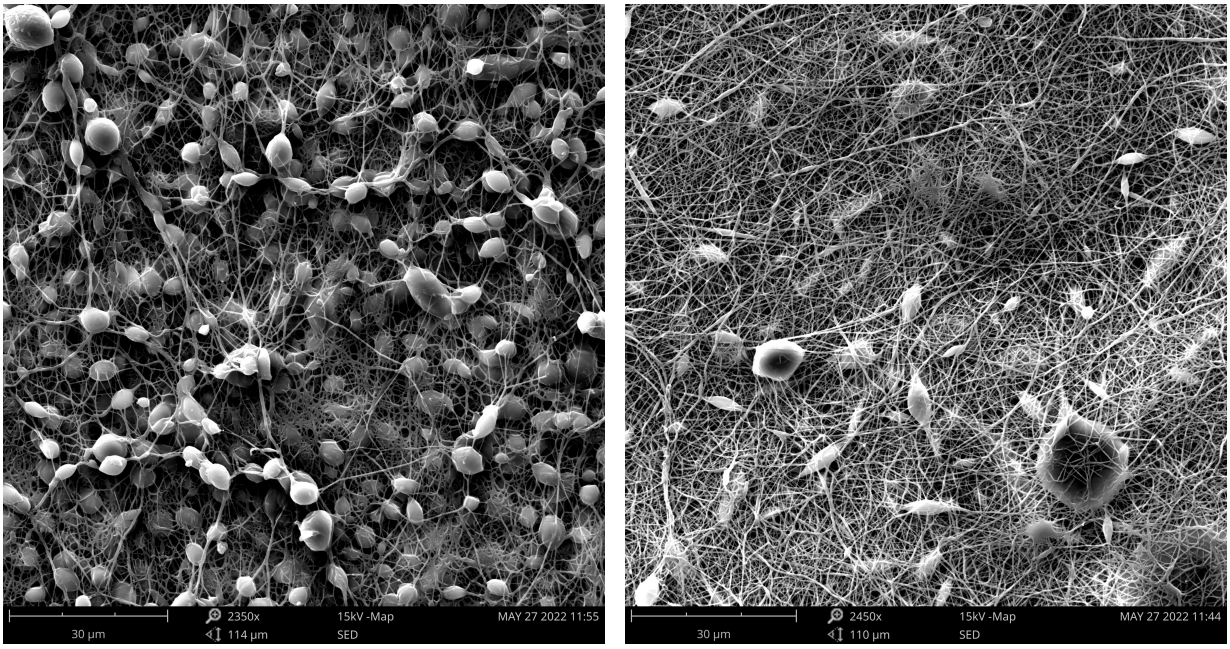

(a) (b)

Figure 4.6: 2400x Magnification: (a) Electrospun PCL mesh at 10 % w/v. (b) Electrospun PCL75:GelMA25 mesh at 10 % w/v. Beads can be observed in both meshes with a decreased presence for PCL75:GelMA25 mesh.

.

The PCL75:GelMA25 electrospun mesh consisting of aligned fibers (Fig.4.8), similarly shows free-bead and visibly homogeneous fibers. The histogram shows a narrow, sharp profile at about 90 °C, indicating a very good alignment of the electrospun fibers. The aligned fibers have a diameter of 724.9 nm ± 159.4 with a maximum relative frequency of 32% for fibers in the 650-750 nm range (Figs.4.9a and 4.9b). During the electrospinning phase due to the rotation of the collector, the viscous solution is subjected to such a tensile stress that the resulting fibers produced are stretched more than for the random configuration, causing smaller diameter values for the aligned fibers. Due to this stretching process, it was assumed that a higher degree of crystallinity could be achieved, which combined with the higher degree of anisotropy could favour mesh dispersion through an ultrasonication process.

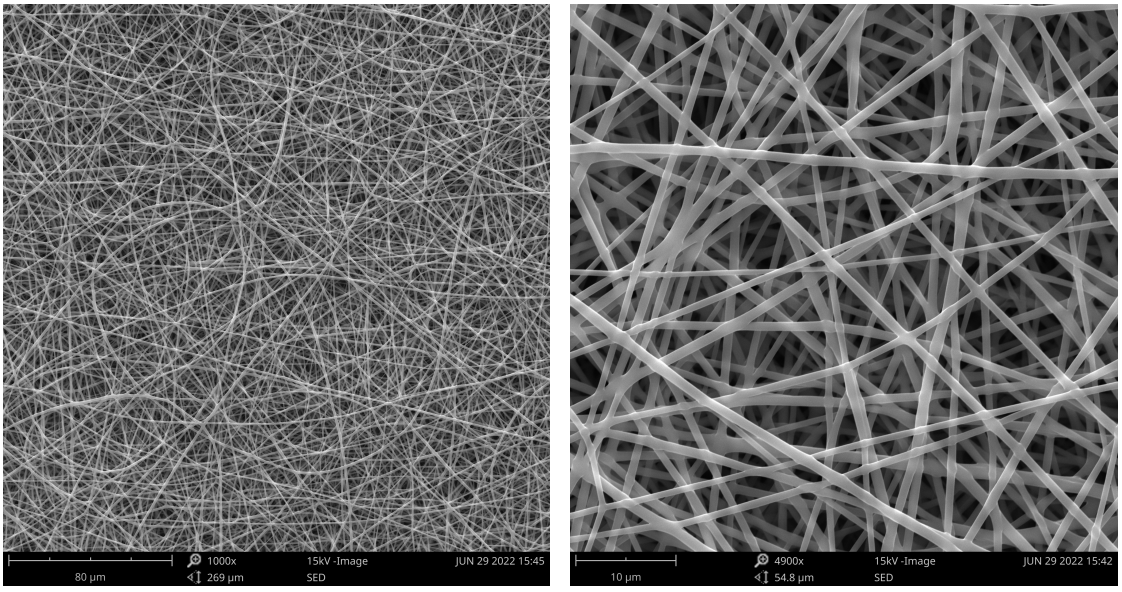

(a) (b)

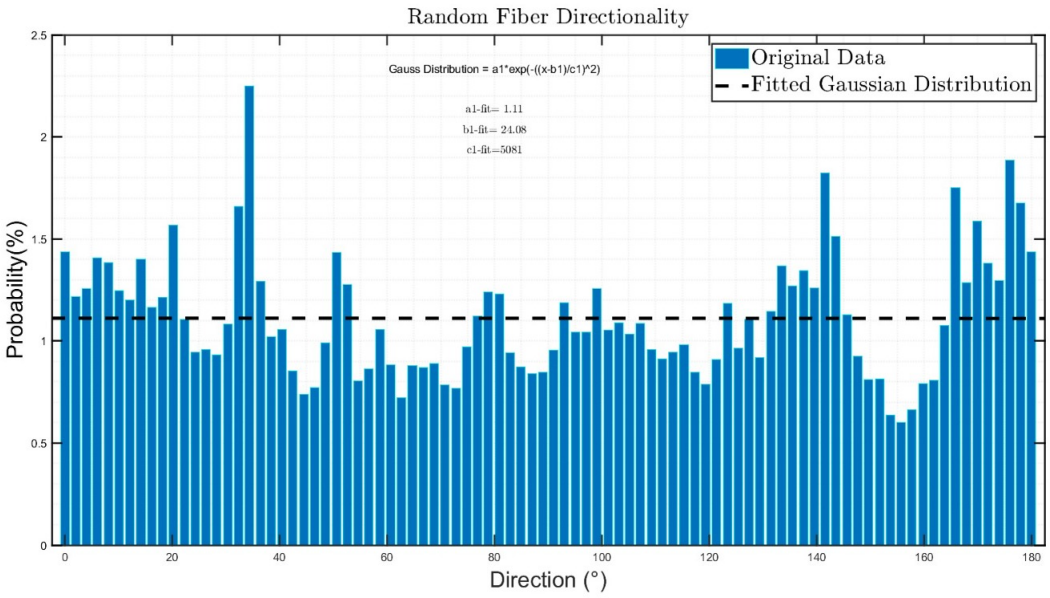

(c)

Figure 4.7: Random isotropic fibers: (a) 1000x, scale bar= 80 µm. (b) 4900x magnitude, scale bar= 10 µm (c) Directionality histogram of random fibers mesh, flat profile.

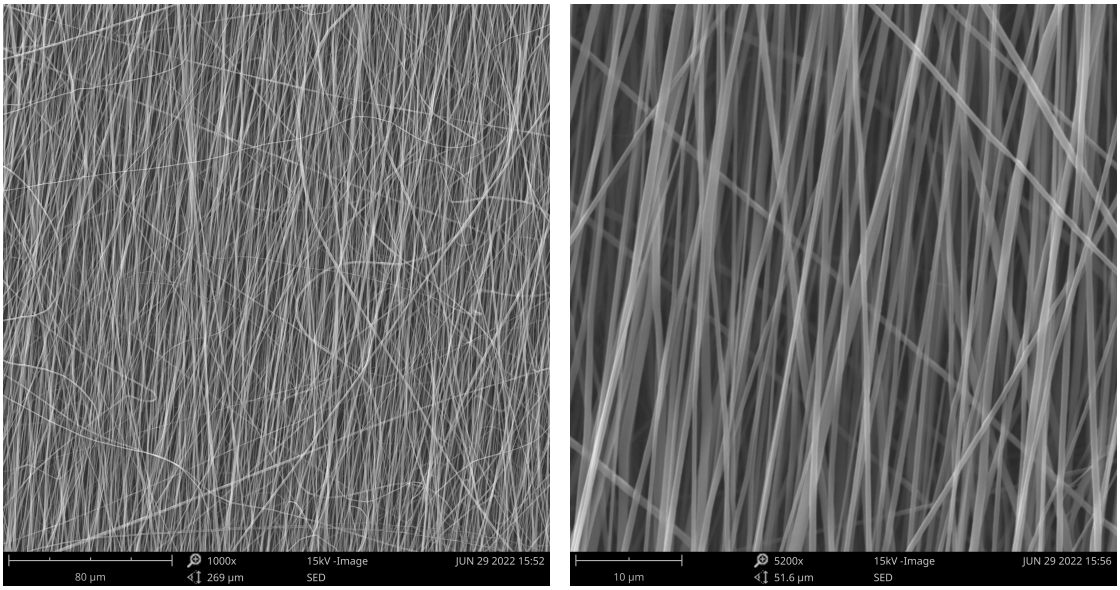

(a) (b)

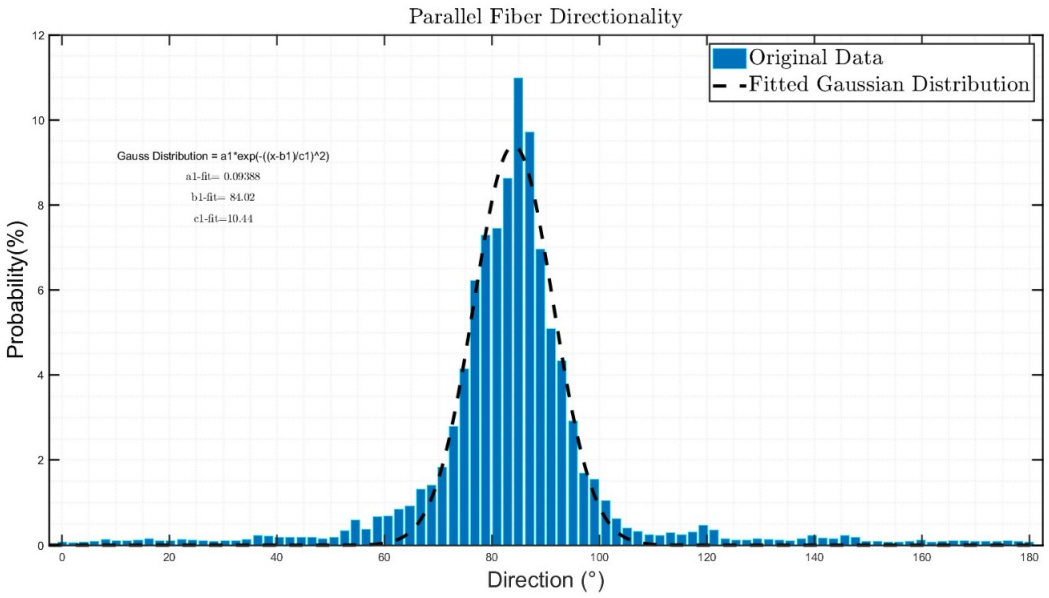

(c)

Figure 4.8: Aligned anisotropic fibers: (a) 1000x, scale bar= 80 µm (b) 5200x, scale bar= 10 µm . (c) Directionality histogram of aligned fibers mesh, high probability for 90 °.

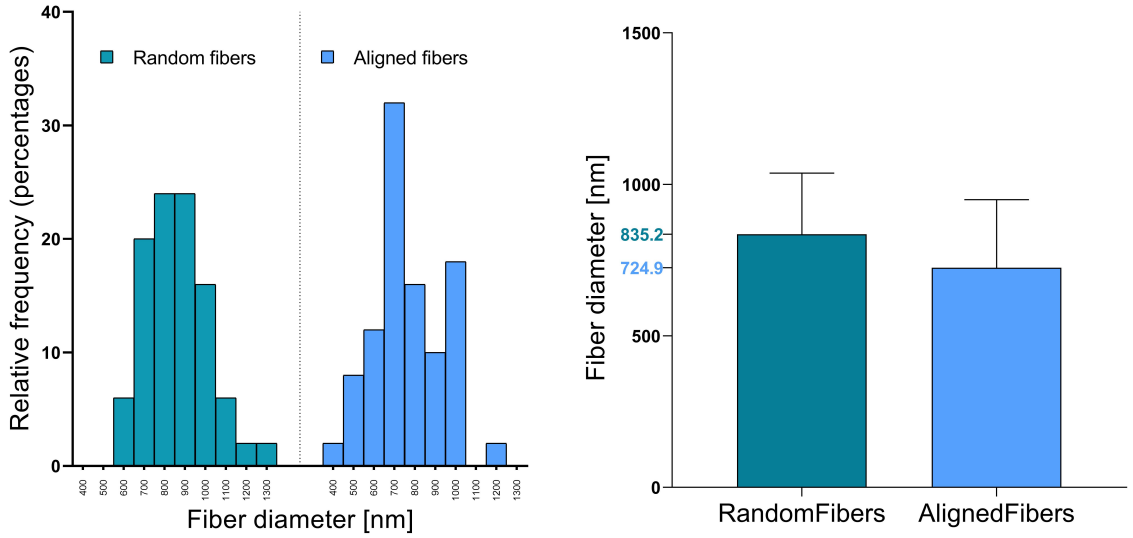

(a) (b)

Figure 4.9: (a) Diameter fibers distribution of random fibers (left histogram) and aligned fibers (right histogram). (b) Diameter mean value of random fibers (left box) and aligned fibers (right box).

For random mesh (isotropic fibers) the ultrasonication did not produce any fiber-like dispersion. Unfortunately, a not well dispersion and a failing outcomes happens also for aligned mesh. The ultrasonication parameters were changed, resulting in two different configurations (see Paragraph 3.2.2). It was hypotized that in neither of them, a condition whereby the suitable energy needed for fragmentation was satisfied. Therefore the process is unable to provide sufficient energy to detach the fibres from their degree of adhesion. No optimal dispersion was therefore obtained by changing both tip type, sonication temperature (as close to zero as possible) and sonication time. Only some isolated dazzling clusters of fibers were obtained for the aligned fiber mesh, as can be observed from the Figs.4.10a and 4.10b.

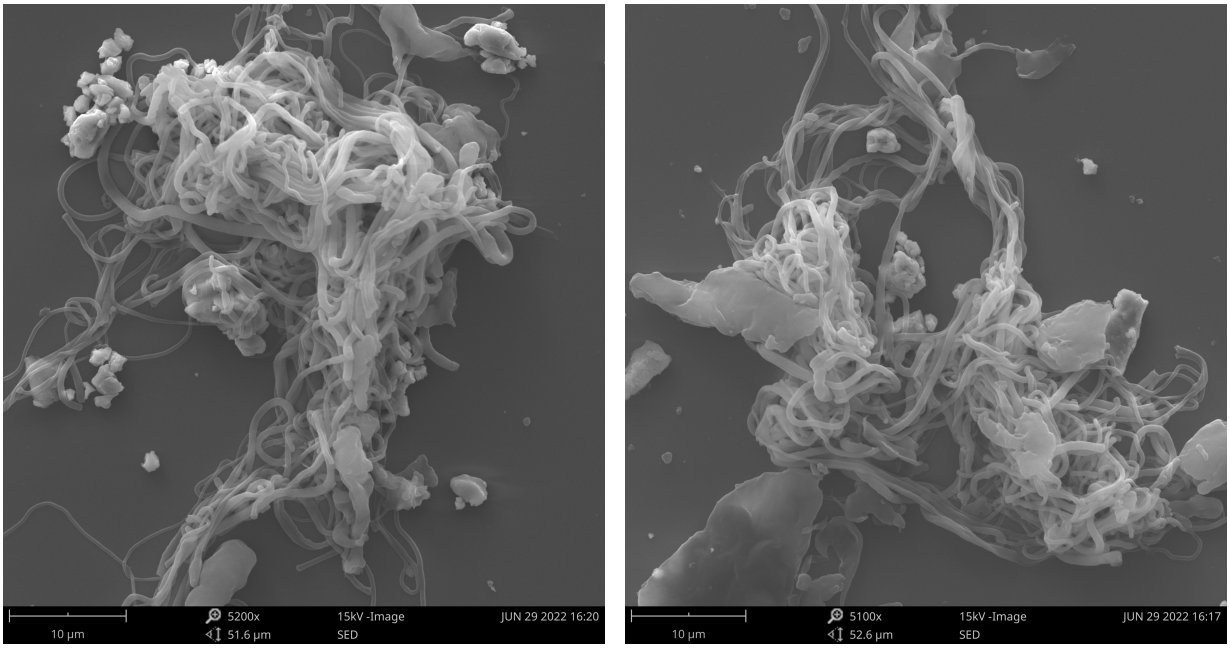

(a) (b)

Figure 4.10: Results of ultrasonication on aligned fiber meshes. Notable pseudospheric shaped particle, 5000x and scale bar= 10 µm. (a) Aggregate of fibers for configuration1. (b) Aggregate of fibers for configuration2.

The ultrasonication process may have led to the undesirable fiber agglomerations, which is likely to be associated with the nature of PCL. PCL has a transition glass temperature around -60 ° C and at the implemented ultrasonication temperatures, it has a very deformable rather than brittle character. Consequently, the process failed to cause a punctual brittle fracture on several fibers of the mesh at the same time. More likely ductile fractures occurred in which the material deformed long before breaking. Confirming this in Fig. 4.10 some pseudospheric elements could be composed of material broken up from the mesh and deformed as a result of the process. To support this, an SEM-EDS investigation on these pseudospheric elements, could reveal the chemical nature of the particles, excluding the possibility to be salt (inorganic nature) or dust, confirming or not the hypothesis just presented. Indeed, it is assumed that the mesh subjected to ultrasonication initially starts to deform plastically and then begins to lose fibers or clusters of fibers. As the process progresses, the ultrasonication deform these fiber clusters until they lose their morphology, continuing to deform and break in a ductile way. In order to understand this effect of ultrasonication on fragmentation, experiments in which sampling will be done at different time points to evaluate them by SEM, will be carried out. Indeed, for isotropic mesh (aligned fibers) the process produced entangled clusters of non-dispersed fibers with such a morphology that no meaningful length measurement was possible.

Following this failed post-processing process, the fibers were treated with the cryostat trough micro-cutting technique, which produced morphologically assessable dispersed fibers with microstructured fiber morphology (Figs. 4.11a and 4.11b). The avarage fiber dimension related to cut thickness is equal to 30.8 ± 13.4 μm. It is notable the behaviour of fibers to mantain the proper shape and to approach each other in clusters. *Ghederine et Al.* [98] used a similar approach obtaining, via ultracentrifugal spinning, dispersed mono fibers composed of PCL magnetic-responsive alignment ability for nerve regeneration application. In this study is evidenced how a cutting thickness higher than 25 μm cause entanglement of dispersed fibers causing the failing of fibers alignment. In our study, however, the aim was not to orient the fibers in a preferential direction but to obtain a composite in which the DFs would isotropically distribute to confer an increase in mechanical properties. Furthermore, the fact that DFs these tend to aggregate or stick together transversely to form organised structures is related to the production process itself. The type of set-up we used resulted in aligned fibers with lateral melting points, unlike the one used in the reference study where was adopted a centrifugal spinning process to fabricate singular filament fibers mesh. Consequently, the cryomicro-cutting process implemented, only allows one characteristic dimension to be governed, while the length of these planar organised structures made up of fibers depends on a random disintegration process. Probabilistically, we therefore have a part of fibers that manage to disintegrate almost individually, while others remain attached to each other and form flat strip structures (Fig.4.12) having, in the worst case, a length equal to the size of the mesh before being cut.

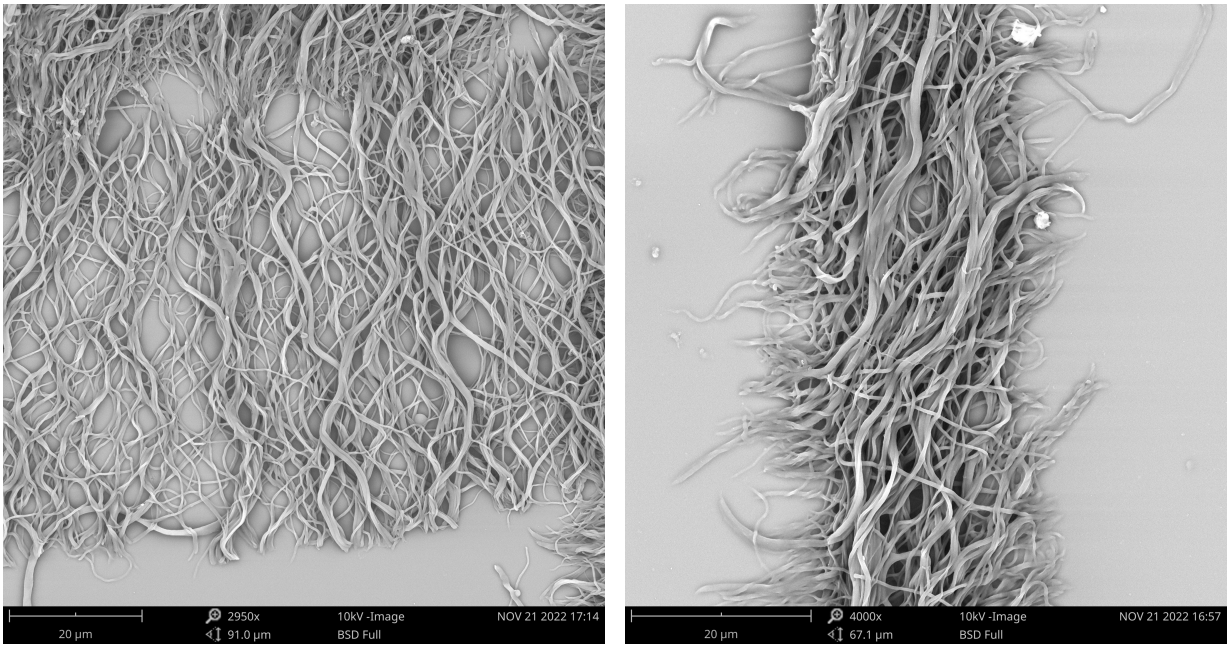

(a) (b)

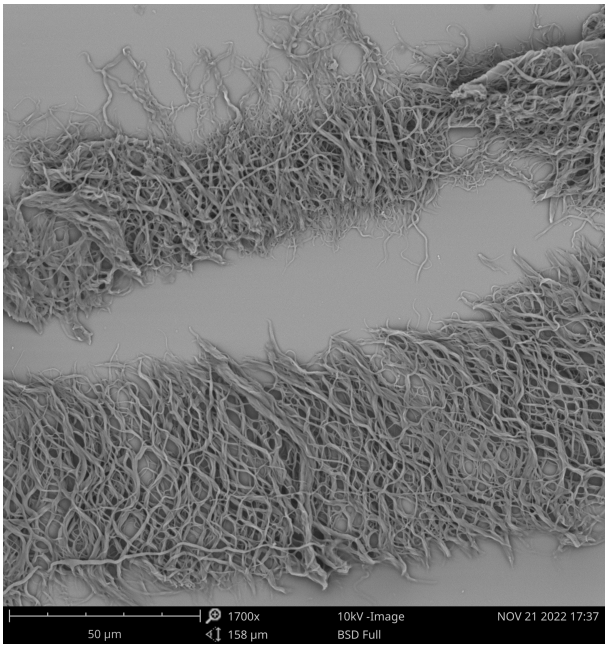

(c)

Figure 4.11: (a) DFs observed via SEM at 2950x, scale bar= 20 µm. (b) DFs observed via SEM, 4000x, scale bar= 20 µm. (c) DFs observed via SEM at 1700x, scale bar= 50 µm.

As reported in Fig.4.13 trough Hirox 3D digital microscope view, is also possible to notice the presence of these flat strip structures with different macroscopic length. To overcome this limitation of inhomogeneity, *Omidinia et Al.* [104] reported a comparable

approach for the production of DFs as well. The fabrication process exploited a parallel plate collector that enhance the evaporation rate of the solvent, avoiding fiber fusion and resulting in single filaments of PLGA [104]. For this reason, the design of a new set-up for the production of aligned fibers could lead to the fabrication of an isolated single filament mesh that if post-processed with cryomicro-cutting technique, would lead to a complete dispersion of mono-fibers.

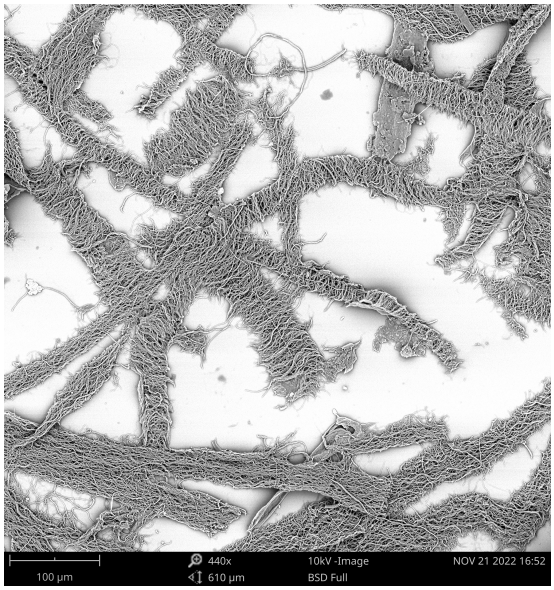

Figure 4.12: DFs obtained after cryomicro-cutting technique, 440x, scale bar= 100µm.

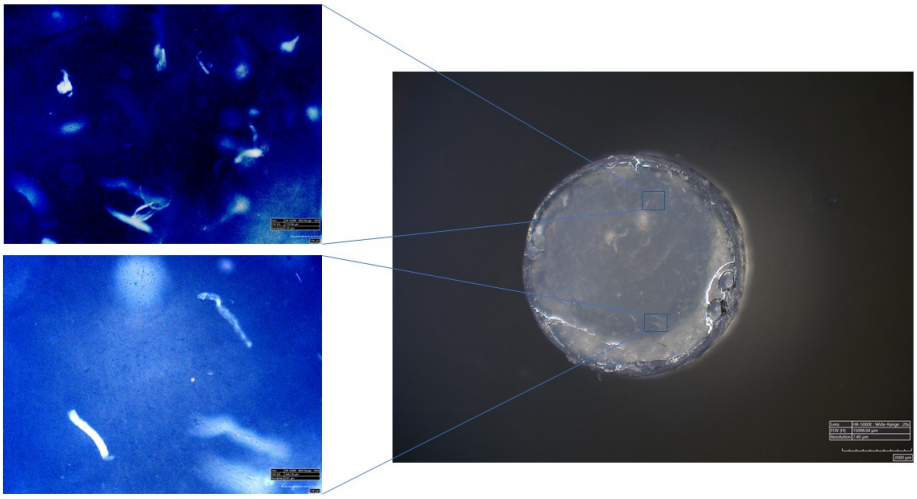

Figure 4.13: Wet GelMA+DFs samples show observable macroscopic DFs.

The porosity of GelMA and GelMA+NFs freeze-dried sample was calculated to be up to

85% for GelMA and up to 82% for GelMA+DFs, with an average pore size of 52 ± 5.6 and 48 ± 8,3 μm respectively. From these values it can be deduced, also supported by Fig. 4.14a and 4.14b, that the presence of DFs does not influence the morphology of the hydrogels. The DFs can be observed via SEM by increasing the degree of magnification up to 3000x, (Fig. 4.15).

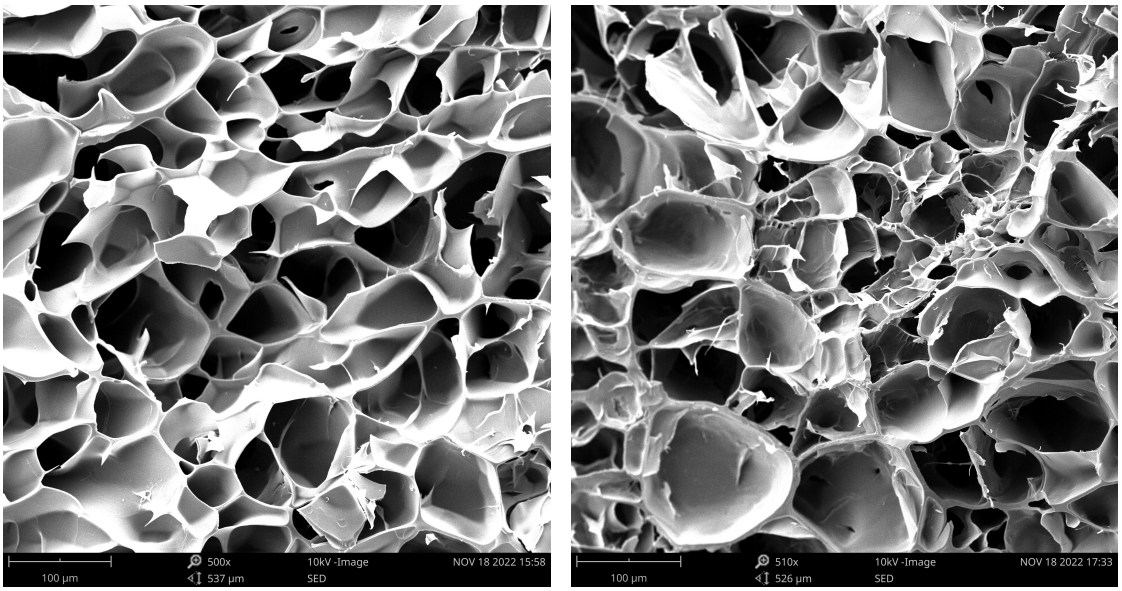

(a) (b)

Figure 4.14: Section view of freeze-dried photocrosslinked cylindrical samples with 300x and scale bar= 100 µm. Porosity and pore dimensions is estimated.

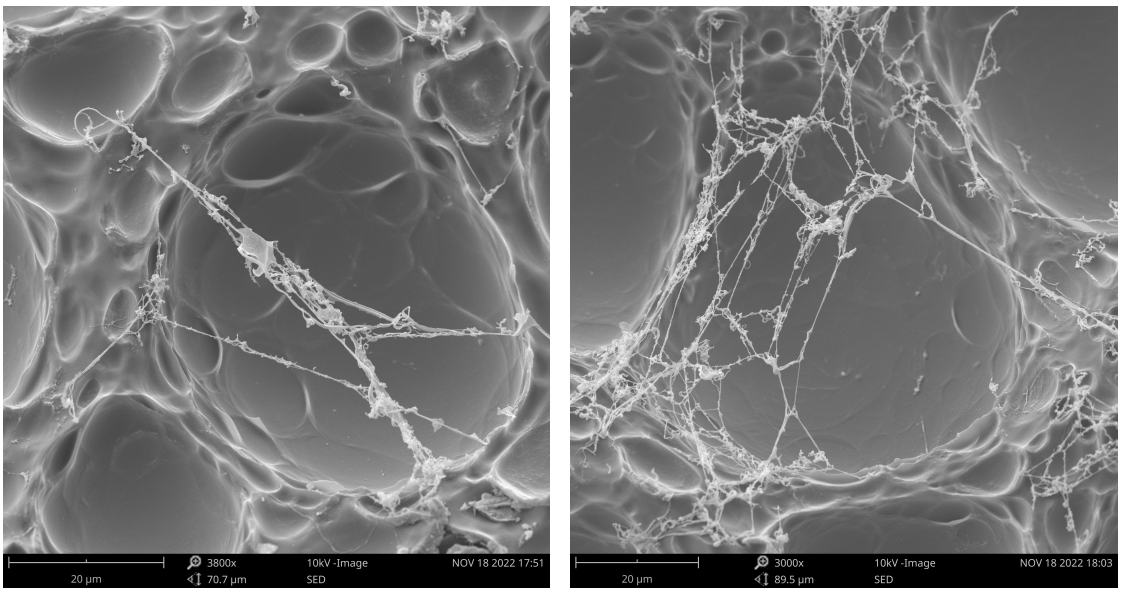

(a) (b)

Figure 4.15: Representative examples of intertwined DFs adhering in different points of bulk network. (a) 3800x and scale bar= 10 µm. (b) 3000x and scale bar= 10 µm

Qualitatively a good interaction between DFs and the bulk material is observable, showing multiple contact sites on the GelMA surface, suggesting that a positive integration of DFs, for a 0,5% w/v concentration, in GelMA network occurred, probably due to the presence of GelMA in the fibers, which may contribute to a higher level of integration with the GelMA network upon light crosslinking.

The DFs that have managed to break up quasi-singularly, assume in freeze-dried samples a dispersed behaviour, mantaining the cutting order of magnitude of tens of μm and the characteristic fiber-like morphology. Acting between different points of the bulk material, DFs behave as bridges within the GelMA network, absorbing a quantity of possible applied load in bearing application. In addition, it is well known that PCL is a material that does not absorb light, unlike other materials, so it does not affect light-mediated crosslinking as UV-light [122]. For example, other structured materials used as reinforcing agents, as barium titanate nanoparticles [123], if used as fillers in hydrogels in order to improve mechanical properties, show to be unsuitable for this type of crosslinking, by absorbing in the UV and visible light band [124]. Therefore, a filler strategy as the presented could be valid for improve the mechanical characteristics without affecting the crosslinking mechanism and indeed improve the degree of crosslinking due to the presence of GelMA in the DFs.

4.5. Mechanical compression tests

The mechanical analysis shows how the integration of DFs within the GelMA network improved the mechanical properties of GelMA matrix material for compressive performance. In Tab.4.3 the obtained mechanical parameters are reported as mean value and SD.

Table 4.3: Mechanical compressive parameters from triplicate measures

Parameter	**GelMA**	**GelMA+DFs**	**unit**
Compressive Modulus	42 ± 7.7	70.8 ± 5.8	kPa
Maximal deformation	48.5 ± 4.6	60.8 ± 2.6	%
Maximal strength	71 ± 12.1	139.3 ± 10	kPa
Compressive toughness	2.6 ± 0.3	4 ± 0.19	J/m^2

The higher compressive modulus of GelMA+DFs points out how the composite, due to the presence of the DFs, exhibits a stiffer behaviour and thus be less compliant. However, it not acquires a brittle behaviour that makes it break sooner than the GelMA network alone. Rather composite reaches high maximal strength values, that correspond to the once at break, of up to 150 kPa, increasing the value by 100% compared to the GelMA one. This may be related to the fact that the fibers act in the GelMA as reinforcing fillers. This characteristic is related both to the intrinsic nature of the PCL fibers, which is an excellent mechanically performing degradable polymer, but also due to the 3D structure of the fibers themselves, which, being homogeneously distributed in the matrix, might bear part of the load, thus guaranteeing a strengthening of the composite. It is likely that the fibers increase stiffness for low deformation values by acting as rigid elements and instead deform greatly for gradually increasing deformations, giving the new character to the stress-strain curve (Fig. 4.16). The value of compressive modulus for GelMA+DFs is equal to of 70.8 ± 5.8 and is nearly doubled compared to the value of 42 ± 7.7 of GelMA network. The maximal deformation increases from 48.5 ± 4.6 % for GelMA to 60.8 ± 2.6% in GelMA+DFs, having higher deformations until breaking for composite material. Since the maximum strain and maximum stress turn out to have higher values for GelMA+DFs, consequently the toughness also have higher values of 4 ± 0.19 J/m^2.

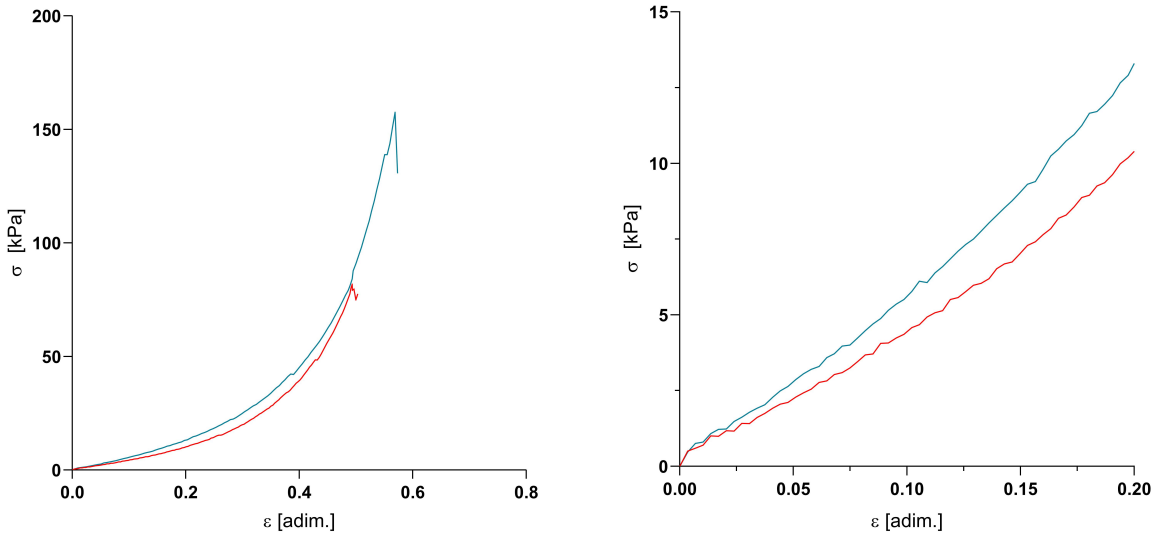

(a) (b)

Figure 4.16: (a) Representative stress-strain curves for GelMA (red) and GelMA+DFs (light blue) (b) Magnification of the linear region in the range 0-20% strain

Compared to the gelatin-based materials presented in the literature, our composite material is in a comparable range of mechanical characteristics under compression, especially for the values of compressive modulus and maximal strength [125]. However, compared to GelMA-based systems designed to be printed by assuming an organized 3D geometrical structures for OC treatment, it is mechanically inferior. *Liu et Al.* [126] reported a 3D-printed construct based on GelMA/nHA that showed, for multilayer printed structure with different GelMA concentration for each one, values of compressive modulus up to 600 kPa for the higher concentration ink. *Schuurman et Al.* [125] instead, have presented a 3D printed structure as well, using a 10% GelMA solution, obtaining compressive modulus of 50 kPa, approaching our value despite the use of 3D printing techniques. If compared to other studies where cast and cross-linked GelMA-based systems were used, our GelMA+DFs composite is a valid competitor *Celikk et Al.* [127] produce speciments of 10 mm of diameter and 1 mm of height with compressive modulus values in a range of tens of kPa. Additionally, for application where the bearing state is not a predominant aspect but not necessarily irrelevant, like dermal applications, was reported from *Zhao et Al* [128] lower compressive modulus and maximal strength values of 30 kPa and 20 kPa, displaying how our GelMA+DFs developed system, could be adapted and suitable to enlarge the mechanical performance of GelMA-based materials also in other applications.

The impact that various parameters can have on the mechanical outcome must be however emphasised when making a comparison. For example, differences in terms of specimen

geometry, type of lamp used, photo-crossing times, type of photoinitiator, type of gelatin used but also degree of functionalization may represent the main crucial aspects to be considered in project design phase to subsequently make a valid comparison between different systems. Nevertheless, there being able to achieve the highest necessary mechanical properties, reaching the features of native OC tissue (order of hundreds of kPa for compressive modulus up to MPa order for maximal strength) while ensuring a minimally invasive approach is still an open challange in the field of injectable hydrogels. Therefore, in order to make the characteristics of GelMA crosslinked hydrogel more mechanically performant, the introduction of a synthetic component that can be employed while maintaining injectability and that can either be trapped in the GelMA network crosslinked (creating a semi IPN), or crosslinking (creating an IPN) could go a long way towards, making the baseline bulk mechanical properties modulable. PVA is a candidate that, if properly designed, could undergo dynamic ionic crosslinking and simultaneously greatly increase the elastic character. Confirming this, *Zhao et Al.* [64] reported range of order of magnitude around 6 MPa for compressive modulus, 25 MPa for maximal strength and no fracture up to 95 % deformation for an injectable ultra strong PVA hydrogel with an in-situ crosslinking mechanism, far exceeding the corresponding values obtained for our GelMA+DFs composite.

The use of the natural component will ensure cell-friendly properties and, in combination with the synthetic component and the use of fiber-based reinforcement, an attempt will be made to increase the mechanical characteristics of the final construct. The PVA component at the same time may modulate the degradation rate of GelMA alone, which is intrinsically very fast due to the high presence of enzymes in biological environments capable of degrading it. Using a synthetic component as bulk material could increase the starting baseline of mechanical characteristics of the system to which the fiber filling could be applied in order to reach a order of magnitude of compressive modulus of tenths of MPa, in order to have a comparable value al least with the one of AC [129]. PVA as described is a synthetic material that lends itself to the target application of this study by showing potential properties of injectability, good cytocompatibility and bioresorbability ensuring a safe in situ crosslinking mechanism. Therefore, ongoing experiments are taking place on the optimisation of an s-IPN system consisting of cross-linkable GelMA and dispersed PVA chains. It will first be investigated whether PVA will have an impact on the crosslinking efficiency, once evaluated, on the compressive mechanical properties and injectability features. The sets of experiments will be carried out also in combination with DFs. Subsequently, the focus will be on the IPN approach and a clearer and broader spectrum of how the characteristics of GelMA can be tuned for OC applications.

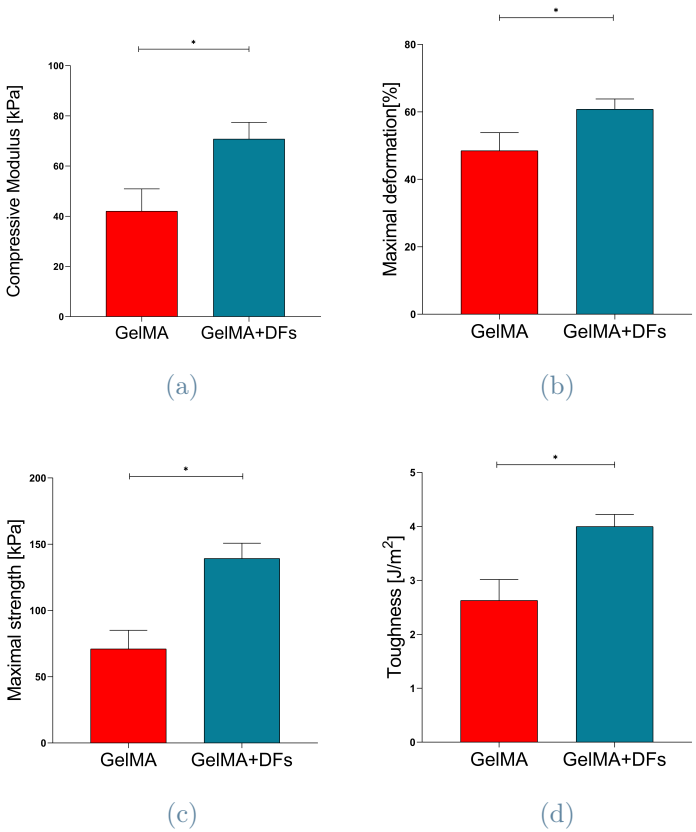

Figure 4.17: GelMA (red) and GelMA+DFs (light blue) compressive mechanical properties: (a) Compressive Modulus. (b) Maximal deformation. (c) Maximal strength. (d) Compressive toughness.

.

4.6. Physical characterization

The swelling profile of the samples shows a decreasing trend for the first 12 h with a subsequent reversal of behaviour from the 12 h hour onwards. This initial behaviour in the first 12h can be attributed to the fact that, as the sol-fraction analysis also suggests, there is initially a weight loss that is related to the dissolution of the uncrosslinked solid phase, which impacts the swelling calculation (being a function of the weight of the samples over time). This does not exclude a possible condition in which, for the first 12 h, there is a simultaneous flow of water to/from the samples. The net contribution between uncrosslinked solid phase loss and water uptake/loss leads to a total decrease in the sample weigth for the first 12 h. From around 12 h onwards there is a reversal of the swelling profile which starts to increase, suggesting that there is a net flow of water uptake by the sample. The swelling behaviour after 12 h grows very slowly and the calculated swelling values (%) at the time points of 24, 36, 48 and 96 h are very similar to each other

with an small % variation between one point and the following one.

The sol-fraction quantification was calculated to be around the value of 30% (Fig.3.7) and represents the weight fraction of polymer chains that are not covalently bound to the hydrogel network after photo-polymerization. The sol-fraction is therefore an aliquot of by weight of the total solid phase that is uncrosslinked. This aliquot over 24 h at 37 °C therefore solubilises in DIW. This value of sol-fraction is in line with those considered as satisfayng for a proper crosslinking in hydrogels, according to *Lim. et Al.* [130]. Tests on GelMA+DFs are in progress and will be presented as available.

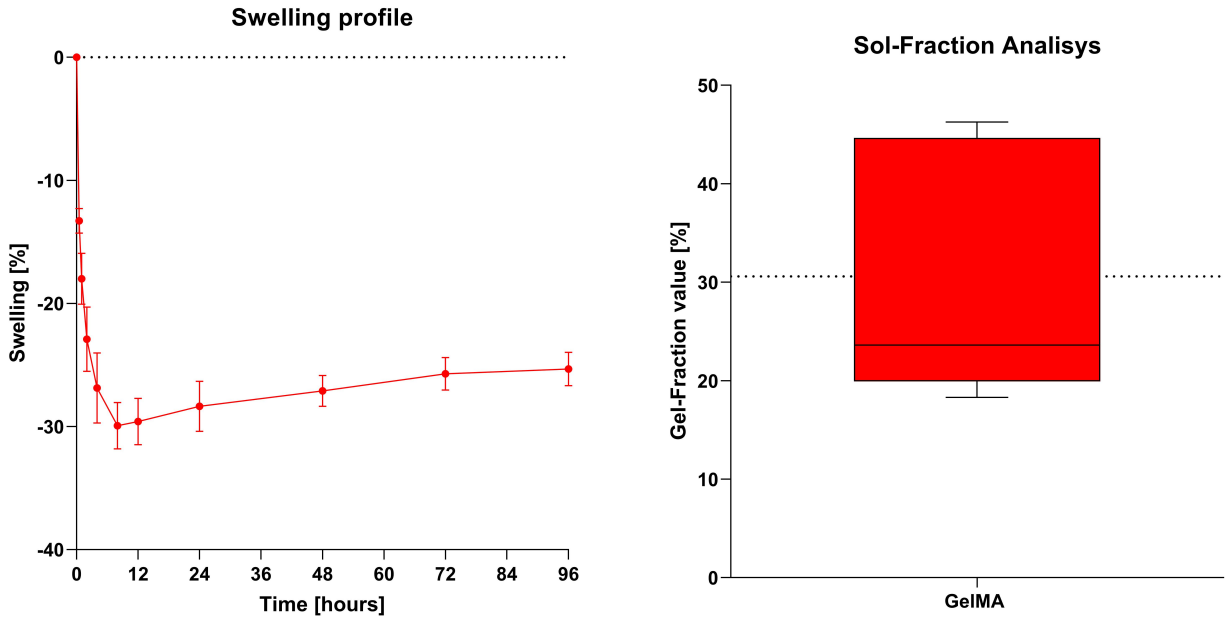

(a) (b)

Figure 4.18: (a) Swelling profile over time. At 24h a saturation time point is considered (b) Sol-Fraction value at 24h in DIW at 37° C.

5 | Conclusions and future developments

A deep investigation on the limitations of a missing resolutive intervention type for osteochondral defects treatment pointed out the need to switch towards a mini-invasive system that could replace the nowadays used devices in the clinical scenario, which have shown questionable regenerative outcomes and being applied through invasive surgeries. Additional socio-economic problems are to be linked to the general picture and are to be associated both to the high cost of the unsuccessful techniques implemented and sanitary expenses, and to the problems resulting from failing to treat patients. The objective of the presented thesis work, has been set to investigate the mechanical compressive performance and injectability of an acellular composite photo-crosslikable gelatin-based hydrogel loaded with a fibers-based filling.

It was shown that trough a post-processing of electruspun meshes of aligned fibers, with a cryomicro-cutting technique, it was possible to obtain almost mono dispersed fibers and organized microstructures composed of fibers. The process provided fiber-structured elements with a controllable dimension of cutting of 20 μm, suggesting an accurate production control and reproducility in cryomicro-cutting technique. The formation of composite design was demonstrated to be an effective approach to increase the mechanical compressive properties of the resultant GelMA+DFs crosslinked composite hydrogel. Values of compressive modulus, maximal strength, maximal deformation and toughness increase, doubling almost the ones of GelMA alone. It has been demonstrated that the DFs, once embedded in GelMA hydrogel to photo-crosslink the composite, have an interaction with the bulk material, due to the GelMA component in fibers PCL:GelMA-blend. The dependence of the viscoelastic and flow properties of the material on temperature showed that a boundary value for injectability can be drawn for temperature down to 30 °C. Then, the injectability study of the GelMA solution suggests the indicative operating set of parameters for which the material is injectable in a range of clinical applicability, where the EN ISO 7886 1:2018 sets 10 N as value for comfortable injection. The study report therefore a novel composite consisting of microstructured fiber elements dispersed

in a GelMA network with enhanced mechanical properties capable of possibly be used as mini-invasive system for osteochondral application.
Some experimental tests are still ongoing, e.g., the injectability force, the swelling behavior and the sol fraction featuring the GelMA + DFs material. These results would complete the set of experiments concerning this thesis.

Future verifications will enclose the maintenance of the injectability properties for different GelMA+DFNs configuration in terms of DFs concentration. This aspect certainly will depend on the length of the fibers and the concentration, so the best compromise must be sought in order to guarantee the best mechanical properties and injectability. Nevertheless, the closest future step will be to verify the injectability of GelMA10%+DF0.5% for 18G and 37 °C configuration.

The possibility of conceiving the bulk material not as a single network but as double entangled networks using PVA as a second type of polymer chain will be contemporary considered in ongoing investigations, in order to increase the baseline of mechanical properties from which apply a filling strategy and possibly act also on injetability feature. The secondary PVA network crosslinked with boron derivatives, may reduce even more the brittle behaviour and act as a ductile network sustaining large deformations with a result of much more synergistically high strength and toughness outcomes than those presented. Ionic-covalent entanglement GelMA/PVA hydrogel could be formed by an ionically crosslinked for PVA dynamic network and a covalently crosslinked for GelMA network, which allows self-healing of the primary network upon high stress condition. The realisation of a new set-up for the fabrication of electrospun meshes with an aligned configuration will also be a possible way to overcome the presence of fibres that are not well dispersed but organised as strip structures, following post-processing with cryomicrocutting technique.

Finally, for the success of the device future studies will involve an assessment of cytocompatibility as first step, followed by an evaluation of the capacity of chondrocytes first and bone mesenchimal stem cells (BMSCs) to adhere to the surface of the crosslinked composite and later to colonize it. Degradation tests should be carried out in host like conditions, in order to known approximately the behave of the device once implanted. Cells viability tests will follow coupled with a study of the capacity of the device to induce the proper chondro-osteo differentiation evaluating the relative gene expression of cells over time. To mimick as much as possible the biological conditions after a hypotized treatment, the ideal environment should be a bioreactor with dynamic bearing sollecitation in a walk with crutch force range with a predetermined degree of inflammation state.

Bibliography

[1] Ali Mobasheri and Mark Batt. An update on the pathophysiology of osteoarthritis. *Annals of Physical and Rehabilitation Medicine*, 59(5):333–339, 2016.

[2] Diego Trucco, Lorenzo Vannozzi, Eti Teblum, Madina Telkhozhayeva, Gilbert Daniel Nessim, Saverio Affatato, Hind Al-Haddad, Gina Lisignoli, and Leonardo Ricotti. Graphene oxide-doped gellan gum–pegda bilayered hydrogel mimicking the mechanical and lubrication properties of articular cartilage. *Advanced healthcare materials*, 10(7):2001434, 2021.

[3] JS Jurvelin, MD Buschmann, and EB Hunziker. Mechanical anisotropy of the human knee articular cartilage in compression. *Proceedings of the Institution of Mechanical Engineers, Part H: Journal of Engineering in Medicine*, 217(3):215–219, 2003.

[4] Ramaswamy Krishnan, Seonghun Park, Felix Eckstein, and Gerard A Ateshian. Inhomogeneous cartilage properties enhance superficial interstitial fluid support and frictional properties, but do not provide a homogeneous state of stress. *J. Biomech. Eng.*, 125(5):569–577, 2003.

[5] Teng Su, Yi Liu, Hongjian He, Jia Li, Yanan Lv, Lili Zhang, Yao Sun, and Chunpu Hu. Strong bioinspired polymer hydrogel with tunable stiffness and toughness for mimicking the extracellular matrix. *ACS Macro Letters*, 5(11):1217–1221, 2016.

[6] AJ Kerin, MR Wisnom, and MA Adams. The compressive strength of articular cartilage. *Proceedings of the Institution of Mechanical Engineers, Part H: Journal of Engineering in Medicine*, 212(4):273–280, 1998.

[7] Sarah IM Lepage, Naomi Robson, Hillary Gilmore, Ola Davis, Allyssa Hooper, Stephanie St. John, Vashine Kamesan, Paul Gelis, Diana Carvajal, Mark Hurtig, et al. Beyond cartilage repair: the role of the osteochondral unit in joint health and disease. *Tissue Engineering Part B: Reviews*, 25(2):114–125, 2019.

[8] Magdalena Muller-Gerbl. The subchondral bone plate. 2013.

[9] Wenying Wei and Honglian Dai. Articular cartilage and osteochondral tissue engineering techniques: Recent advances and challenges. *Bioactive materials*, 6(12):4830–4855, 2021.

[10] Alice J Sophia Fox, Asheesh Bedi, and Scott A Rodeo. The basic science of articular cartilage: structure, composition, and function. *Sports health*, 1(6):461–468, 2009.

[11] Henning Madry, C Niek van Dijk, and Magdalena Mueller-Gerbl. The basic science of the subchondral bone. *Knee surgery, sports traumatology, arthroscopy*, 18(4):419–433, 2010.

[12] DM Salter, SJ Millward-Sadler, G Nuki, and MO Wright. Differential responses of chondrocytes from normal and osteoarthritic human articular cartilage to mechanical stimulation. *Biorheology*, 39(1-2):97–108, 2002.

[13] Adrian C Shieh and Kyriacos A Athanasiou. Principles of cell mechanics for cartilage tissue engineering. *Annals of biomedical engineering*, 31(1):1–11, 2003.

[14] Silvia Ravalli, Marta Anna Szychlinska, Giovanni Lauretta, and Giuseppe Musumeci. New insights on mechanical stimulation of mesenchymal stem cells for cartilage regeneration. *Applied Sciences*, 10(8):2927, 2020.

[15] Jingming Gao, Xiaoquan Ding, Xiaoye Yu, Xiaobin Chen, Xingyu Zhang, Shuquan Cui, Jiayue Shi, Jun Chen, Lin Yu, Shiyi Chen, et al. Cell-free bilayered porous scaffolds for osteochondral regeneration fabricated by continuous 3d-printing using nascent physical hydrogel as ink. *Advanced Healthcare Materials*, 10(3):2001404, 2021.

[16] CPT Jessica D Rivera, Joseph C Wenke, Joseph A Buckwalter, COL James R Ficke, and LTC Anthony E Johnson. Posttraumatic osteoarthritis caused by battlefield injuries: the primary source of disability in warriors. *The Journal of the American Academy of Orthopaedic Surgeons*, 20(0 1):S64, 2012.

[17] DI Chen, Jie Shen, Weiwei Zhao, Tingyu Wang, Lin Han, John L Hamilton, and Hee-Jeong Im. Osteoarthritis: toward a comprehensive understanding of pathological mechanism. *Bone research*, 5(1):1–13, 2017.

[18] Yoke Yue Chow and Kok-Yong Chin. The role of inflammation in the pathogenesis of osteoarthritis. *Mediators of inflammation*, 2020, 2020.

[19] Peter Angele, Philipp Niemeyer, Matthias Steinwachs, Giuseppe Filardo, Andreas H Gomoll, Elizaveta Kon, Johannes Zellner, and Henning Madry. Chondral and os-

teochondral operative treatment in early osteoarthritis. *Knee Surgery, Sports Traumatology, Arthroscopy*, 24(6):1743–1752, 2016.

[20] Matthew Howell, Quintin Liao, and Christopher W Gee. Surgical management of osteochondral defects of the knee: an educational review. *Current Reviews in Musculoskeletal Medicine*, 14(1):60–66, 2021.

[21] Syam P. Nukavarapu and Deborah L. Dorcemus. Osteochondral tissue engineering: Current strategies and challenges. *Biotechnology Advances*, 31(5):706–721, 2013. Pearl (30th) Anniversary Edition: Nanotechnology & Regenerative Medicine.

[22] Diana Bicho, Sandra Pina, Rui L Reis, and J Miguel Oliveira. Commercial products for osteochondral tissue repair and regeneration. *Osteochondral Tissue Engineering*, pages 415–428, 2018.

[23] Elizaveta Kon, Marco Delcogliano, Giuseppe Filardo, Milena Fini, Gianluca Giavaresi, Silvia Francioli, Ivan Martin, Daniele Pressato, Elena Arcangeli, Rodolfo Quarto, et al. Orderly osteochondral regeneration in a sheep model using a novel nano-composite multilayered biomaterial. *Journal of Orthopaedic Research*, 28(1):116–124, 2010.

[24] Bjørn Borsøe Christensen, Casper Bindzus Foldager, Jonas Jensen, Niels Christian Jensen, and Martin Lind. Poor osteochondral repair by a biomimetic collagen scaffold: 1-to 3-year clinical and radiological follow-up. *Knee surgery, sports traumatology, arthroscopy*, 24(7):2380–2387, 2016.

[25] Alan Getgood, Frances Henson, Carrie Skelton, Roger Brooks, Hans Guehring, Lisa A Fortier, and Neil Rushton. Osteochondral tissue engineering using a biphasic collagen/gag scaffold containing rhfgf18 or bmp-7 in an ovine model. *Journal of experimental orthopaedics*, 1(1):1–11, 2014.

[26] Paul Hindle, Jane L Hendry, John F Keating, and Leela C Biant. Autologous osteochondral mosaicplasty or trufit™ plugs for cartilage repair. *Knee Surgery, Sports Traumatology, Arthroscopy*, 22(6):1235–1240, 2014.

[27] F Falez and FV Sciarretta. Treatment of osteochondral symptomatic defects of the knee with salucartilage. In *Orthopaedic Proceedings*, volume 87, pages 202–202. The British Editorial Society of Bone & Joint Surgery, 2005.

[28] Elizaveta Kon, Berardo Di Matteo, Peter Verdonk, Matej Drobnic, Oliver Dulic, Gordan Gavrilovic, Jenel M Patrascu, Ken Zaslav, Grzegorz Kwiatkowski, Nir Altschuler, et al. Aragonite-based scaffold for the treatment of joint surface lesions

in mild to moderate osteoarthritic knees: results of a 2-year multicenter prospective study. *The American Journal of Sports Medicine*, 49(3):588–598, 2021.

[29] Louis Kluyskens, Pedro Debieux, Keng Lin Wong, Aaron J Krych, and Daniel BF Saris. Biomaterials for meniscus and cartilage in knee surgery: state of the art. *Journal of ISAKOS*, 2022.

[30] Andrea Fontana. A novel technique for treating cartilage defects in the hip: A fully arthroscopic approach to using autologous matrix-induced chondrogenesis. *Arthroscopy Techniques*, 1(1):e63–e68, 2012.

[31] Ian Jun Yan Wee, Thomas Stonier, Michael Harrison, and Andrew MTL Choong. Transcarotid transcatheter aortic valve implantation: A systematic review. *Journal of Cardiology*, 71(6):525–533, 2018.

[32] Amir Mellati and Javad Akhtari. Injectable hydrogels: A review of injectability mechanisms and biomedical applications. *Research in Molecular Medicine (RMM)*, pages 1–14, 2019.

[33] Øystein Øvrebø, Giuseppe Perale, Jonathan P Wojciechowski, Cécile Echalier, Jonathan RT Jeffers, Molly M Stevens, Håvard J Haugen, and Filippo Rossi. Design and clinical application of injectable hydrogels for musculoskeletal therapy. *Bioengineering & Translational Medicine*, page e10295, 2022.

[34] Domagoj Coric and Praveen V Mummaneni. Nucleus replacement technologies: Invited submission from the joint section meeting on disorders of the spine and peripheral nerves, march 2007. *Journal of Neurosurgery: Spine*, 8(2):115–120, 2008.

[35] Whitney L Stoppel, Chiara E Ghezzi, Stephanie L McNamara, David L Kaplan, et al. Clinical applications of naturally derived biopolymer-based scaffolds for regenerative medicine. *Annals of biomedical engineering*, 43(3):657–680, 2015.

[36] Lubomir Medvecky, Maria Giretova, Radoslava Stulajterova, Jan Danko, Katarina Vdoviakova, Lenka Kresakova, Zdenek Zert, Eva Petrovova, Katarina Holovska, Maros Varga, Lenka Luptakova, and Tibor Sopcak. Characterization of properties, in vitro and in vivo evaluation of calcium phosphate/amino acid cements for treatment of osteochondral defects. *Materials*, 14(2), 2021.

[37] Santiago Correa, Abigail K Grosskopf, Hector Lopez Hernandez, Doreen Chan, Anthony C Yu, Lyndsay M Stapleton, and Eric A Appel. Translational applications of hydrogels. *Chemical Reviews*, 121(18):11385–11457, 2021.

[38] Danielle Lynne Taylor and Marc in het Panhuis. Self-healing hydrogels. *Advanced Materials*, 28(41):9060–9093, 2016.

[39] Francesco Cilurzo, Francesca Selmin, Paola Minghetti, Marco Adami, Elisa Bertoni, Sara Lauria, and Luisa Montanari. Injectability evaluation: an open issue. *AAPS PharmSciTech*, 12(2):604–609, 2011.

[40] Jose Maria Alonso, Jon Andrade del Olmo, Raul Perez Gonzalez, and Virginia Saez-Martinez. Injectable hydrogels: From laboratory to industrialization. *Polymers*, 13(4):650, 2021.

[41] Murat Guvendiren, Hoang D Lu, and Jason A Burdick. Shear-thinning hydrogels for biomedical applications. *Soft matter*, 8(2):260–272, 2012.

[42] Lin Yu and Jiandong Ding. Injectable hydrogels as unique biomedical materials. *Chemical Society Reviews*, 37(8):1473–1481, 2008.

[43] Andrea Allmendinger, Stefan Fischer, Joerg Huwyler, Hanns-Christian Mahler, Edward Schwarb, Isidro E. Zarraga, and Robert Mueller. Rheological characterization and injection forces of concentrated protein formulations: An alternative predictive model for non-newtonian solutions. *European Journal of Pharmaceutics and Biopharmaceutics*, 87(2):318–328, 2014.

[44] Armin Vedadghavami, Farnaz Minooei, Mohammad Hossein Mohammadi, Sultan Khetani, Ahmad Rezaei Kolahchi, Shohreh Mashayekhan, and Amir Sanati-Nezhad. Manufacturing of hydrogel biomaterials with controlled mechanical properties for tissue engineering applications. *Acta Biomaterialia*, 62:42–63, 2017.

[45] Chanjuan Dong and Yonggang Lv. Application of collagen scaffold in tissue engineering: Recent advances and new perspectives. *Polymers*, 8(2), 2016.

[46] Julie Glowacki and Shuichi Mizuno. Collagen scaffolds for tissue engineering. *Biopolymers*, 89(5):338–344, 2008.

[47] Shabnam Hemmati-Sadeghi, Jochen Ringe, Tilo Dehne, Rainer Haag, and Michael Sittinger. Hyaluronic acid influence on normal and osteoarthritic tissue-engineered cartilage. *International Journal of Molecular Sciences*, 19(5), 2018.

[48] Sio-Mei Lien, Liang-Yu Ko, and Ta-Jen Huang. Effect of crosslinking temperature on compression strength of gelatin scaffold for articular cartilage tissue engineering. *Materials Science and Engineering: C*, 30(4):631–635, 2010.

[49] Patrícia B. Malafaya, Gabriela A. Silva, and Rui L. Reis. Natural–origin polymers

as carriers and scaffolds for biomolecules and cell delivery in tissue engineering applications. *Advanced Drug Delivery Reviews*, 59(4):207–233, 2007. Matrices and Scaffolds for Drug Delivery in Tissue Engineering.

[50] Wenqiang Yan, Xingquan Xu, Qian Xu, Ziying Sun, Zhongyang Lv, Rui Wu, Wenjin Yan, Qing Jiang, and Dongquan Shi. An injectable hydrogel scaffold with kartogenin-encapsulated nanoparticles for porcine cartilage regeneration: a 12-month follow-up study. *The American journal of sports medicine*, 48(13):3233–3244, 2020.

[51] Dong-An Wang, Shyni Varghese, Blanka Sharma, Iossif Strehin, Sara Fermanian, Justin Gorham, D Howard Fairbrother, Brett Cascio, and Jennifer H Elisseeff. Multifunctional chondroitin sulphate for cartilage tissue–biomaterial integration. *Nature materials*, 6(5):385–392, 2007.

[52] Neven J Steinmetz and Stephanie J Bryant. Chondroitin sulfate and dynamic loading alter chondrogenesis of human mscs in peg hydrogels. *Biotechnology and Bioengineering*, 109(10):2671–2682, 2012.

[53] Nandana Bhardwaj and Subhas C. Kundu. Chondrogenic differentiation of rat mscs on porous scaffolds of silk fibroin/chitosan blends. *Biomaterials*, 33(10):2848–2857, 2012.

[54] Nandana Bhardwaj, Quynhhoa T. Nguyen, Albert C. Chen, David L. Kaplan, Robert L. Sah, and Subhas C. Kundu. Potential of 3-d tissue constructs engineered from bovine chondrocytes/silk fibroin-chitosan for in vitro cartilage tissue engineering. *Biomaterials*, 32(25):5773–5781, 2011.

[55] Jayachandran Venkatesan, Ira Bhatnagar, Panchanathan Manivasagan, Kyong-Hwa Kang, and Se-Kwon Kim. Alginate composites for bone tissue engineering: A review. *International Journal of Biological Macromolecules*, 72:269–281, 2015.

[56] Jinchen Sun and Huaping Tan. Alginate-based biomaterials for regenerative medicine applications. *Materials*, 6(4):1285–1309, 2013.

[57] Jiaqi Xing, Xu Peng, Anqi Li, Meilin Chen, Yuan Ding, Xinyuan Xu, Peng Yu, Jing Xie, and Jianshu Li. Gellan gum/alginate-based ca-enriched acellular bilayer hydrogel with robust interface bonding for effective osteochondral repair. *Carbohydrate Polymers*, 270:118382, 2021.

[58] Lígia Costa, Joana Silva-Correia, J Miguel Oliveira, and Rui L Reis. Gellan gum-

based hydrogels for osteochondral repair. *Osteochondral Tissue Engineering*, pages 281–304, 2018.

[59] Jingyi Liu, Liang Li, Hairui Suo, Mengling Yan, Jun Yin, and Jianzhong Fu. 3d printing of biomimetic multi-layered gelma/nha scaffold for osteochondral defect repair. *Materials & Design*, 171:107708, 2019.

[60] Gang Tan, Jing Xu, Qin Yu, Jieyu Zhang, Xuefeng Hu, Chenwei Sun, and Hui Zhang. Photo-crosslinkable hydrogels for 3d bioprinting in the repair of osteochondral defects: A review of present applications and future perspectives. *Micromachines*, 13(7), 2022.

[61] Kan Yue, Grissel Trujillo-de Santiago, Mario Moisés Alvarez, Ali Tamayol, Nasim Annabi, and Ali Khademhosseini. Synthesis, properties, and biomedical applications of gelatin methacryloyl (gelma) hydrogels. *Biomaterials*, 73:254–271, 2015.

[62] Tzu-Hsiang Lin, Hsueh-Chun Wang, Meng-Chian Wu, Horng-Chaung Hsu, and Ming-Long Yeh. A bilineage thermosensitive hydrogel system for stimulation of mesenchymal stem cell differentiation and enhancement of osteochondral regeneration. *Composites Part B: Engineering*, 233:109614, 2022.

[63] Zhaleh Atoufi, Seyed Kamran Kamrava, Seyed Mohammad Davachi, Majid Hassanabadi, Sadaf Saeedi Garakani, Rafieh Alizadeh, Mohammad Farhadi, Shima Tavakol, Zohreh Bagher, and Ghodratollah Hashemi Motlagh. Injectable pnipam/hyaluronic acid hydrogels containing multipurpose modified particles for cartilage tissue engineering: Synthesis, characterization, drug release and cell culture study. *International journal of biological macromolecules*, 139:1168–1181, 2019.

[64] Yanran Zhao, Mengnan Li, Bingchuan Liu, Junfeng Xiang, Zhiyong Cui, Xiaozhong Qu, Dong Qiu, Yun Tian, and Zhenzhong Yang. Ultra-tough injectable cytocompatible hydrogel for 3d cell culture and cartilage repair. *Journal of Materials Chemistry B*, 6(9):1351–1358, 2018.

[65] Shifeng Yan, Xin Zhang, Kunxi Zhang, Hao Di, Long Feng, Guifei Li, Jianjun Fang, Lei Cui, Xuesi Chen, and Jingbo Yin. Injectable in situ forming poly (l-glutamic acid) hydrogels for cartilage tissue engineering. *Journal of Materials Chemistry B*, 4(5):947–961, 2016.

[66] JE Trachtenberg, JK Placone, BT Smith, CM Piard, M Santoro, DW Scott, JP Fisher, and AG Mikos. Extrusion-based printing of poly (propylene fumarate) for osteochondral tissue engineering. In *Front. Bioeng. Biotechnol. Conference Abstract: 10th World Biomaterials Congress*, 2016.

[67] Yogendra Pratap Singh, Joseph Christakiran Moses, Nandana Bhardwaj, and Biman B Mandal. Injectable hydrogels: a new paradigm for osteochondral tissue engineering. *Journal of Materials Chemistry B*, 6(35):5499–5529, 2018.

[68] Jin Seon Kwon, So Mi Yoon, Doo Yeon Kwon, Guo Zhe Tai, Ling Mei Jin, Boram Song, Bong Lee, Jae Ho Kim, Dong Keun Han, Byoung Hyun Min, et al. Injectable in situ-forming hydrogel for cartilage tissue engineering. *Journal of Materials Chemistry B*, 1(26):3314–3321, 2013.

[69] Anestis Papadopoulos, David A Bichara, Xing Zhao, Shinichi Ibusuki, Mark A Randolph, Kristi S Anseth, and Michael J Yaremchuk. Injectable and photopolymerizable tissue-engineered auricular cartilage using poly (ethylene glycol) dimethacrylate copolymer hydrogels. *Tissue Engineering Part A*, 17(1-2):161–169, 2011.

[70] Fei Gao, Ziyang Xu, Qingfei Liang, Bo Liu, Haofei Li, Yuanhao Wu, Yinyu Zhang, Zifeng Lin, Mingming Wu, Changshun Ruan, et al. Direct 3d printing of high strength biohybrid gradient hydrogel scaffolds for efficient repair of osteochondral defect. *Advanced functional materials*, 28(13):1706644, 2018.

[71] Abhishek P Dhand, Jonathan H Galarraga, and Jason A Burdick. Enhancing biopolymer hydrogel functionality through interpenetrating networks. *Trends in Biotechnology*, 39(5):519–538, 2021.

[72] Laura Pescosolido, Wouter Schuurman, Jos Malda, Pietro Matricardi, Franco Alhaique, Tommasina Coviello, P Rene van Weeren, Wouter JA Dhert, Wim E Hennink, and Tina Vermonden. Hyaluronic acid and dextran-based semi-ipn hydrogels as biomaterials for bioprinting. *Biomacromolecules*, 12(5):1831–1838, 2011.

[73] Jin-A Kim, Young-Hyeon An, Hyun-Gu Yim, Woo-Jung Han, Yong-Beom Park, Hyun Jin Park, Man Young Kim, Jaewon Jang, Racheal H Koh, Su-Hwan Kim, et al. Injectable fibrin/polyethylene oxide semi-ipn hydrogel for a segmental meniscal defect regeneration. *The American Journal of Sports Medicine*, 49(6):1538–1550, 2021.

[74] Hairui Suo, Deming Zhang, Jun Yin, Jin Qian, Zi Liang Wu, and Jianzhong Fu. Interpenetrating polymer network hydrogels composed of chitosan and photocrosslinkable gelatin with enhanced mechanical properties for tissue engineering. *Materials Science and Engineering: C*, 92:612–620, 2018.

[75] Bin Wang, Pedro J Diaz-Payno, David C Browe, Fiona E Freeman, Jessica Nulty, Ross Burdis, and Daniel J Kelly. Affinity-bound growth factor within sulfated

interpenetrating network bioinks for bioprinting cartilaginous tissues. *Acta Biomaterialia*, 128:130–142, 2021.

[76] Yan Guo, Tun Yuan, Zhanwen Xiao, Pingping Tang, Yumei Xiao, Yujiang Fan, and Xingdong Zhang. Hydrogels of collagen/chondroitin sulfate/hyaluronan interpenetrating polymer network for cartilage tissue engineering. *Journal of Materials Science: Materials in Medicine*, 23(9):2267–2279, 2012.

[77] Shuai Zhang, Yunlong Li, Hangjing Zhang, Guojun Wang, Hao Wei, Xinyue Zhang, and Ning Ma. Bioinspired conductive hydrogel with ultrahigh toughness and stable antiswelling properties for articular cartilage replacement. *ACS Materials Letters*, 3(6):807–814, 2021.

[78] Qing Gao, Xuefeng Niu, Lei Shao, Luyu Zhou, Zhiwei Lin, Anyu Sun, Jianzhong Fu, Zichen Chen, Jun Hu, Yande Liu, et al. 3d printing of complex gelma-based scaffolds with nanoclay. *Biofabrication*, 11(3):035006, 2019.

[79] Zhenqiang Dong, Qijuan Yuan, Keqing Huang, Wanli Xu, Guiting Liu, and Zhipeng Gu. Gelatin methacryloyl (gelma)-based biomaterials for bone regeneration. *RSC advances*, 9(31):17737–17744, 2019.

[80] Hang Wang, Lei Zhou, Jingwen Liao, Ying Tan, Kongyou Ouyang, Chenyun Ning, Guoxin Ni, and Guoxin Tan. Cell-laden photocrosslinked gelma–dexma copolymer hydrogels with tunable mechanical properties for tissue engineering. *Journal of Materials Science: Materials in Medicine*, 25(9):2173–2183, 2014.

[81] Yihu Wang, Ming Ma, Jianing Wang, Weijie Zhang, Weipeng Lu, Yunhua Gao, Bing Zhang, and Yanchuan Guo. Development of a photo-crosslinking, biodegradable gelma/pegda hydrogel for guided bone regeneration materials. *Materials*, 11(8):1345, 2018.

[82] Akhilesh K Gaharwar, Nicholas A Peppas, and Ali Khademhosseini. Nanocomposite hydrogels for biomedical applications. *Biotechnology and bioengineering*, 111(3):441–453, 2014.

[83] Yanlun Zhu, Lingzhi Kong, Fatemeh Farhadi, Wei Xia, Jiang Chang, Yaohua He, and Haiyan Li. An injectable continuous stratified structurally and functionally biomimetic construct for enhancing osteochondral regeneration. *Biomaterials*, 192:149–158, 2019.

[84] Li Zheng, Xianfang Jiang, Xuening Chen, Hongsong Fan, and Xingdong Zhang. Evaluation of novel in situ synthesized nano-hydroxyapatite/collagen/alginate hy-

drogels for osteochondral tissue engineering. *Biomedical Materials*, 9(6):065004, 2014.

[85] Niloofar Eslahi, Abdolreza Simchi, Morteza Mehrjoo, Mohammad Ali Shokrgozar, and Shahin Bonakdar. Hybrid cross-linked hydrogels based on fibrous protein/block copolymers and layered silicate nanoparticles: tunable thermosensitivity, biodegradability and mechanical durability. *RSC advances*, 6(67):62944–62957, 2016.

[86] Naiyin Zhang, Jaclyn Lock, Amy Sallee, and Huinan Liu. Magnetic nanocomposite hydrogel for potential cartilage tissue engineering: synthesis, characterization, and cytocompatibility with bone marrow derived mesenchymal stem cells. *ACS applied materials & interfaces*, 7(37):20987–20998, 2015.

[87] Ziyuan Fang, Kun Qiao, Yansen Wang, Yudong Zheng, Wei He, Yajie Xie, and Huiyi Yang. Injectable and biodegradable double-network nanocomposite hydrogel with regulable sol-gel transition process and mechanical properties. *Polymer Testing*, 106:107452, 2022.

[88] Arianna De Mori, Marta Peña Fernández, Gordon Blunn, Gianluca Tozzi, and Marta Roldo. 3d printing and electrospinning of composite hydrogels for cartilage and bone tissue engineering. *Polymers*, 10(3), 2018.

[89] Lucy A. Bosworth, Lesley-Anne Turner, and Sarah H. Cartmell. State of the art composites comprising electrospun fibres coupled with hydrogels: a review. *Nanomedicine: Nanotechnology, Biology and Medicine*, 9(3):322–335, 2013.

[90] Elia A Guzzi and Mark W Tibbitt. Additive manufacturing of precision biomaterials. *Advanced materials*, 32(13):1901994, 2020.

[91] Annabel L. Butcher, Giovanni S. Offeddu, and Michelle L. Oyen. Nanofibrous hydrogel composites as mechanically robust tissue engineering scaffolds. *Trends in Biotechnology*, 32(11):564–570, 2014.

[92] Nandana Bhardwaj and Subhas C. Kundu. Electrospinning: A fascinating fiber fabrication technique. *Biotechnology Advances*, 28(3):325–347, 2010.

[93] Anne Hsieh, Tasneem Zahir, Yakov Lapitsky, Brian Amsden, Wankei Wan, and Molly S Shoichet. Hydrogel/electrospun fiber composites influence neural stem/progenitor cell fate. *Soft Matter*, 6(10):2227–2237, 2010.

[94] Fang Yongcong, Ting Zhang, Liliana Liverani, Aldo R Boccaccini, and Wei Sun. Novel biomimetic fiber incorporated scaffolds for tissue engineering. *Journal of Biomedical Materials Research Part A*, 107(12):2694–2705, 2019.

[95] Zhang-Qi Feng, Chuanmei Shi, Bin Zhao, and Ting Wang. Magnetic electrospun short nanofibers wrapped graphene oxide as a promising biomaterials for guiding cellular behavior. *Materials Science and Engineering: C*, 81:314–320, 2017.

[96] Seema Agarwal, Joachim H. Wendorff, and Andreas Greiner. Use of electrospinning technique for biomedical applications. *Polymer*, 49(26):5603–5621, 2008.

[97] Beata Niemczyk-Soczynska, Judyta Dulnik, Oliwia Jeznach, Dorota Kolbuk, and Pawel Sajkiewicz. Shortening of electrospun plla fibers by ultrasonication. *Micron*, 145:103066, 2021.

[98] Paria Ghaderinejad, Najmeh Najmoddin, Zohreh Bagher, Mahdi Saeed, Sarah Karimi, Sara Simorgh, and Mohamad Pezeshki-Modaress. An injectable anisotropic alginate hydrogel containing oriented fibers for nerve tissue engineering. *Chemical Engineering Journal*, 420:130465, 2021.

[99] Maria Ann Woodruff and Dietmar Werner Hutmacher. The return of a forgotten polymer—polycaprolactone in the 21st century. *Progress in polymer science*, 35(10):1217–1256, 2010.

[100] Marini Sawawi, Ting Yi Wang, David R Nisbet, and George P Simon. Scission of electrospun polymer fibres by ultrasonication. *Polymer*, 54(16):4237–4252, 2013.

[101] Chiaki Yoshikawa, Kun Zhang, Ewelina Zawadzak, and Hisatoshi Kobayashi. A novel shortened electrospun nanofiber modified with a 'concentrated' polymer brush. *Science and technology of advanced materials*, 12(1):015003, February 2011.

[102] Taek Gyoung Kim and Tae Gwan Park. Biodegradable polymer nanocylinders fabricated by transverse fragmentation of electrospun nanofibers through aminolysis. *Macromolecular rapid communications*, 29(14):1231–1236, 2008.

[103] Aleksandar Stoiljkovic, Rajan Venkatesh, Evgueni Klimov, Vijay Raman, Joachim H Wendorff, and Andreas Greiner. Poly (styrene-co-n-butyl acrylate) nanofibers with excellent stability against water by electrospinning from aqueous colloidal dispersions. *Macromolecules*, 42(16):6147–6151, 2009.

[104] Abdolrahman Omidinia-Anarkoli, Sarah Boesveld, Urandelger Tuvshindorj, Jonas C Rose, Tamás Haraszti, and Laura De Laporte. An injectable hybrid hydrogel with oriented short fibers induces unidirectional growth of functional nerve cells. *Small*, 13(36):1702207, 2017.

[105] Kyung Jin Lee, Jaewon Yoon, Sahar Rahmani, Sangyeul Hwang, Srijanani Bhaskar, Samir Mitragotri, and Joerg Lahann. Spontaneous shape reconfigurations in mul-

ticompartmental microcylinders. *Proceedings of the National Academy of Sciences*, 109(40):16057–16062, 2012.

[106] Daniela Loessner, Christoph Meinert, Elke Kaemmerer, Laure C Martine, Kan Yue, Peter A Levett, Travis J Klein, Ferry PW Melchels, Ali Khademhosseini, and Dietmar W Hutmacher. Functionalization, preparation and use of cell-laden gelatin methacryloyl–based hydrogels as modular tissue culture platforms. *Nature protocols*, 11(4):727–746, 2016.

[107] Jun Yin, Mengling Yan, Yancheng Wang, Jianzhong Fu, and Hairui Suo. 3d bioprinting of low-concentration cell-laden gelatin methacrylate (gelma) bioinks with a two-step cross-linking strategy. *ACS applied materials & interfaces*, 10(8):6849–6857, 2018.

[108] Ping Song, Mingxin Li, Boqing Zhang, Xingyu Gui, Yanlong Han, Li Wang, Wenzheng Zhou, Likun Guo, Zhenyu Zhang, Zhengyong Li, Changchun Zhou, Yujiang Fan, and Xingdong Zhang. Dlp fabricating of precision gelma/hap porous composite scaffold for bone tissue engineering application. *Composites Part B: Engineering*, 244:110163, 2022.

[109] Tommaso Mazzocchi, Daniele Guarnera, Diego Trucco, Francesco Rocco Restaino, Lorenzo Vannozzi, Alessio Siliberto, Gina Lisignoli, Stefano Zaffagnini, Alessandro Russo, and Leonardo Ricotti. A novel approach for multiple material extrusion in arthroscopic knee surgery. *Annals of Biomedical Engineering*, pages 1–16, 2022.

[110] Nitin Rathore, Pratik Pranay, Bruce Eu, Wenchang Ji, and Ed Walls. Variability in syringe components and its impact on functionality of delivery systems. *PDA Journal of Pharmaceutical Science and Technology*, 65(5):468–480, 2011.

[111] Hairui Suo, Deming Zhang, Jun Yin, Jin Qian, Zi Liang Wu, and Jianzhong Fu. Interpenetrating polymer network hydrogels composed of chitosan and photocrosslinkable gelatin with enhanced mechanical properties for tissue engineering. *Materials Science and Engineering: C*, 92:612–620, 2018.

[112] Kaveh Rahimi Mamaghani, Seyed Morteza Naghib, Alireza Zahedi, and Masoud Mozafari. Synthesis and microstructural characterization of gelma/pegda hybrid hydrogel containing graphene oxide for biomedical purposes. *Materials Today: Proceedings*, 5(7, Part 3):15635–15644, 2018. INN International Conference/Workshop on "Nanotechnology and Nanomedicine" (NTNM2017), 2-3 May 2017.

[113] Sahar Abdollahi Baghban, Morteza Ebrahimi, Shadab Bagheri-Khoulenjani, and Manoucher Khorasani. A highly efficient microwave-assisted synthesis of an led-

curable methacrylated gelatin for bio applications. *RSC advances*, 11(25):14996–15009, 2021.

[114] P Coimbra, Patrícia Santos, P Alves, Sónia P Miguel, Marco P Carvalho, Kevin D de Sá, IJ Correia, and P Ferreira. Coaxial electrospun pcl/gelatin-ma fibers as scaffolds for vascular tissue engineering. *Colloids and Surfaces B: Biointerfaces*, 159:7–15, 2017.

[115] Hitomi Shirahama, Bae Hoon Lee, Lay Poh Tan, and Nam-Joon Cho. Precise tuning of facile one-pot gelatin methacryloyl (gelma) synthesis. *Scientific reports*, 6(1):1–11, 2016.

[116] Mengxiang Zhu, Yingying Wang, Gaia Ferracci, Jing Zheng, Nam-Joon Cho, and Bae Hoon Lee. Gelatin methacryloyl and its hydrogels with an exceptional degree of controllability and batch-to-batch consistency. *Scientific reports*, 9(1):1–13, 2019.

[117] NS Deshpande and Mostafa Barigou. Vibrational flow of non-newtonian fluids. *Chemical Engineering Science*, 56(12):3845–3853, 2001.

[118] Miaomiao Zhou, Bae Hoon Lee, Yu Jun Tan, and Lay Poh Tan. Microbial transglutaminase induced controlled crosslinking of gelatin methacryloyl to tailor rheological properties for 3d printing. *Biofabrication*, 11(2):025011, 2019.

[119] Tanmay Jain, Hannah B Baker, Anna Gipsov, John P Fisher, Abraham Joy, David S Kaplan, and Irada Isayeva. Impact of cell density on the bioprinting of gelatin methacrylate (gelma) bioinks. *Bioprinting*, 22:e00131, 2021.

[120] Nishant S Kulkarni, Gautam Chauhan, Mimansa Goyal, Sruthi Sarvepalli, and Vivek Gupta. Development of gelatin methacrylate (gelma) hydrogels for versatile intracavitary applications. *Biomaterials Science*, 10(16):4492–4507, 2022.

[121]

[122] EM Abdelrazek, AM Hezma, A El-Khodary, and AM Elzayat. Spectroscopic studies and thermal properties of pcl/pmma biopolymer blend. *Egyptian Journal of basic and applied sciences*, 3(1):10–15, 2016.

[123] A Cafarelli, A Verbeni, A Poliziani, P Dario, A Menciassi, and L Ricotti. Tuning acoustic and mechanical properties of materials for ultrasound phantoms and smart substrates for cell cultures. *Acta biomaterialia*, 49:368–378, 2017.

[124] Suresh Sagadevan and Jiban Podder. Investigation of structural, sem, tem and dielectric properties of batio3 nanoparticles. 2015.

[125] Wouter Schuurman, Peter A Levett, Michiel W Pot, Paul René van Weeren, Wouter JA Dhert, Dietmar W Hutmacher, Ferry PW Melchels, Travis J Klein, and Jos Malda. Gelatin-methacrylamide hydrogels as potential biomaterials for fabrication of tissue-engineered cartilage constructs. *Macromolecular bioscience*, 13(5):551–561, 2013.

[126] Jingyi Liu, Liang Li, Hairui Suo, Mengling Yan, Jun Yin, and Jianzhong Fu. 3d printing of biomimetic multi-layered gelma/nha scaffold for osteochondral defect repair. *Materials & Design*, 171:107708, 2019.

[127] Nehar Celikkin, Simone Mastrogiacomo, Jakub Jaroszewicz, X Frank Walboomers, and Wojciech Swieszkowski. Gelatin methacrylate scaffold for bone tissue engineering: the influence of polymer concentration. *Journal of Biomedical Materials Research Part A*, 106(1):201–209, 2018.

[128] Xin Zhao, Qi Lang, Lara Yildirimer, Zhi Yuan Lin, Wenguo Cui, Nasim Annabi, Kee Woei Ng, Mehmet R Dokmeci, Amir M Ghaemmaghami, and Ali Khademhosseini. Photocrosslinkable gelatin hydrogel for epidermal tissue engineering. *Advanced healthcare materials*, 5(1):108–118, 2016.

[129] Xiangbo Zhu, Taijun Chen, Bo Feng, Jie Weng, Ke Duan, Jianxin Wang, and Xiaobo Lu. Biomimetic bacterial cellulose-enhanced double-network hydrogel with excellent mechanical properties applied for the osteochondral defect repair. *ACS Biomaterials Science & Engineering*, 4(10):3534–3544, 2018.

[130] Khoon S Lim, Barbara J Klotz, Gabriella CJ Lindberg, Ferry PW Melchels, Gary J Hooper, Jos Malda, Debby Gawlitta, and Tim BF Woodfield. Visible light cross-linking of gelatin hydrogels offers an enhanced cell microenvironment with improved light penetration depth. *Macromolecular bioscience*, 19(6):1900098, 2019.

[131] Kyunga Na, Sungchul Shin, Hyunji Lee, Donghyeok Shin, Jihye Baek, Hojung Kwak, Minsung Park, Jonghyun Shin, and Jinho Hyun. Effect of solution viscosity on retardation of cell sedimentation in dlp 3d printing of gelatin methacrylate/silk fibroin bioink. *Journal of Industrial and Engineering Chemistry*, 61:340–347, 2018.

A | Appendix A

A mathematical model was developed, according to [43], based on hydrodynamic equations in order to correlate glide forces with viscosity data, obtained from rheological analysis with plate/cone geometry. Injection of a liquid through a needle results in a counteracting force which is described by the Hagen–Poiseuille's law Eq.A.1.

$$F = \frac{8 \cdot \frac{\partial v}{\partial t} \cdot l \cdot R_{syringe}^2}{R_{needle}^4} \cdot \eta + F_{friction;f\left(\frac{\partial v}{\partial t}\right)} \tag{A.1}$$

Eq. A.1 is valid for laminar flow in a cylindrical tube which is defined by a Reynolds number Re « 2300, so a calculation of the Reynolds number was made using parameters for the case at worst risk of turbulence as reported in A.2.

$$Re = \frac{2 \cdot \frac{\partial v}{\partial t} \cdot \rho}{\pi \cdot R_{needle} \cdot \eta} \tag{A.2}$$

Where the maximal flow $\frac{\partial v}{\partial t}$ was 0.2 mL/sec, the density ρ was considered for a 10% GelMA solution equal to the one of water [131], the radius R_{needle} was the one for 22G (0.203 mm) and the dynamic viscosity μ was equal to 0.005 Pa·s and was measured at 37 °C for a shear rate of 1000 s^{-1} from analysis reported in Fig.**??** (asymptotic behavior from 100 s^{-1} onwards). The Hagen–Poiseuille's law requires a defined viscosity for the correct prediction of the glide force. However, the viscosity of a non-Newtonian solution is dependent on the shear rate. Using the common power law model of Ostwald–de Waele to represent the relation between viscosity and shear rate for a non-newtonian fluid (Eq.A.3) is possible to extrapolate the glide injective force for different syringe geometry.

$$\eta = K \cdot \dot{\gamma}^{n-1} \tag{A.3}$$

The velocity v of a non-Newtonian fluid flowing through a needle can be expressed in terms of the average velocity $v_{average}$ applied to the system during injection and the variable distance r between the center of the needle (r = 0) and the needle wall (r =

R_{needle})

$$v = v_{avarage} \cdot \left(\frac{3n+1}{n+1}\right) \cdot \left[1 - \left[\frac{r}{R_{needle}}\right]^{\frac{n+1}{n}}\right] \tag{A.4}$$

Differentiation of Eq.A.4 gives the shear rate dependent on the power law index n Eq.A.5:

$$\dot{\gamma} = -\frac{\partial v}{\partial r} = v_{avarage} \cdot \left(\frac{3n+1}{n+1}\right) \cdot R_{needle}^{\frac{-(n+1)}{n}} \cdot r^{\frac{1}{n}} \tag{A.5}$$

The velocity and shear rate profile according to Eqs. (A.4), (A.5) are valid for non-newtonian fluids. For Newtonian fluids, the velocity profile is a parabola where the maximum velocity is $2v$ at the center of the tube (r = 0) and zero velocity at the tube wall ($r = R_{needle}$). Maximum velocity of a non-Newtonian solution at the same volumetric flow is thereby smaller than that of a Newtonian solution. The maximum shear rate occurs at the wall of the tube, and zero shear rate occurs at the center of the pipe. However, the shear rate is not only a function of the distance r between the center and needle wall, but it is also dependent on the rheological properties of the solution. The shear rate ($\dot{\gamma}$) of a Newtonian solution increases linearly from the center of the needle to the needle wall. In contrast, the shear rate of a non-Newtonian solution is initially smaller than the shear rate of a Newtonian solution, but subsequently exceeds the Newtonian shear rate as the needle wall is approached.

Because the viscosity of a non-Newtonian solution is shear-rate dependent, it changes continuously over the needle cross-section in response to the varying shear rate and is therefore a function of the distance r between the center and the needle wall. A definition of an average shear rate (here termed 'effective shear rate') from the shear rate profile in the needle is needed. The appropriate viscosity at the effective shear rate was then obtained from the viscosity–shear rate profile of the sample.

The effective shear rate is derived by integration of (eq.A.5) over the tube cross-section divided by the circular area of the needle. The average velocity is expressed as a fraction of volumetric flow and needle cross-section $v_{avarage} = \frac{\frac{\partial v}{\partial t}}{\pi \cdot R_{needle}}$:

$$\gamma_{avarage} = \frac{1}{\pi \cdot R_{needle}^2} \cdot \int 2\pi r \cdot \dot{\gamma}(r) dr = \frac{2\partial v/\partial t}{\pi R_{needle}^3} \cdot \frac{3n+1}{2n+1} \tag{A.6}$$

To predict the glide force based on the viscosity–shear rate profile, Eq.A.6 is inserted into Eq. 2.1 to calculate the viscosity at the effective shear rate. As a result, combination of

Eqs.(A.1), (A.3), (A.6) gives:

$$F = 2^{n+2} \cdot \pi^{1-n} \cdot l \cdot R_{Syringe}^{2} \cdot K \cdot Q^{n} \cdot R_{needle}^{-(3n+1)} \cdot \left(\frac{3n+1}{2n+1} \right)^{n-1} + F_f \qquad \text{(A.7)}$$

Eq.A.7 describes the glide force, considering also the friction force F_f, of a non-Newtonian fluid based on the viscosity–shear rate profile from plate/cone rheometry dependent on the syringe/needle dimensions, volumetric flow, and rheological properties of the solution and was implemented to calculate the theoretical force value and used as control.

List of Figures

List of Tables

List of Symbols

Variable	Description	SI unit
$\boldsymbol{K}$	consistency index	$(\text{Pa} \cdot s)^n$
$\boldsymbol{n}$	flow index	adim.
$\boldsymbol{\eta}$	viscosity	$\text{Pa} \cdot \text{s}$
$\boldsymbol{\gamma}$	shear strain	%
$\boldsymbol{\dot{\gamma}}$	shear rate	s^{-1}
$\boldsymbol{\sigma}$	stress	Pa
$\boldsymbol{\epsilon}$	deformation	adim.

Acknowledgements

I want to say thank you to the people who have made me grow along this path and who have taught me something, making sure I move forward one small step at a time. I thank Professor Ricotti and all the guys in the group who immediately made me feel part of something and never left me alone. I thank Professor Farè for her availability and ability to always put me in a position to do things properly, stimulating me to think and mature independently. I thank all the people who supported me during the various periods I spent in the PoliMI laboratories, for granting me access to the equipment and giving me advice. Finally, I thank my family, those who have always been there and those who I hope will always be there.

ADMAIORA: The results of this thesis can be seen as a parallel result of the project (and the funds used to purchase various reagents were those of the project): This work has been carried out in the framework of and received funding from the European Union's Horizon 2020 research and innovation programme under grant agreement No 814413, project ADMAIORA (ADvanced nanocomposite MAterIals fOr in situ treatment and ultRAsound-mediated management of osteoarthritis)